The Effect of Measurement Uncertainties on the Inferred Stability of Planes of Satellite Galaxies

Prem Kumar
University of Potsdam

A thesis submitted for the degree of
Master of Science
in Astrophysics

Supervised by:
Dr. Marcel Pawlowski
Prof. Dr. Philipp Richter

Statement of originality

I hereby declare that the submitted Master's thesis is my work and that, to the best of my knowledge, it contains no sources or resources other than the ones mentioned and acknowledged. During the wring the writing of the thesis, I indicated all quotes, citations, and references that were taken from published or unpublished publications, such as books, journals, academic articles, newspapers, reports, etc. Furthermore, the research described in this thesis is based on work conducted at the Leibniz-Institut für Astrophysik Potsdam (AIP) and no part of this thesis has been submitted elsewhere for any other degree or qualification

Acknowledgements

I am profoundly grateful for the support and guidance provided by my supervisor, Dr. Marcel Pawlowski. His unwavering commitment to my academic journey, along with his invaluable insights, has been the cornerstone of this research endeavor. Dr. Pawlowski's expertise has not only shaped this thesis but has also enriched my understanding of the subject matter. I am equally thankful to my second supervisor, Prof. Dr. Philipp Richter, for his valuable input, thoughtful critiques, and guidance that significantly contributed to the depth and quality of this research.

Special gratitude is owed to Kosuke Jamie Kanehisa for his invaluable assistance with the Tensor of Inertia code. His expertise and willingness to share knowledge have been instrumental in overcoming challenges encountered during the course of this research.

Zusammenfassung

Beobachtungen haben ergeben, dass die Milchstraße, die Andromeda-Galaxie und Centaurus A raumlich dünne und kinematisch kohärente Ebenen von Satelliten um sie beherbergen. Solche Strukturen gelten als äußerst unwahrscheinlich im Rahmen des Standard-ΛCDM-Kosmologiemodells, und die Stabilität dieser Ebenen ist seit langem Gegenstand kontroverser Diskussionen. Die genaue Bestimmung der Stabilität dieser Satellitenebenen erfordert ein gründliches Verständnis orbitaler Parameter wie Eigenbewegung, Entfernung und Geschwindigkeit entlang der Sichtlinie, zusätzlich zum Gravitationspotenzial der Gastgalaxie. Viele dieser Parameter bleiben jedoch unzureichend eingeschränkt, was zu erheblichen Unsicherheiten in jeder Analyse führt. Diese Forschung zielt darauf ab, die Auswirkungen von Messunsicherheiten in Eigenbewegungen und Entfernungen der Satellitengalaxien auf die abgeleitete Stabilität dieser Satellitenebenen zu untersuchen. Um dies zu untersuchen, werden Computersimulationen von Test-Satellitengalaxien, die eine Gastgalaxie umkreisen, erstellt. Diese simulierten Satellitensysteme werden dann imitiert beobachtet und analysiert, um Trends und Korrelationen zwischen den bekannten Anfangsbedingungen und Unsicherheiten in den orbitalen Parametern der Satellitensysteme zu identifizieren. Darüber hinaus wurden auch die Auswirkungen unterschiedlicher Milchstraßenpotenziale und unterschiedlicher orbitaler Exzentrizitäten berücksichtigt. Die Ergebnisse deuten darauf hin, dass Unsicherheiten in den Eigenbewegungen zu einer abgeleiteten, scheinbaren Ausdehnung einer intrinsisch stabilen Satellitenebene führen, wobei ihre Breite linear mit den angenommenen Unsicherheiten in der Eigenbewegung zunimmt. Selbst bei Unsicherheiten auf dem Niveau von Gaia-Systematiken, wie zum Beispiel 0,04 masyr^{-1}, wird die Ebene bereits für Satelliten auf ähnlich exzentrischen Umlaufbahnen wie das beobachtete Milchstraßensatellitensystem stark instabil. Unsicherheiten in der Entfernung tragen ebenfalls deutlich zur Instabilität bei. Unter den verschiedenen analysierten Potenzialmodellen der Milchstraße hatte eine Unterschätzung des Potenzials der Gastgalaxie einen signifikanten Einfluss auf die Stabilität dieser Ebenen.

Abstract

Observations have revealed that the Milky Way, Andromeda Galaxy, and Centaurus A host spatially thin and kinematically coherent planes of satellites around them. Such structures are considered highly improbable within the standard ΛCDM cosmological model, and the stability of these planes has been a subject of debate for a long time. Accurately determining the stability of these satellite planes requires a thorough understanding of orbital parameters such as proper motion, distance, and line-of-sight velocity, in addition to the gravitational potential of the host galaxy. However, many of these parameters remain insufficiently constrained, leading to significant uncertainties in any analysis. This research aims to explore the impact of measurement uncertainties in proper motions and distances of the satellite galaxies on the inferred stability of these satellite planes. To investigate this, computer simulations of test satellite galaxies orbiting a host galaxy are set up. These simulated satellite systems are then mock-observed and analyzed to identify trends and correlations between the known initial conditions and uncertainties in the orbital parameters of the satellite systems. Additionally, the effect of different Milky Way potentials and different orbital eccentricities have also been considered. The findings indicate that uncertainties in proper motions lead to an inferred, apparent widening of intrinsically stable satellite plane, with their width increasing linearly with the adopted proper motion uncertainties. Even with uncertainties on the level of Gaia systematics, such as 0.04 masyr^{-1}, the plane becomes already highly unstable for satellites on similarly eccentric orbits as the observed Milky Way satellite system. Uncertainties in distance also contribute noticeably to the instability. Among the various Milky Way potential models analyzed, underestimating the host galaxy's potential showed a significant impact on the stability of these planes.

Contents

List of Tables

List of Symbols

a	major axis
b	intermediate axis
c	minor axis
c/a	minor-to-major axis ratio
μ_a	mean major axis
μ_b	mean intermediate axis
μ_c	mean minor axis
$\mu_{c/a}$	mean minor-to major axis ratio
$\Delta_{c/a}$	absolute difference between backward $\mu_{c/a}$ and forward $\mu_{c/a}$
$f_{c/a}$	relative change between backward $\mu_{c/a}$ and forward $\mu_{c/a}$
ϵ_μ	proper motion uncertainties
ϵ_{dist}	distance uncertainties
$N_{\text{realization}}$	forward integration realizations
$M_{\text{realization}}$	backward integration realizations
N_{sat}	number of test satellites

Chapter 1

Introduction

Cosmology, the scientific investigation of the structure, evolution, and composition of the universe, has been a topic of human curiosity and inquiry since ancient times. Throughout human history, various cultures and civilizations, including the Greeks, Indians, Chinese, and Muslims, have attempted to comprehend the origins and riddles of the universe through philosophical and religious mediums. However, it was only in the last few centuries that cosmology evolved as a distinct discipline within physics, utilizing a rigorous, empirical, and data-driven approach to unveil the secrets of the cosmos.

The advent of modern cosmology was characterized by the outcomes of new observational technologies, analytical methods, and computational capacities, which allowed for exceptional exploration of the universe. Despite the extensive progress in cosmology, much remains to be understood about the universe. The study of cosmology continues to pose some of the most complex and challenging questions in science, requiring interdisciplinary collaboration and the integration of cutting-edge technology, observational data, and theoretical models. The pursuit of understanding the universe through the lens of cosmology remains a quest of immense importance.

1.1 Cosmological background

It won't be wrong to state that modern cosmology traces its roots of origin back to 1916 when Albert Einstein published his groundbreaking work, Die Allgemeine Relativitätstheorie (the general theory of relativity) (Einstein, 1915). According to his theory, gravity is not a force between masses, as it was considered in classical mechanics, but instead, it is the curvature of spacetime caused by the presence of mass and energy. The curvature of spacetime is described by the Einstein field equations, which later on, were solved by A. Friedmann, G. Lemaître, H. P. Robertson, and A. G. Walker, under the assumption of the Cosmological Principle (Friedman, 1922; Lemaître, 1927; Robertson, 1929; Walker, 1935). This principle states that at large scales, the universe is considered to be homogeneous and isotropic. Observations of the CMB have shown a significant level of isotropy when the dipole component (which arises from the relative motion of the Local Group) and the contribution of the Milky Way's emission (which can be quite strong at frequencies close to those

Figure 1.1: The ALMA antennae are illuminated by a red glow, while the background includes the southern Milky Way to the left and the Magellanic Clouds at the top. Image source: European Southern Observatory

of the CMB) are excluded (Ade et al., 2014). However, galaxies may be grouped or clustered with higher random velocities on smaller scales of a few Mpc. Therefore, to study the large-scale structure of the universe and its homogeneity, one needs to look at even larger scales beyond a few Mpc, where the random velocities of galaxies appear to be more homogeneous. This requires using large telescopes and surveys that cover a wide area of the sky to map out the distribution of galaxies on larger scales. Large sky surveys such as SDSS have shown homogeneity is reached for scales greater than 70 Mpch^{-1} (Sarkar et al., 2009). Based on the cosmological assumption, a model of the universe was created, the dynamics of which are determined by the Friedmann-Lemaître equations (Friedman, 1922):

$$H^2 = (\frac{\dot{a}}{a})^2 = \frac{8\pi G}{3}\rho - \frac{kc^2}{a^2} + \frac{\Lambda c^2}{3} \tag{1.1}$$

$$\frac{\ddot{a}}{a} = -\frac{4\pi G}{3}(\rho + \frac{3p}{c^2}) + \frac{\Lambda c^2}{3} \tag{1.2}$$

Here, a is the scale factor of the universe, ρ is the density of matter, p is the pressure of the universe, c is the speed of light, G is the gravitational constant, Λ is the cosmological constant, and k is the curvature of space (which can be positive, negative, or zero). The dots above a denote derivatives with respect to time. These equations describe the evolution of the universe based on its energy density and pressure. Equation 1.1 is usually written in terms of density parameters, which are the dimensionless quantities that describe the relative contributions of different types of matter and energy to the total energy density of the universe.

$$H(a)^2 = H_0^2 \left[\Omega_{\mathrm{r},0} a^{-4} + \Omega_{\mathrm{m},0} a^{-3} + \Omega_{\mathrm{k},0} a^{-2} + \Omega_{\Lambda,0}\right] \tag{1.3}$$

Here, Ω_i represents the cosmic density parameter (where i denotes different energy components: radiation, matter, curvature, and dark energy) and *H(a)* is the Hubble parameter, which is a measure of the rate at which the universe is expanding (Hubble and Humason, 1931).

Today, the scientific community widely accepts the Lambda Cold Dark Matter (ΛCDM) cosmological model due to its ability to explain a range of astrophysical phenomena such as Big Bang Nucleosynthesis, the accelerated expansion of the universe, the power spectrum of the Cosmic Microwave Background, and large-scale structure traced by observed galaxies (McGaugh, 2015; Merritt, 2017). It is based on the idea that the universe is composed of three main components with some shocking proportions: normal matter accounting for only about 5%, cold dark matter about 27%, and dark energy about 68%, which can be associated with Einstein's cosmological constant (Ade et al., 2016).

In terms of particle physics, normal matter is made up of baryons (e.g., protons, neutrons, and other sub-atomic particles) and leptons (e.g., electrons and muons etc.). Regarding dark matter, it is still quite uncertain what exactly it is composed of. The presence of dark matter is mostly inferred from astronomical observations. The earliest indications of dark matter date back to the start of the 20th century when researchers observed mass excess that contradicted the established theory of Newtonian dynamics. In 1937, Swiss astrophysicist Zwicky conducted a study on the velocity dispersion of galaxies in the Coma cluster, comparing it to the virial theorem (Zwicky, 1937). The results showed that a significantly higher amount of mass was required than what could be inferred from stars alone. During the 1970s, strong evidence of dark matter came out when researchers found a discrepancy in the rotational curves of the Milky Way and other close galaxies. They found that stars in spiral galaxies had either flat or increasing rotation velocities as the radius increased. These observations implied the presence of a substantial amount of non-luminous matter outside the optical galaxy (Rubin and Ford Jr, 1970). Other strong evidence for the presence of dark matter has been produced through gravitational lensing of background objects by galaxy clusters, such as the Bullet Cluster (Clowe et al., 2006).

Like cold dark matter, the evidence of dark energy has also been obtained with indirect methods. It wasn't until researchers noticed that the Universe was expanding at an increasing rate that we included dark energy in the cosmological model. This phenomenon of accelerating expansion was observed through the distance examination of Type Ia supernovae (SNIa) that were used as standard candles. The measured distances were significantly larger than the model predicted without the presence of dark energy (Riess et al., 1998; Perlmutter et al., 1999).

1.1.1 Structure Formation

The CDM theory and observations of the CMB have been crucial in developing our understanding of the formation and evolution of large-scale structures in the universe (Press and Schechter, 1974). Structure formation refers to the process by which large-scale structures in the universe, such as galaxies, clusters of galaxies, and cosmic filaments, form and evolve over time. A significant achievement of the ΛCDM model was the agreement between its predicted and observed anisotropies in the Cosmic Microwave Background Radiation (CMBR) created during the recombination epoch. According to this model, the formation of structures on the largest scales is predominantly influenced by the gravitational forces of dark matter, causing the matter to gather into dense clusters, sheets, and filaments, with vast empty spaces known as voids in between. One of the primary objectives of modern cosmology is to understand how the structure of our universe evolved from its early stages. The prevailing idea is that of inflation, which leads to a homogeneous universe, but quantum fluctuations in the very early universe produced fluctuations in density. These fluctuations underwent rapid expansion during the inflationary period, and eventually, the density fluctuations grew large enough to undergo gravitational collapse, leading to the formation of the first structure. This process emphasizes the crucial role of dark matter in shaping the universe, as it provides the gravitational potential necessary for structure formation.

In a matter-dominated universe, the formation of structure is driven by the evolution of matter density perturbations. The degree of perturbation in matter density is quantified using the dimensionless quantity called *density contrast*.

$$\delta(\tilde{r}) = \frac{\rho_m(\tilde{r})}{\bar{\rho}_m} - 1 \tag{1.4}$$

In this equation, $\delta(\tilde{r})$ is the density contrast at a point $\tilde{r}$, $\rho_m(\tilde{r})$ is the matter density at that point, and $\bar{\rho}_m$ is the average matter density of the universe.

In the linear regime, where $\delta(\tilde{r}) \ll 1$ at all scales, linear theory provides a precise description. However, as δ increases due to gravitational instability, the linear approximation becomes insufficient, and nonlinear effects become important. During this period, clumps of dark matter underwent gravitational collapse, leading to the formation of halos and voids, thus producing the known *cosmic web*. It has also been shown that the smaller scales show a higher amplitude to attain nonlinear mass than larger scales, causing them to collapse before larger structures, thus leading to a *bottom-up* scenario for structure formation, with lower-mass structures forming first (White and Rees, 1978).

The nonlinear evolution of the density field is complex and defies analytical description. Therefore, the most efficient way to study the nonlinear evolution of the density field is through numerical simulations. High-resolution computer simulations have allowed for precise predictions regarding the distribution and properties of galaxies and clusters. For a brief period of time, the leading simulations were the Millennium-I (Springel et al., 2005) and Millennium II (Boylan-Kolchin et al., 2009), which served as the foundation for over 400 research studies. Later, with

advancements in the measurement of cosmological parameters, simulation methods, and computing power, newer simulations such as Bolshoi (Klypin et al., 2011) and BigBolshoi/MultiDark (Prada et al., 2012; Riebe et al., 2013) have been able to deliver more precise results. These simulations have been recomputed using the latest Planck cosmological parameters (Klypin et al., 2016).

Figure 1.2 shows the distribution of galaxies within large-scale structures. This illustration includes data from the observational CfA2 (Geller and Huchra, 1989), 2dFGRS (Colless et al., 2001), and SDSS (York et al., 2000) surveys, as well as a model created by the Millennium simulation (Springel et al., 2005). The image demonstrates that the galaxies are aligned as part of these large-scale structures.

There are even some theoretical models that explain the nonlinear evolution. For instance, the spherical collapse model states that regions with a density higher than the background will evolve similarly to an isolated matter-dominated universe, and these regions will expand until a turning point, at which they collapse until the matter reaches an equilibrium state where the potential energy is equal to twice the kinetic energy, as described by the virial theorem. The density at which this happens is about 178 times the background density, which is normally rounded up to 200 to define halo masses as M_{200} (White, 2001).

$$M_{\rm vir} = \frac{4\pi}{3}\bar{\rho}_m \Delta_{\rm vir} r_{\rm vir}^3 \tag{1.5}$$

Where $M_{\rm vir}$ is the virial mass of a dark matter halo, $\bar{\rho}_m$ is the mean matter density of the universe, $\Delta_{\rm vir}$ is the virial overdensity, and $r_{\rm vir}$ is the virial radius of the halo.

1.2 Towards the Observation

As previously discussed, the ΛCDM model is widely accepted among researchers as the preferred cosmological model on large scales. However, it faces difficulties in explaining the properties and formation of galaxies on smaller scales, particularly concerning the satellite dwarf galaxies of large galaxies such as the Milky Way and its neighboring galaxy, Andromeda. One of the concerning challenges is the "planes of satellite galaxies problem" (Pawlowski, 2018). This challenge arises from the presence of a thin and kinematically coherent plane of satellite galaxies surrounding their host galaxies, which is difficult to replicate in ΛCDM simulations. Additionally, the model encounters difficulties with other features, such as the "cusp/core (CC) problem" (Bullock and Boylan-Kolchin, 2017), the "missing satellite problem" (MSP) (Klypin et al., 1999), and the "Too Big To Fail" (TBTF) problem". Recently, these concerns have been largely addressed through the shift from dark-matter-only (DM only) simulations to those that also consider baryonic feedback (Garrison-Kimmel et al., 2019). With the inclusion of baryonic feedback effects, simulations have been able to more accurately replicate the observed satellite galaxies around the Milky Way and other galaxies. Examples of baryonic feedback processes include supernovae explosions, which can eject gas from a galaxy and prevent the formation of

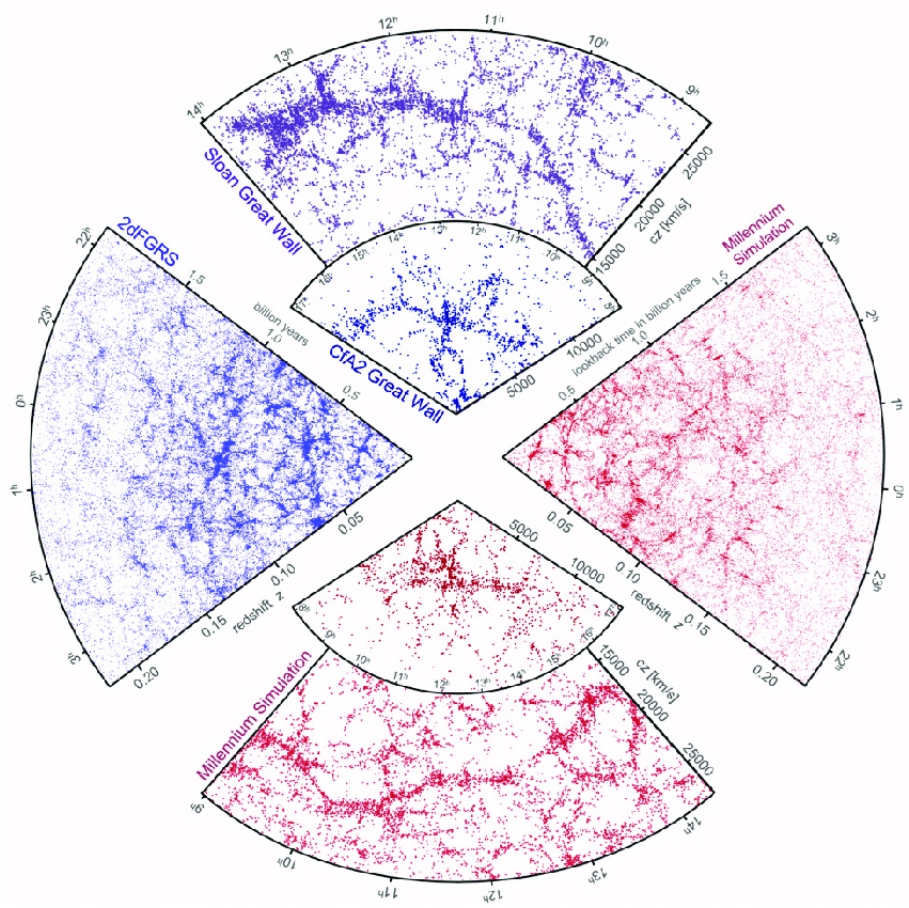

Figure 1.2: The arrangement of galaxies obtained through spectroscopic redshift surveys and mock catalogues generated from cosmological simulations (Springel et al., 2006).

new stars, and the formation of black holes. Baryonic feedback is an important factor to consider in simulations of galaxy formation and evolution, as it can have significant impacts on the properties of a galaxy (Hopkins et al., 2014).

This section will focus on the examination of several significant satellite planes surrounding their host galaxies, along with an exploration of prior studies on similar structures.

1.2.1 The Vast Polar Structure (VPOS) of the Milky Way

The Milky Way is surrounded by several relatively small galaxies that are bound to it, and their distribution is highly anisotropic, meaning that they are not isotropic or uniformly distributed in all directions (see Figure 2.4). Instead, they are largely concentrated in a thin plane around the Milky Way, with a few more distant outliers (Lynden-Bell, 1976; Kroupa et al., 2005; Pawlowski et al., 2012).

By the 1990s, only a handful of 11 satellite galaxies of the Milky Way had been discovered and are now referred to as the "classical" satellites. The number of known satellite galaxies of the Milky Way has significantly increased with the advancements in observational technology, larger telescopes and systematic sky surveys and around 60 dwarf galaxies have been discovered (Simon, 2019). The discovery of these additional satellites has provided valuable insights into the distribution and properties of satellites around the Milky Way, which has helped to enhance our understanding of their formation and evolution. The satellites are arranged in a thin disk-like structure known as the "vast polar structure (VPOS)" with a narrow plane, root mean square (rms) thickness of 20-30 kpc, axis ratio c/a of 0.18–0.30, a radius of about 250 kpcs. The VPOS is almost perpendicular to the Milky Way (Pawlowski and Kroupa, 2020). The proper motions (PMs) of the 11 brightest or classical MW satellites were studied, and it was found that almost all of these orbit in the same direction (Pawlowski and Kroupa, 2013), suggesting that these satellite galaxies form a coherent structure and may have evolved together. At least eight of these satellite galaxies are consistent with orbital planes that are closely aligned with the VPOS - Carina, Draco, Fornax, Leo II, LMC, SMC, and Ursa Minor appear to co-orbit along the VPOS, while Sculptor appears to be counter-orbiting in the structure. Additional, fainter satellite galaxies discovered, primarily through the Sloan Digital Sky Survey (SDSS) and the Dark Energy Survey (DES), have bolstered this favored spatial alignment.

Although there is a serious concern among researchers that the sky coverage such as SDSS is not uniform, and covers the regions close to the Milky Way poles which could potentially bias the observed distribution of satellite galaxies, researchers also find that if the satellites were picked from an isotropic distribution, this would be unlikely (Pawlowski, 2018).

1.2.2 The Great Plane of Andromeda (GPoA)

The Pan-Andromeda Archaeological Survey (McConnachie et al., 2009) sky survey, which covers a distance of about 150 kiloparsecs (kpc) from M 31, has revealed a

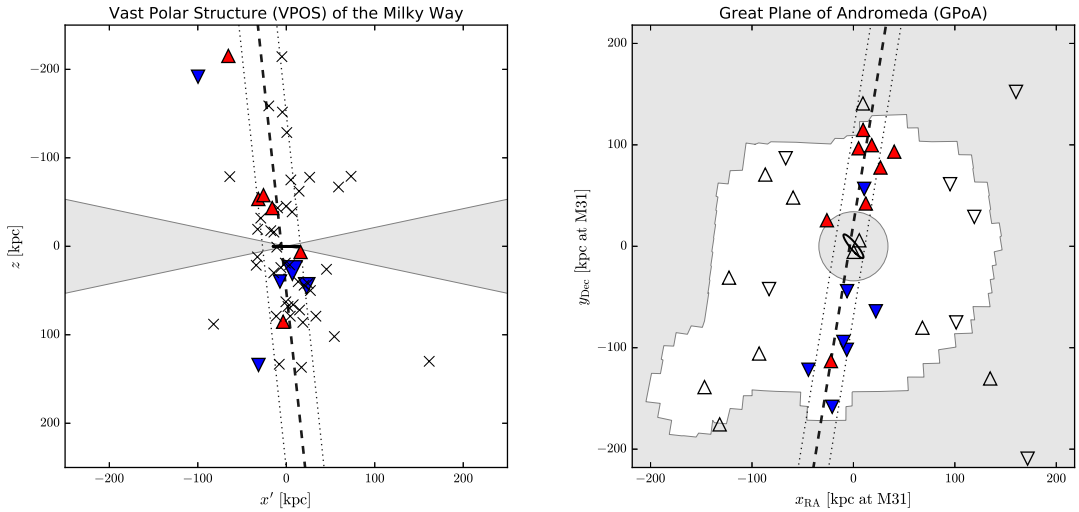

Figure 1.3: These figures display the edge-on views of the Milky Way and Andromeda galaxy's satellite planes. The left panel showcases the VPOS of the Milky Way as seen from a vantage point where both the galaxy and the plane of satellite are in an edge-on orientation. The right panel illustrates the GPoA surrounding Andromeda as seen from the Sun. The best fit for the satellite galaxy planes is represented by dashed lines, with the width of these planes depicted by dotted lines. The line-of-sight velocities of the satellites are indicated with blue downward triangles for approaching satellites and red upward triangles for receding satellites that are part of the plane. Open triangles represent satellites that are not part of the plane, while crosses are the satellites fainter than the classical satellites. The shaded areas highlight regions with significant observational limitations (Pawlowski, 2018).

substantial population of satellite galaxies around M31. Like the VPOS, a similar structure of flattened satellite galaxy distributions has also been observed around the Andromeda Galaxy (M31) (Ibata et al., 2013; Conn et al., 2013), which is termed The Great Plane of Andromeda (GPoA), (see Figure 2.4).The GPoA is nearly edge-on as viewed from the Sun, with an average distance (rms plane height) of about 12.6 kpc between the satellites within the GPoA and the plane they are aligned in. This measurement gives us an idea of how closely packed and aligned the satellites within the GPoA are to each other in space. Additionally, the GPoA extends over a distance of 400 kpc and has an axis ratio of $c/a = 0.1$, indicating that the thickness of the GPoA is relatively small compared to its length and width, consistent with the GPoA being a disk-like structure (Pawlowski et al., 2013).

Studies of the M31 satellite system have shown that roughly half of M31's satellite galaxies are believed to be associated with this structure. Ibata et al. (2013) report a high degree of correlation in the line-of-sight velocities of satellite members along the edge-on orientation, with 13 out of 15 observed satellites within the GPoA having a consistent sense of rotation such that northern satellites are receding from us, while the southern satellites are approaching relative to the host. This resembles the rotating structure around its host galaxy, like the VPOS, thus supporting the idea that the GPoA is a nonrandom and coherent structure, rather than an isotropic system. Moreover, Pawlowski et al. (2013) conclude that out of 34 M31 satellites, 19 contribute to the planar structure.

1.2.3 Centaurus A Satellite Plane (CASP)

The study of satellite galaxies has received significant attention from the astronomical community, but much of the focus has been on the dwarf galaxy population within the Local Group. To gain a more comprehensive understanding of dwarf galaxies and their properties, it is important to conduct similar studies in other nearby galaxy groups. This will allow for the evaluation of the generalizability of the phenomena and further advancement in our understanding of galaxy formation and evolution. One such proximate galaxy group is the Centaurus group, centered around the Centaurus galaxy at a distance of 3.6 Mpc (Tully et al., 2009) (with an alternative estimate of 3.8 Mpc (Harris et al., 2010)). Evidence suggests that there are planar structures in this group, similar to those in the Local Group, see Figure 1.4. Tully et al. (2015) initially proposed the existence of two nearly parallel planes of satellite galaxies. These planes are observed nearly edge-on from the Milky Way, with an average root mean square height of 60 kiloparsecs, long axis dimensions of approximately 300 kiloparsecs (c/a ratio = 0.2), and a separation of around 300 kiloparsecs. However, new discoveries of dwarf galaxies have weakened the case for a strict separation between the planes, and the single-plane model (Crnojević et al., 2014, 2016; Müller et al., 2017), now generally accepted and known as the Centaurus A Satellite Plane (CASP), is preferred (Müller et al., 2016). A kinematic study of the 16 dwarf galaxies around the dominant galaxy Cen A was conducted and found that 14 of these satellites appear to be co-rotating around their host galaxy,

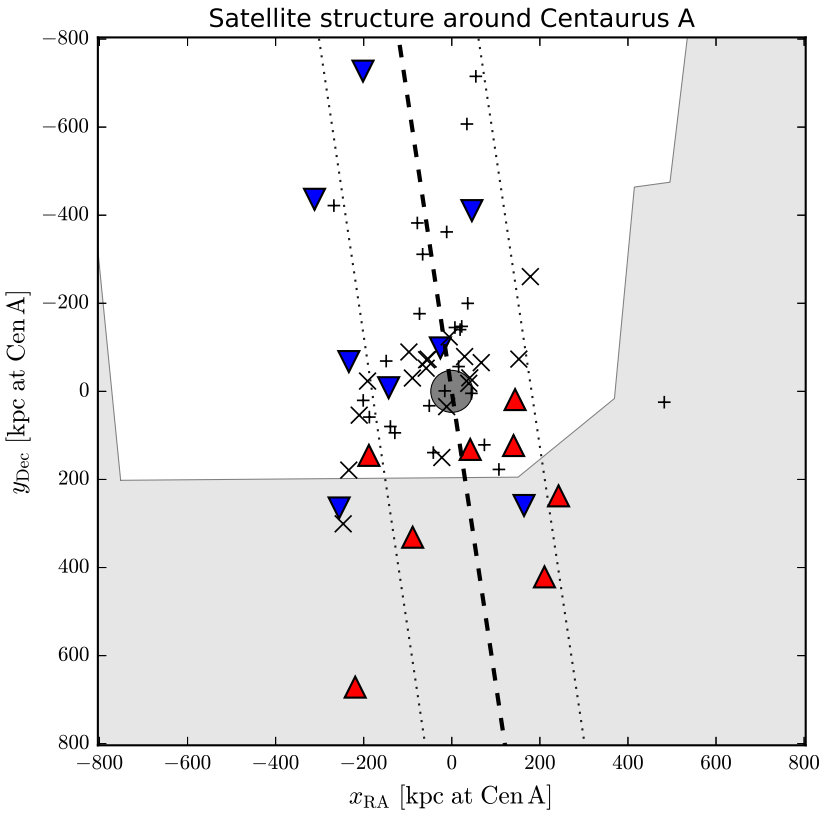

Figure 1.4: Centaurus A satellite plane (CASP) observation in edge-on view shows the best fit of the satellite galaxy plane as a dashed line with its width as a dotted line. Satellite velocities are represented as blue downward triangles for approaching and red upward triangles for receding satellites in the plane, while crosses mark satellites with unavailable velocities. Shaded areas indicate areas with significant observational limitations (Pawlowski, 2018).

.

as judged by their line-of-sight velocities, while the remaining two show different behavior. The satellites in the north of Cen A appear to be moving towards the MW, while those in the south are moving away, similar to what is observed in the Great Plane of Andromeda (GPoA)(Müller et al., 2018).

1.3 Origin of Plane of Satellites

The exact origin of these planes of satellites is not fully understood and is an active area of research in astrophysics. However, various hypotheses have been proposed to explain the phenomenon of planes of satellite galaxies, but three of them that are majorly discussed are shown in Figure 1.5). The first is the accretion hypothesis, which suggests that satellites are accreted onto the host galaxy along a preferred plane due to the anisotropic nature of the large-scale structure of the universe. The second hypothesis is the accretion of dwarf galaxies in groups. The third is the tidal alignment hypothesis, formed from the debris thrown out by galactic collisions.

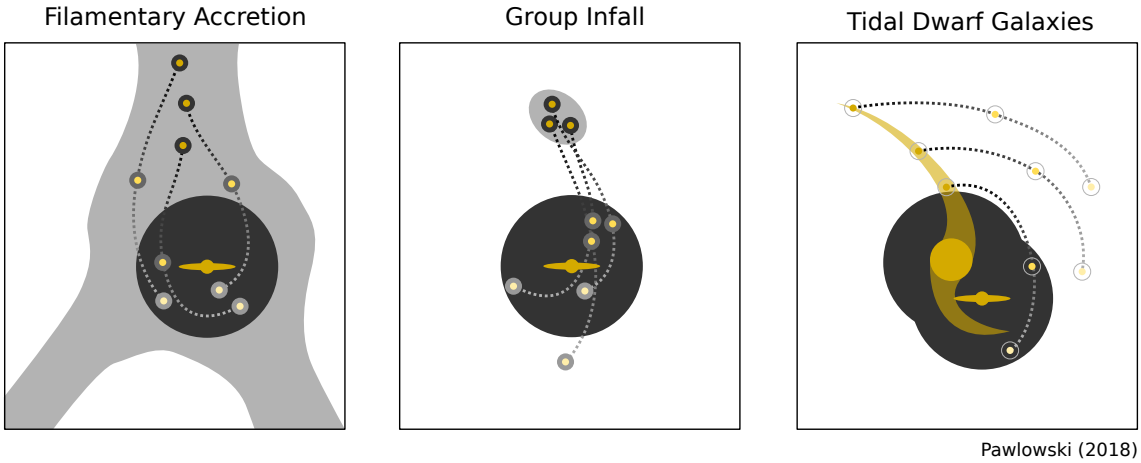

Figure 1.5: Illustrations of three possibilities for the formation of satellite galaxy planes. On the left, accretion of dwarf galaxies from filaments onto the central galaxy's halo. In the middle, dwarf galaxies accreted in groups. On the right, second-generation tidal dwarf galaxies formed from the tails of interacting galaxies (Pawlowski, 2018).

These would naturally form along the plane of the collision, potentially leading to a planar arrangement.

It is important to note that the available evidence supporting each of these hypotheses is inconclusive, and further research is necessary to achieve a comprehensive understanding of the underlying causes. While some studies have provided evidence that supports one or more of these hypotheses, other studies have also presented evidence that contradicts or challenges these hypotheses. Each of the hypotheses put forward to explain the phenomenon of planes of satellite galaxies has its own unique merits and demerits, which will be examined in further detail in the following analysis.

1.3.1 Filamentary accretion

One of the possible explanations for the phenomenon of planes of satellite galaxies is that they were preferentially accreted along large, cosmic filaments (Lovell et al., 2011). As per the ΛCDM model, large galaxies form at the intersections of dark matter filaments. These filaments are thought to be the locations where dark matter density is highest and result in the formation of the first galaxies. This model also suggests that smaller dwarf galaxies form along these filaments and eventually, under the gravitational pull, fall towards the larger galaxies. This process could potentially explain the correlation of galaxy positions in the universe.

However, one of the main issues with this hypothesis is that the filaments found in cosmological simulations are significantly thicker compared to the observed structures. In order for the filamentary accretion process to fully explain the observed correlation of galaxy positions, the filaments would need to be as thin as the observed structures, which have been observed to be less than 14 kpc. The size of the filaments in the simulations, on the other hand, are typically on the order of 500-1,000 kpc. This discrepancy makes it unlikely that the filamentary accretion

process can fully explain the observed correlation of galaxy positions in the universe (Vera-Ciro et al., 2011).

Additionally, the study by Pawlowski et al. (2012) found that the filamentary accretion origin of the VPOS of the Milky Way satellites could be ruled out. They found that the coherence of the sub-halo orbital poles in high-resolution cosmological simulations is not sufficient to explain the alignment of the MW satellite orbits. This further highlights the challenges faced by the filamentary accretion theory in fully explaining the phenomenon of satellite galaxies. Despite these challenges, the filamentary accretion theory remains a significant area of research, and ongoing studies aim to address these challenges and refine our understanding of the origin and formation of satellite galaxies.

1.3.2 Group Infall

The accretion of satellites from a common infalling group of dwarf galaxies is another mechanism proposed for the formation of satellite planes (Lynden-Bell and Lynden-Bell, 1995). This hypothesis suggests that a group of dwarf galaxies could have fallen into the host galaxy's halo. If these satellites share a specific orbital plane and have similar orbital characteristics, such as orientation, energy, and specific angular momentum, they will likely maintain their alignment when they accrete onto the host galaxy. Samuel et al. (2021) found that the probability of satellite planes forming is higher when a heavy satellite is present, which is often accompanied by smaller satellites.

According to D'Onghia and Lake (2008), the Magellanic Clouds and seven of the eleven dwarf galaxies around the MW may have accreted as a group of dwarfs that were later disrupted in the Galaxy's halo. (Li and Helmi, 2008) found that the observed correlation in the orientation of subhaloes' angular momentum leads to disc-like configurations. They found that if all subhaloes are assimilated from a single group, there is a high probability of obtaining a disc-like distribution (approximately 80 percent). However, for assimilation from only two groups, the chance of obtaining a distribution as planar as observed is about 40 percent. This idea was further supported by research that utilized Gaia proper motion data and discovered a considerable number of satellite galaxies in the LMC's own system. It has also been found that several observed VPOS member satellites, such as Carina and Leo I, are situated in regions that are inaccessible to LMC satellites. This suggests that the formation of the VPOS may not be solely explained by the accretion of a group from the LMC (Nichols et al., 2011).

Moreover, the group-infall theory can be extended to major mergers between two host galaxies. Smith et al. (2016) have shown that such mergers have the potential to generate very thin and stable planes of satellites. They demonstrated that a merger with a mass ratio of 1:2 can result in a plane of satellites with diameters of 150 kpc and a thickness of 10-40 kpc, which can remain stable for up to 6 Gyr.

However, the group infall scenario is at odds with observational evidence from the local Universe, which shows that associations of dwarf satellites are much more

extended, with sizes on the order of 200 kpc, as opposed to the narrow thickness (15-30 kpc) predicted by the group infall scenario (Metz et al., 2009).

1.3.3 Tidal Dwarf Galaxies

This scenario focuses on the possibility that the observed dwarf galaxies may actually be tidal dwarf galaxies (TDGs). TDGs are small, self-gravitating systems that are believed to form from material stripped from larger parent galaxies during collisions or interactions. These galaxies tend to form in the tidal tail and move along its plane, leading to a common orbital direction and the formation of a coherent plane of satellites (Kroupa et al., 2005; Pawlowski et al., 2012). This explanation may help account for why satellite galaxies of the Milky Way and other large galaxies are often found in thin planes, rather than being randomly distributed (Kroupa, 2012; Hammer et al., 2013). The Evolution and Assembly of Galaxies and their Environments (EAGLE) cosmological hydrodynamic simulation supports this scenario by reproducing the formation of TDGs in the tidal tails of interacting galaxies (Ploeckinger et al., 2018). The simulation also predicts that TDGs should be mostly dark matter-free.

However, observations of some of the best candidates for TDGs in the Local Group, such as the dwarf spheroidal galaxies (dSphs), have shown high velocity dispersions relative to their luminosities, leading to mass-to-light ratios that are greater than 10 solar masses per solar luminosity, indicating that they are dark-matter dominated systems (McConnachie, 2012). This discrepancy between the predicted and observed properties of TDGs raises questions about the validity of the TDG scenario.

Several potential solutions have been proposed to address this issue, including the possibility of observational errors or incorrect assumptions about equilibrium in dSphs. Other solutions involve modifying the properties of dark matter or switching to a modified gravity framework. Although these solutions offer potential explanations, they would require significant revisions to our current understanding of dark matter and galaxy formation.

1.4 Motivation

As previously discussed, the study of satellite galaxies, particularly those orbiting the Milky Way and Andromeda galaxies, has been a significant area of research in astrophysics due to their intriguing properties. A central challenge in this field is the accurate determination of the orbital parameters of these satellites. This task necessitates a comprehensive understanding of multiple critical parameters, including the satellites' positions, velocities, and the gravitational potential of their host galaxies. A major complication arises from the fact that many of these parameters are not sufficiently constrained, leading to substantial uncertainties in analyses (Pawlowski et al., 2017). While Gaia has revolutionized our understanding of Milky Way dwarf galaxies by providing increasingly accurate measurements of proper motions (Fritz

et al., 2018; Gaia et al., 2018), a significant amount of measurement uncertainty still remains. These uncertainties necessitate careful consideration in analyses, as they can obscure any correlations. Previous research, such as the works of Maji et al. (2017) and Sawala et al. (2023), have suggested that the satellite plane may be unstable or a mere coincidental alignment, but these studies often overlooked the impact of measurement uncertainties. Therefore, it is imperative to account for these measurement errors in any analysis of satellite galaxy orbits. Ignoring or underestimating these errors can lead to incorrect interpretations or conclusions about the dynamics and stability of satellite planes. The incorporation of measurement uncertainties, particularly in proper motion data, is essential for achieving a more realistic and reliable understanding of the satellite galaxies' orbital behaviors.

To address this issue, this master's thesis proposes a novel method: using computer generated simulations to model the orbits of test satellite galaxies around a host galaxy under controlled initial conditions. The test satellites are forward-integrated, and then 'mock-observed' by introducing a wide range of uncertainties in proper motion and other quantities, followed by backward integration. This approach aims to explore the potential impact of these uncertainties on the satellite plane. By analyzing the resulting mock observations, we hope to gain valuable insights into the orbital properties of satellite galaxies. This research will enhance our understanding of the evolution of the satellite plane and contribute significantly to our knowledge of galaxy formation and evolution.

This thesis is structured into several distinct chapters, each focusing on a critical aspect of the research. Chapter 2, titled **Methodology**, details the specific approaches and techniques employed in the study, including the computer simulations and modeling processes. Chapter 3, **Initial Setup**, delves into the initial conditions and parameters set for the simulations, explaining their selection and relevance to the study. Chapter 4, **Results and Discussion**, presents the findings of the research, including the data obtained from the simulations and a thorough analysis of these results, highlighting the implications and insights gained. Finally, Chapter 5, **Summary and Conclusion**, provides a comprehensive summary of the entire research, drawing conclusions from the findings, discussing the implications of the study, and suggesting potential areas for future research. This structure ensures a clear and logical flow, guiding the reader through the stages of the research from methodology to conclusions.

Chapter 2

Methodology

In this section I will focus on discussing the useful and important concepts in order to set up a plane of satellite galaxies orbiting around a host galaxy.

2.1 Coordinate System

Throughout the project, various coordinate systems were utilized to determine the precise positions of the host galaxy and its test satellite galaxy. One of the most commonly used coordinate systems in astrophysics is the cylindrical coordinates. In the cylindrical coordinate system, the position of any celestial object is defined using three coordinates: the radial distance R from the z-axis, the azimuthal angle ϕ, and the height z above the xy-plane. This system is particularly useful for problems exhibiting cylindrical symmetry. When setting up disc-like structures, this system offers control over initial parameters to establish a planar structure. Therefore, I have used the cylindrical coordinate system in my simulated environment to emulate a similar structure and to position test satellites around the host galaxy.

In terms of the Cartesian coordinate system (x, y, z), the Cylindrical coordinate system can be expressed as follows:

$$x = R\cos\phi\,, \tag{2.1}$$
$$y = R\sin\phi\,, \tag{2.2}$$
$$z = z\,, \tag{2.3}$$

and

$$R = \sqrt{x^2 + y^2}\,, \tag{2.4}$$
$$\phi = \text{atan2}(y, x)\,, \tag{2.5}$$
$$z = z\,, \tag{2.6}$$

and their corresponding velocities are:

$$v_x = v_R \cos\phi - v_\phi \sin\phi \tag{2.7}$$
$$v_y = v_R \sin\phi + v_\phi \cos\phi \tag{2.8}$$
$$v_z = v_z \,. \tag{2.9}$$

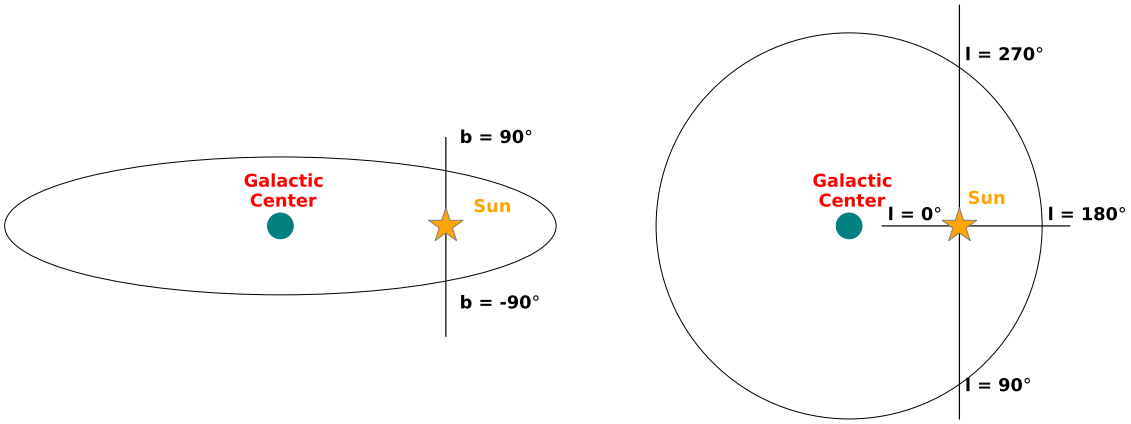

Figure 2.1: Two images showing the Galactic coordinate frame system. On the left, Galactic latitude *(b)* is shown, measured from the Galactic equator to the Galactic poles. The North Galactic Pole is at $b = 90°$, and the South Galactic Pole is at $b =$ -90°. While, the right panel illustrates the Galactic longitude *(l)* that goes from 0°to 360°, measured eastward around the equator in degrees. In both of these panels, the reference point is the Sun.

2.1.1 Position of the Milky Way

For the study of the Milky Way and its satellite galaxies, the Galactic Coordinate System is a widely used reference framework, as illustrated in Figure 2.1. In this system, the Sun is positioned at the origin. This reference system comprises two main components: the galactic latitude (b) and galactic longitude (l). The galactic latitude *(b)* ranges from +90° to -90°. It indicates the angle of an object above or below the galactic plane. On the other hand, the galactic longitude *(l)* measures the angle of an object westward along the galactic equator. Galactic longitude extends from 0° to 360°, increasing in a counterclockwise direction. This coordinate system is especially useful for exploring the structure of the solar neighborhood. However, for more comprehensive studies of the galaxy and its surrounding halo objects, the Galactocentric coordinate system is often more advantageous. This system centers on the Milky Way's core, using it as the primary reference point, as shown in Figure 2.2.

In order to transform galactic coordinates to Galactocentric coordinates, determining the Sun's distance, $R_\odot$, from the Galactic Center (GC) is important for

various areas of astronomy. Over the past few decades, numerous efforts have been made to calculate this distance. Several studies have relied on the S2 star, a massive, young main-sequence B star located in close proximity to the Milky Way's supermassive black hole. The initial measurement yielded a value of $R_\odot = 7.94 \pm 0.42$ kpc (Eisenhauer et al., 2003), which was subsequently updated to $R_\odot = 7.62 \pm 0.32$ kpc (Eisenhauer et al., 2005). Furthermore, Gillessen et al. (2017) reported a distance of $R_\odot = 8.32 \pm 0.07 \pm 0.14$ pc, with the first being the statistical error and second the systematic error. More recently, the detection of gravitational redshift from Sgr A* in the S2 spectra was reported. Utilizing this data, the updated value for $R_\odot$ was estimated as 8.122 ± 0.031 kpc, with a statistical error only (Abuter et al., 2018).

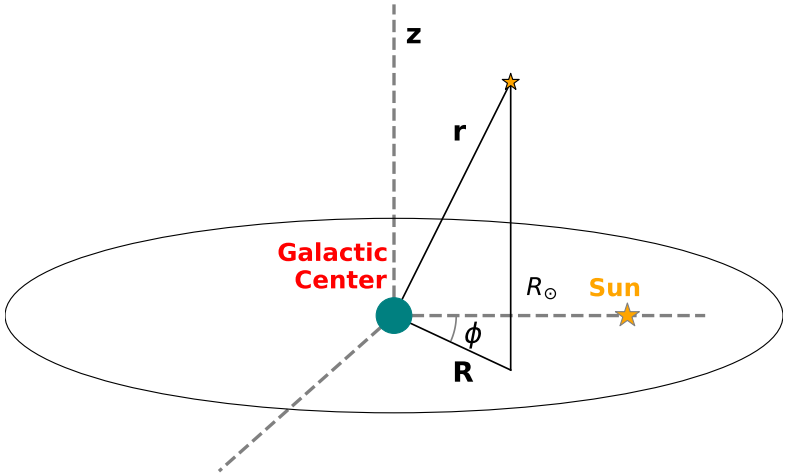

Figure 2.2: Galactocentric coordinate frame system with Galactic Center (GC) as the reference point. Sun lies at $R_\odot$ distance away from the center. To locate any object in this system, R, distance from GC, z, height above midplane, ϕ, azimuthal angle are used. Whereas, r is Galactocentric distance.

Additionally, research has established that the Sun's position in the Milky Way is not precisely in the galactic mid-plane. Since the last century, it has been known that the Sun is actually positioned a few parsecs north of this plane. This elevation, $z_\odot$, is crucial for accurately determining our location within the galaxy. Efforts to measure $z_\odot$ have been diverse, ranging from analyses of the neutral hydrogen layer to the study of star and cluster distributions. For instance, a 1960 study by Gum et al. (1960) estimated $z_\odot = 4 \pm 12$ pc. Later, using the distribution of B0-B5 stars, Stothers and Frogel (1974) calculated z to be 24 ± 3 pc. Other studies, like that of Janes and Adler (1982), employed the spatial distribution of 114 open clusters older than 10^8 years, finding $z_\odot$ to be around 75 pc, assuming a solar distance of 8 to 9 kpc from the galactic center. Moreover, Joshi (2005) obtained $z_\odot = 22.8 \pm 3.3$ pc above the plane through the reddening analysis. Maíz-Apellániz (2001), using O-B5 stars, measures $z_\odot = 24.2 \pm 1.7 \pm 0.4$ pc, with the former being the random error and the latter the systematic error. More recently, Joshi (2007), through analysis of Young Open Clusters, estimated $z_\odot = 17 \pm 3$ pc. Additional methods have contributed further; from the observation of γ-rays, Siegert (2019) estimated $z_\odot = 15 \pm 17$ pc.

In a related vein, several attempts have been made to estimate the Sun's velocity. Dehnen and Binney (1998), using Hipparcos data, determined the solar motion relative to the Local Standard of Rest (LSR), with $(U, V, W)_\odot = (10.00 \pm 0.36, 5.23 \pm 0.62, 7.17 \pm 0.38)$ kms^{-1}, where U, V, and W are the velocity components towards the Galactic Center, in the direction of the Milky Way's rotation, and towards the North Galactic Pole, respectively. Furthermore, Reid et al. (2009), using direct parallax measurements, estimates $(U, V, W)_\odot = (10.3, 15.3, 7.7)$ kms^{-1}. Schönrich et al. (2010), by comparing the local stellar kinematics to a chemodynamical model, estimated $(U, V, W)_\odot = (11^{+0.69}_{-0.75}, 12.24^{+0.47}_{-0.47}, 7.25^{+0.37}_{-0.36})$ kms^{-1}.

Figure 2.2 shows the Galactocentric cylindrical polar coordinates, R, ϕ, and z, to specify the location of test satellite galaxies. The parameter R represents the distance from the Galactic center in the disk plane, while the height above the midplane is denoted by z, with positive values of z indicating the direction towards the north Galactic pole. The azimuthal angle ϕ is measured from the direction pointing towards the Sun.

2.2 Milky Way Potentials

The Milky Way, like other galaxies, possesses a complex structure predominantly influenced by gravitational forces. Understanding the gravitational potential is essential for monitoring the motion of its satellite galaxies and other celestial bodies within and around our galaxy. This potential is derived from the mass distribution of the Milky Way, which can be broken down into several components: the central bulge, the disk, and the dark halo. Notably, distinct potential models are used to represent each of these components individually, reflecting their unique attributes and influences.

2.2.1 The Galactic Disk

The Galactic disk, a flattened structure, comprises the majority of the Galaxy's total stellar mass, including stars, gas, and dust. Extensive studies have been conducted since the last century to explore the dynamics of the Milky Way's disk using various astrophysical models. One of the earliest and simplest is the Kuzmin disk model (Kuzmin, 1956). Initially introduced by Kuzmin in 1956 and later independently rediscovered by Toomre in 1963 (Toomre, 1963), it represents the gravitational potential as follows:

$$\Phi(R, z)_{\text{kuzmin}} = -\frac{G\,M}{\sqrt{R^2 + (|z| + a)^2}}, \tag{2.10}$$

where G is the gravitational constant, M the mass, R the radial distance in the plane of the disk, z the vertical distance, and a a model parameter that sets the characteristic scale of the disk's thickness. In the Kuzmin model, $a \geq 0$.

At a point far from the disk (i.e., when both R and $|z|$ are much larger than a), the Kuzmin model, $\Phi(R, z)_{\text{kuzmin}}$, approximates a point-mass potential:

$$\Phi(R,z)_{\text{point}} \approx -\frac{GM}{\sqrt{R^2+z^2}} = -\frac{GM}{r}, \tag{2.11}$$

where r is the radial distance from the point to the center of the disk.

While the Kuzmin model effectively represents a razor-thin disk, it requires modification to realistically depict the Milky Way with a non-zero vertical thickness. Introducing the scale height, b, as an additional parameter leads to the more comprehensive Miyamoto-Nagai model (Miyamoto and Nagai, 1975), expressed as:

$$\Phi(R,z)_{\text{Miyamoto}} = -\frac{G\,M}{\sqrt{R^2+(\sqrt{z^2+b^2}+a)^2}}. \tag{2.12}$$

The corresponding density component is:

$$\rho(R,z)_{\text{Miyamoto}} = \left(\frac{b^2\,M}{4\pi}\right) \frac{a\,R^2+\left(3\sqrt{z^2+b^2}+a\right)\left(\sqrt{z^2+b^2}+a\right)^2}{\left(R^2+(\sqrt{z^2+b^2}+a)^2\right)^{5/2}\left(z^2+b^2\right)^{3/2}}. \tag{2.13}$$

Setting $a = 0$ in the Miyamoto-Nagai model yields the Plummer spherical potential (Plummer, 1911), and setting $b = 0$ recovers the Kuzmin model, representing a thin disk.

2.2.2 Dark Matter Halo

The Galactic Dark Matter Halo, encircling the stellar disk of the Milky Way, is a crucial component containing a significant portion of the Galaxy's mass. This halo, predominantly composed of dark matter, plays a vital role in the dynamics and structure of the Galaxy.

Dark halos can be modeled using extensions of spherical two-power density models:

$$\rho(r) = \frac{\rho_0}{(r/a)^{\alpha}(1+r/a)^{\beta-\alpha}} \tag{2.14}$$

A diverse range of models emerge from varying α and β. For example, setting $\beta = 4$ with different α values yields the Dehnen models with simple analytic properties (Dehnen, 1993). The Jaffe model (Jaffe, 1983) is obtained with $\alpha = 2$ and $\beta = 4$, while the Hernquist model (Hernquist, 1990) arises from $\alpha = 1$ and $\beta = 4$. Similarly, the NFW model, named after Navarro, Frenk, & White (Navarro, 1996), is defined with $\beta = 3$ and $\alpha = 1$. The NFW model provides a spherically symmetric density profile for dark matter halos:

$$\rho_{\text{NFW}}(r) = \frac{\rho_0}{\frac{r}{r_s}\left(1+\frac{r}{r_s}\right)^2}, \tag{2.15}$$

where r is the radial distance from the center of the halo, r_s the scale radius, and ρ_0 the characteristic density. The NFW profile is known for its cusp-like center, where the density increases sharply towards the halo's core.

An alternative model, the Einasto profile (Einasto, 1965), describes the dark matter distribution with a smoother central density profile:

$$\rho_{\text{Einasto}}(r) = \rho_{-2} \exp\left\{-\frac{2}{\alpha}\left[\left(\frac{r}{r_{-2}}\right)^{\alpha} - 1\right]\right\}, \tag{2.16}$$

where ρ_{-2} is the density at a characteristic radius r_{-2}, and α is a parameter that influences the steepness of the profile.

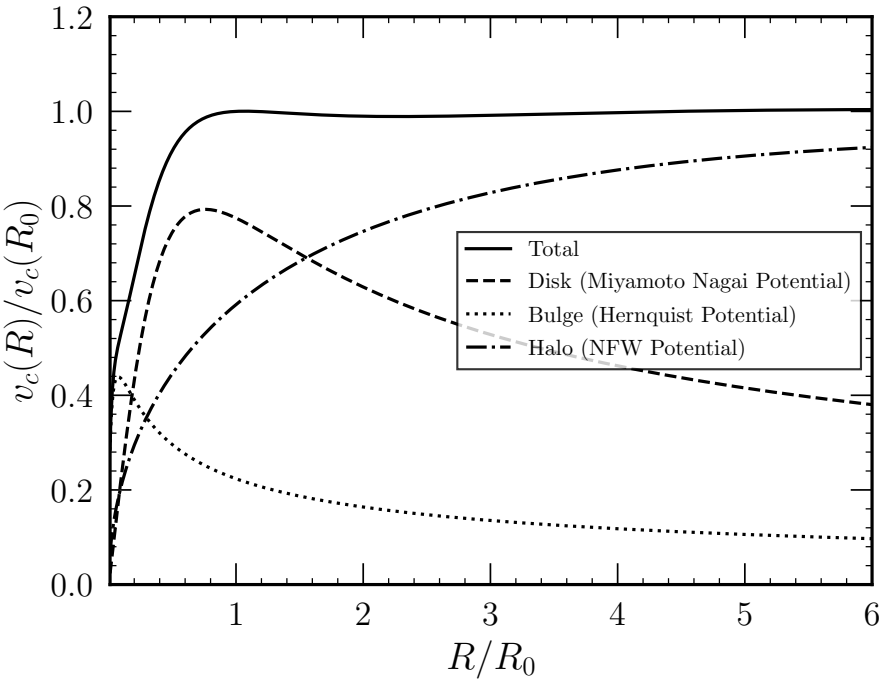

Figure 2.3: Normalized composite rotation curve of Milky Way and its components (bulge, disk, and halo contributions).

2.2.3 Bulge

Another important component of the Milky Way is its Galactic Bulge, a densely populated central region. The Galactic Bulge is characterized by a high concentration of older, metal-rich stars and exhibits a complex structure (Wegg and Gerhard, 2013). Over time, several models have been proposed to determine the mass distribution within the Galactic Bulge.

While the bulge is often assumed to have a spherically symmetric mass distribution, following the de Vaucouleurs law, it can be described by spheroidal models. One such example is the Hernquist model (Hernquist, 1990), a density-potential pair, which provides insights into such distribution.

$$\rho_H = \frac{\rho_b}{\left(\frac{r}{a_b}\right)\left(1 + \frac{r}{a_b}\right)^3} \tag{2.17}$$

and,

$$\phi_H = -\frac{\sigma_b^2}{1 + \frac{r}{a_b}} \tag{2.18}$$

where a_b is the scale length, ρ_b is the characteristic density ($\rho_b = \frac{\rho_b^2}{2\pi a_b^2}$), and σ_b is the characteristic velocity of the bulge.

However, recent studies suggest the actual structure of the Galactic Bulge might be more complex than what the Hernquist model alone can describe. Some studies use an axisymmetric approximation to describe the Galactic bulge, which has the density profile (McMillan, 2016):

$$\rho_b = \frac{\rho_{0,b}}{(1 + r/r_0)^\alpha} \exp\left[-\left(\frac{r}{r_{cut}}\right)^2\right] \tag{2.19}$$

where $\rho_{0,b}$ is the scale density, r_{cut} the cut-off radius, and α the exponent of the power-law.

2.3 Plane fitting

In this study, I initially distribute test satellites randomly within a three-dimensional space to simulate a plane of satellite galaxies, as described in Chapter 3. Subsequently, the next step involves performing plane fitting. For this purpose, a viable method is the unweighted plane-fitting technique outlined by (Metz et al., 2007). This method commences with the calculation of the moment of inertia matrix of the satellite distribution, followed by its diagonalization. The process begins by determining the centroid, r_0, of the data points:

$$r_0 = \frac{1}{N} \sum_{i=1}^{N} r_i$$

Subsequent to this, an eigenvalue analysis of the moment of inertia tensor, $\mathbf{T}_0$, is conducted for the position vectors, $\hat{r}_i = r_i - r_0, i = 1 \ldots n$ (Metz et al., 2007; Pawlowski et al., 2013).

$$T_0 = \sum_{i=1}^{N} \left[(\mathbf{r}_i - \mathbf{r}_0)^2 \cdot \mathbf{1} - (\mathbf{r}_i - \mathbf{r}_0) \cdot (\mathbf{r}_i - \mathbf{r}_0)^T\right]$$

In this formula, $\mathbf{1}$ denotes the unit matrix and $\mathbf{r^T}$ is the transposed version of the vector $\mathbf{r}$. The square-root of the eigenvalues of the moment of inertia indicates the extent along three axes *(a, b, c)* of the fitted ellipsoid to the satellite distribution. These values are proportional to the rms deviation relative to the eigenvectors of $\mathbf{T}$. The eigenvector corresponding to the largest eigenvalue defines the normal of the plane, encompassing the centroid. Meanwhile, the eigenvectors corresponding to the intermediate and smallest eigenvalues indicate the directions of the intermediate and major axes of the distribution, respectively. Consequently, the axial ratios c/a and b/a are determined. A small value of c/a suggests two possibilities: if b/a is large,

it indicates an oblate distribution resembling a thin plane; if b/a is similarly small $(c/a \approx b/a)$, it suggests a narrow prolate distribution resembling a filament-like shape (Metz et al., 2007).

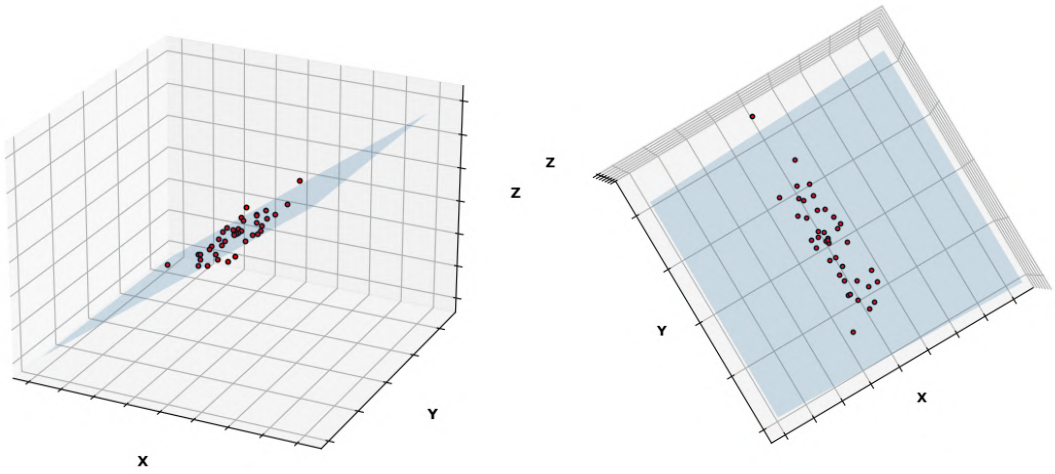

Figure 2.4: Example of plane fitting over N random points in space. Left: Edge-on view. Right: Face-on view.

2.4 Proper Motion

To determine the motion of a galaxy precisely, both its direction and speed are crucial. Spectroscopy is used to track the motion of a star or galaxy as it approaches or recedes from the observer. This is done by analyzing the shift in the wavelength of its emitted light due to its velocity, a phenomenon known as the Doppler effect. However, it's essential to note that radial velocity measures only one dimension. To comprehend how a star or galaxy moves tangentially across the sky, the concept of proper motion is commonly employed. Proper motion represents the apparent angular motion of an object across the plane of the sky, measured in arcseconds per year, resulting from its actual physical movement through space relative to distant background stars. For accurate measurements, one needs at least two observations of the object's position, separated by a known interval of time. Historically, these observations would have been taken using photographic plates, but today, digital detectors like CCDs are used to measure them. Moreover, Measurement of proper motion is time-consuming task, because for many objects, their proper motion is less than an arcsecond per year. In order to detect such small angular changes, observations must often be separated by many years, or even decades. This task becomes even more challenging when observing distant objects. The further an object is from Earth, the smaller its apparent motion appears, even if its absolute velocity is high.

Among the 60 satellite galaxies, which include both classical satellites and others, the Hubble Space Telescope (HST) has successfully determined the proper motion of 11 galaxies associated with our Milky Way. To detect the proper motions of ultra-

faint galaxies, data from Gaia becomes crucial as it provides the most accurate information about their positions (Redd, 2018). However, detecting the proper motion of satellite galaxies poses challenges due to their considerable distance from us. This distance introduces uncertainties in the data, which must be taken into account when analyzing the information. Table 2.1 presents the satellite galaxies of the Milky Way located at a radial distance of 300 kpc. The first column lists the names of the satellites, followed by their galactocentric coordinates in the second and third columns. The fourth column provides information about the heliocentric distances of these satellite galaxies, including measurement uncertainties. Columns five, six, and seven detail the line-of-sight velocity and proper motions in RA and Dec, along with their respective systematic errors.

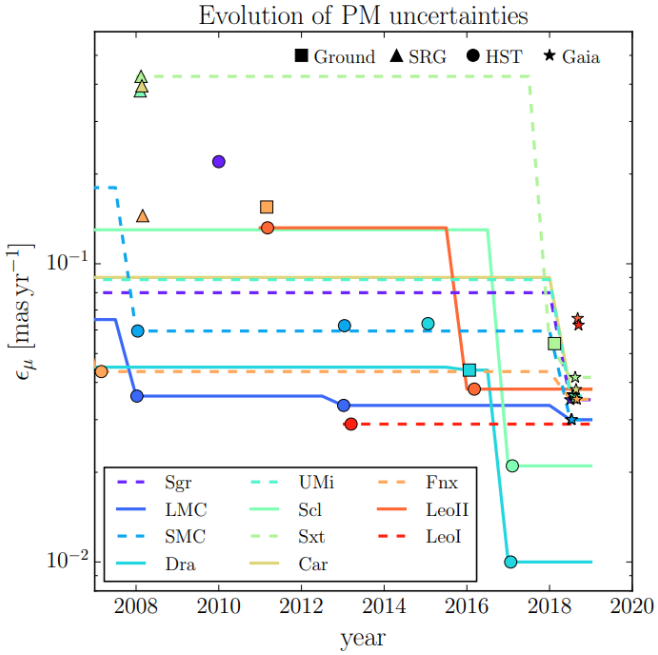

Figure 2.5: The evolution of the proper motion of the 11 classical satellites of the Milky Way over time is depicted. Different symbols indicate the mode of data acquisition, whether through ground-based observations (Ground), observations from the Hubble Space Telescope (HST), data from Gaia DR2 (Gaia), or via the stellar redshift gradient method (SRG). With updated data, proper motion uncertainties are continuously decreasing (Pawlowski and Kroupa, 2020).

.

Generally, data comes with two types of errors: random (or statistical) errors and systematic errors. Random errors, such as instrumental noise or those from other sources, acts as variability between different measurements of the same data. These errors can be largely reduced by taking repeated measurements and applying statistical analysis. Systematic errors, on the other hand, are consistent, repeatable errors that induce a bias in the measurements. They cannot be reduced simply by collecting more data, as with random errors. Such errors can skew the data and lead to false conclusions. Although Gaia has revolutionized data, it also carries both random and systematic errors in its astrometric parameters, such as proper motion and parallax.

The Figure 2.5 shows the smallest reported uncertainties associated with proper motion measurements for the 11 classical satellite galaxies from 2007 to 2018. Here, ϵ_μ represents the average of the errors presented for both components of proper motion. The lines on the graph represent the lowest reported uncertainties in proper motion available in published literature at the beginning of each year. Various symbols denote different detection methods, including ground observations, Hubble Space Telescope (HST), SRG, and Gaia. The graph clearly illustrates that Gaia DR2 has significantly contributed to reducing proper motion errors. The Gaia DR2 indicated proper motion systematic uncertainties at approximately 0.035 to 0.066 masyr^{-1} (Gaia et al., 2018; Helmi et al., 2018), which in Gaia ER3, it managed to decreased by a factor of at least two (Li et al., 2021).

Table 2.1: Adapted from Sawala et al. (2023), this table displays Milky Way's satellite galaxies located within 300 kpc away from the Milky Way. Column 1 shows the name of Satellite galaxies, Columns 2 and 3 detail the galactic longitude and latitude of these satellites. Column 4 lists the heliocentric distances along with their uncertainties. Column 5 includes the line-of-sight velocities and their respective uncertainties. Finally, columns 6 and 7 present the proper motions in Right Ascension and Declination, including their uncertainties.

Satellite	l°	b°	$r_\odot$ [kpc]	V_{los} [kms^{-1}]	$\mu_{\alpha*}$ [masy^{-1}]	μ_δ [masy^{-1}]
Sagittarius I	5.57	-14.17	26.0 ± 2.0	140.0 ± 2.0	-2.692 ± 0.001	-1.359 ± 0.001
LMC	280.47	-32.89	51.0 ± 2.0	262.2 ± 3.4	1.85 ± 0.03	0.234 ± 0.03
SMC	302.80	-44.30	64.0 ± 4.0	145.6 ± 0.6	0.797 ± 0.03	-1.22 ± 0.03
Draco I	86.43	34.71	76.0 ± 6.0	-291.0 ± 0.1	-0.01 ± 0.01	-0.14 ± 0.01
Ursa Minor	104.98	44.81	76.0 ± 4.0	-246.9 ± 0.1	-0.16 ± 0.01	0.06 ± 0.01
Sculptor	287.53	-83.16	83.9 ± 1.5	111.4 ± 0.1	0.081 ± 0.005	-0.136 ± 0.004
Sextans	243.51	42.27	92.5 ± 2.2	224.2 ± 0.1	-0.44 ± 0.02	0.09 ± 0.02
Carina I	260.11	-22.22	105.6 ± 5.4	222.9 ± 0.1	0.48 ± 0.01	0.13 ± 0.01
Fornax	237.26	-65.67	147.0 ± 9.0	55.3 ± 0.1	0.380 ± 0.002	-0.410 ± 0.004
LeoII	220.17	67.23	233.0 ± 15.0	78.5 ± 0.6	-0.12 ± 0.06	-0.17 ± 0.06
LeoI	225.98	49.12	258.2 ± 9.5	282.5 ± 0.1	-0.06 ± 0.07	-0.18 ± 0.08
AntliaII	264.86	11.25	132.3 ± 6.7	290.7 ± 0.5	-0.05 ± 0.04	0.04 ± 0.05
AquariusII	55.11	-53.01	107.9 ± 3.3	-71.1 ± 2.5	-0.0 ± 0.16	-0.2 ± 0.16
BootesI	358.09	69.64	66.0 ± 3.0	102.2 ± 0.8	-0.47 ± 0.04	-1.07 ± 0.03
BootesII	353.75	68.86	42.0 ± 1.6	-117.1 ± 7.6	-2.25 ± 0.21	-0.63 ± 0.15
Canes VenaticiI	74.32	79.82	210.0 ± 6.0	30.9 ± 0.6	-0.26 ± 0.05	-0.06 ± 0.03
CanesVenaticiII	113.58	82.70	160.0 ± 7.0	-128.9 ± 1.2	-0.34 ± 0.11	-0.35 ± 0.10
CarinaII	269.98	-17.14	37.4 ± 0.4	477.2 ± 1.2	1.84 ± 0.03	0.11 ± 0.03
CarinaIII	270.01	-16.85	27.8 ± 0.6	284.6 ± 3.25	2.99 ± 0.08	1.49 ± 0.1
ColumbaI	231.62	-28.88	182 ± 18	153.7 ± 5.0	0.21 ± 0.09	-0.14 ± 0.1
Coma BerenicesI	241.86	83.61	42.0 ± 1.5	98.1 ± 0.9	0.5 ± 0.05	-1.67 ± 0.04
CraterII	282.91	42.03	117.5 ± 1.1	87.5 ± 0.4	-0.17 ± 0.04	-0.09 ± 0.02
DracoII	98.29	42.88	20.0 ± 3.0	-347.6 ± 1.75	1.06 ± 0.17	0.96 ± 0.18
GrusI	338.68	-58.24	120.2 ± 11.1	-140.5 ± 2.0	-0.05 ± 0.12	-0.41 ± 0.14
GrusII	351.14	-51.94	53.2 ± 5.2	-110.0 ± 0.5	0.48 ± 0.06	-1.41 ± 0.09
Hercules	28.73	36.87	132.0 ± 6.0	45.2 ± 1.09	-0.13 ± 0.07	-0.39 ± 0.06
HorologiumI	271.39	-54.73	79.0 ± 7.0	112.8 ± 2.55	0.87 ± 0.05	-0.58 ± 0.05
HorologiumII	262.47	-54.14	78.3 ± 7.2	168.7 ± 12.9	0.89 ± 0.23	-0.21 ± 0.25
HydraII	295.62	30.46	151.0 ± 8.0	303.1 ± 1.4	-0.26 ± 0.13	-0.05 ± 0.12
HydrusI	297.42	-36.75	27.6 ± 0.5	80.4 ± 0.6	3.77 ± 0.03	-1.55 ± 0.03
LeoIV	265.44	56.51	154.0 ± 5.0	132.3 ± 1.4	-0.20 ± 0.13	-0.26 ± 0.12
LeoV	261.85	58.54	173.0 ± 5.0	172.1 ± 2.2	-0.11 ± 0.11	-0.21 ± 0.10
PiscesII	79.21	-47.11	183.0 ± 15.0	-226.5 ± 2.7	0.07 ± 0.11	-0.26 ± 0.11
ReticulumII	266.28	-49.72	31.4 ± 1.4	64.8 ± 0.5	2.39 ± 0.03	-1.3 ± 0.03
Reticulum_III	273.88	-45.65	92.0 ± 13.2	274.2 ± 7.5	0.05 ± 0.21	-0.09 ± 0.2
Sagittarius_II	18.94	-22.90	73.4 ± 1.0	-177.3 ± 1.2	-0.65 ± 0.07	-0.96 ± 0.04
SegueI	220.49	50.42	23.0 ± 2.0	208.5 ± 0.9	-1.59 ± 0.23	-3.5 ± 0.21
SegueII	149.43	-38.14	36.6 ± 2.45	-40.2 ± 0.9	1.68 ± 0.13	0.12 ± 0.08
TriangulumII	140.90	-23.83	28.4 ± 1.6	-381.7 ± 1.1	0.62 ± 0.15	0.42 ± 0.11
TucanaII	328.04	-52.35	57.5 ± 5.3	-129.1 ± 3.5	0.94 ± 0.05	-1.22 ± 0.06
TucanaIII	315.38	-56.18	25.0 ± 2.0	-102.3 ± 0.4	-0.02 ± 0.03	-1.67 ± 0.03
TucanaIV	313.29	-55.29	48.3 ± 4.2	15.9 ± 1.8	0.63 ± 0.13	-1.54 ± 0.11
TucanaV	316.31	-51.89	55.4 ± 8.7	-36.3 ± 2.5	-0.1 ± 0.2	-1.01 ± 0.23
Ursa MajorI	159.44	54.39	97.3 ± 5.85	-55.3 ± 1.4	-0.56 ± 0.06	-0.68 ± 0.08
Ursa MajorII	152.46	37.44	34.7 ± 2.1	-116.5 ± 1.9	1.72 ± 0.05	-1.84 ± 0.06
WillmanI	158.57	56.78	38.0 ± 7.0	-12.8 ± 1.0	0.36 ± 0.1	-1.04 ± 0.18

Chapter 3

Initial Setup

This chapter introduces the initial parameters used throughout the thesis. It will explain how the satellites are arranged around their host galaxy and how they are numerically integrated. Additionally, it also discusses how different ranges of uncertainties are chosen for Proper Motions and Distances along with different Milky Way potentials. This chapter serves as a comprehensive guide, shedding light on the fundamental aspects that form the basis of this work. All codes for this work used the Python programming language.

3.1 Plane Setup

To set up a plane of satellites, it is crucial to position the test satellites correctly in three dimensions. The shape of the distribution, whether it is flat or spherical, depends on how these satellites are arranged around the host galaxy. The initial conditions of these satellites play a significant role in forming a flat structure. For this research, I am using the Milky Way and its distribution of satellites as a reference. I aim to replicate a similar arrangement in this study. The Milky Way's plane of satellites, VPOS, has a radius of about 250 kpc and a root mean square thickness ranging from 20 to 30 kpc. To simulate this, I am using a cylindrical coordinate system to randomly generate $N_{\rm sat}$ test satellites, aligned with the co-orbiting satellite plane, with distance from the host galaxy, R, ranging from 20 to 250 kpc and height, z, between 0 and 20 kpc, and azimuthal angle, ϕ, ranging from 0 to 2π.

To generate the random values for the distance, R, the Von Neumann rejection algorithm, also known as rejection sampling, is used. It is a statistical technique used to generate random samples from a desired probability distribution. Generally, it involves three main steps:

- First, start generating a sample from a relatively simple distribution.
- Check whether the generated sample fits the target distribution. If it does, keep the sample you want to sample from. If not, reject it.
- If the generated sample is rejected, repeat the first step until a required acceptable sample is obtained.

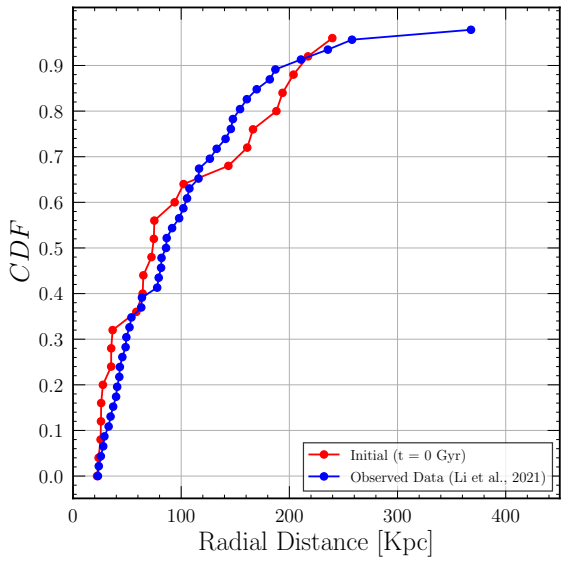

Figure 3.1: A graphical comparison of the radial distance distributions of satellite galaxies, contrasting simulated test satellites in our model with observed data. Figure Presents the Cumulative Distribution Function (CDF) for these two datasets.

To produce the radial distance distribution, the power-law distribution function is used:

$$f(r) = r^{\alpha} \tag{3.1}$$

The cumulative distribution function (CDF) for this is derived by integrating the radial density distribution function across a sphere, given by:

$$F(r) = \int f(r^{'}) \times 4\pi r^{'2} dr^{'} \tag{3.2}$$

From here, through inverse transform sampling or the inverse CDF method, the random samples corresponding to the radial distribution are drawn. In equation 3.2, $r^{'}$ is a variable of integration, and the multiplication with $4\pi r^{'2}$ accounts for the spherical volume element, r represents the radial distance, while α is an exponent dictating the behavior of the distribution in equation 3.1.

In this study, $\alpha = -3$, which indicates a higher likelihood of finding test satellites closer to the host galaxy. This effectively means that there is a denser concentration of satellite galaxies nearer to the host galaxy which decreases with large distances. This kind of distribution is useful for mimicking the observed distribution of the Milky Way's satellites. A Kolmogorov–Smirnov (K–S) test was conducted to compare the radial distribution of randomly generated test satellites with the distribution of observed satellites. The aim was to check if the two distributions were statistically similar. Upon analysis, the results indicated that the p-value obtained was greater than the significance threshold of 0.05. This suggests that there is no strong evidence to reject the null hypothesis, implying that the distributions of the randomly generated test satellites and the observed satellites do not exhibit significant differences, and the datasets may come from the same distribution. Figure 3.1 shows the CDF of a randomly generated radial distribution and that of the observed

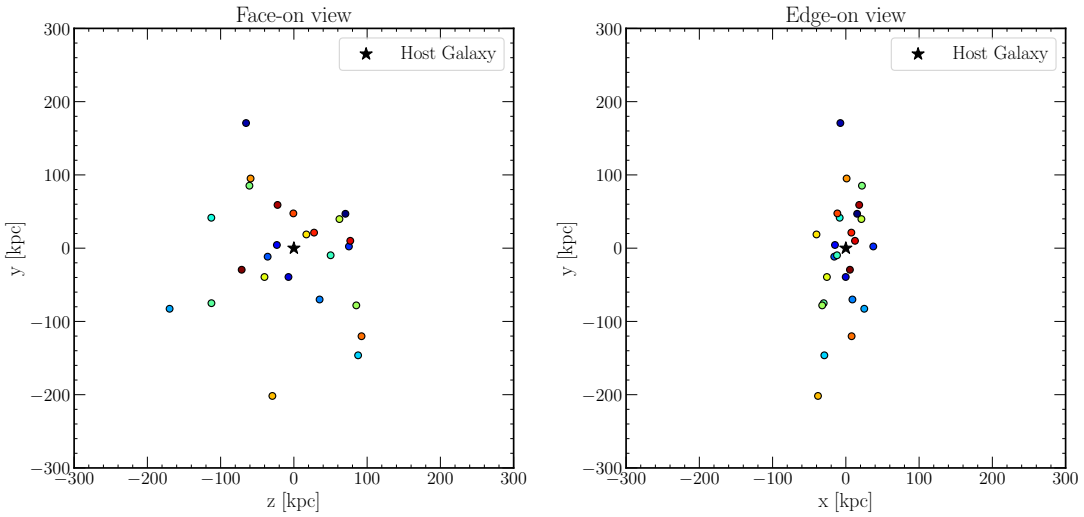

Figure 3.2: Face-on (left) and Edge-on (right) views of $N_{\text{sat}} = 25$ randomly generated test satellite points represented by different colors. Here, star symbol represents the host galaxy.

data.

Once the required random N_{sat} satellites arranged around a host galaxy, these are then converted to the Cartesian coordinate system, see Figure 3.2 for face-on and edge-on view of the randomly distributed $N_{\text{sat}} = 25$ test satellites around a host galaxy. With this step, the initial triaxility or the flatness of the system was measured by using the Tensor of Inertia method described in Chapter 2.

3.2 Velocities

In the simulation of the galaxy system, determining the velocities of the satellites is a fundamental aspect that drives their dynamic behavior. For that purpose, understanding the initial velocities of the satellites is a critical factor, because these initial velocities influence their subsequent trajectories within the simulated galaxy system. In the cylindrical coordinate system, each test satellite needs three unit vectors in three different directions - radial, tangential and perpendicular.

To get the radial unit vector for each satellite, the position vector is normalized. This helps in defining the direction in which a satellite is moving away from or towards the center of the galaxy.

$$\mathbf{r_i} = (\mathbf{x_i}, \mathbf{y_i}, \mathbf{z_i}) \tag{3.3}$$

$$|\mathbf{r_i}| = \sqrt{|\mathbf{x_{i|}^2} + |\mathbf{y_{i|}^2} + |\mathbf{z_{i|}^2}} \tag{3.4}$$

$$\hat{r}_i = \left(\frac{\mathbf{x_i}}{|\mathbf{r_i}|}, \frac{\mathbf{y_i}}{|\mathbf{r_i}|}, \frac{\mathbf{z_i}}{|\mathbf{r_i}|} \right) \tag{3.5}$$

Where $\hat{r}_i$ is the radial unit vector for satellite i. $\mathbf{x_i}$, $\mathbf{y_i}$, and $\mathbf{z_i}$ are the satellite's

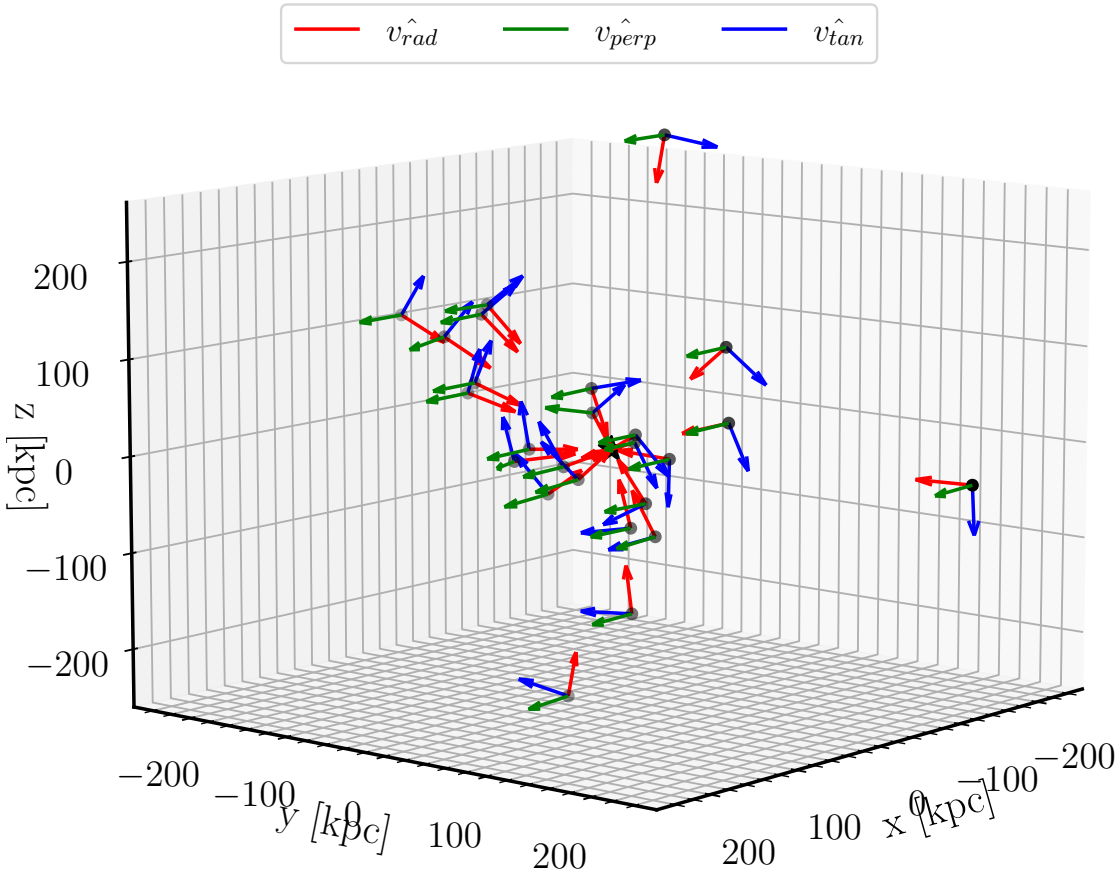

Figure 3.3: 3D plot of all $N_{\text{sat}} = 25$ randomly generated test satellites. For each satellite, radial, perpendicular and tangential velocity component is shown by red, green and blue color respectively. Where, host galaxy is represented by black star symbol at origin.

Cartesian coordinates and $|r_i|$ is the magnitude of the radial vector.

To find the unit vectors in the tangential direction, first I get the normal unit vector to the plane which can be obtained by using the Tensor of Inertia algorithm.

$$\hat{n} = (\hat{e_x}, \hat{e_y}, \hat{e_z}) \tag{3.6}$$

Then, using cross product of the radial unit vectors and the normal vector to the satellite plane, I get the tangential unit vectors.

$$\hat{t}_i = \hat{r}_i \times \hat{n} \tag{3.7}$$

Whereas, the perpendicular unit vectors can be obtained by calculating the cross product of radial and tangential units vectors.

$$\hat{p}_i = \hat{r}_i \times \hat{t} \tag{3.8}$$

In vector representation, they can be written as:

$$\mathbf{v}_{\mathrm{tan_i}} = |\mathbf{v}_{\mathrm{tan_i}}|.\hat{t}_i \tag{3.9}$$

$$\mathbf{v}_{\mathrm{rad_i}} = |\mathbf{v}_{\mathrm{rad_i}}|.\hat{r}_i \tag{3.10}$$

$$\mathbf{v}_{\mathrm{perp_i}} = |\mathbf{v}_{\mathrm{perp_i}}|.\hat{p}_i \tag{3.11}$$

Figure 3.3 displays the N_{sat} test satellites in 3D. For each satellite, three vectors – radial, perpendicular, and tangential – are illustrated, each represented by a different color. Initially, both $|\mathbf{v}_{\mathrm{perp_i}}|$ and $|\mathbf{v}_{\mathrm{rad_i}}|$ are set to zero, indicating no motion in radial and perpendicular directions. This means only the tangential component is relevant. Satellites are initialized with a tangential speed equal to the gravitational potential's circular velocity, guaranteeing the circular orbits. To make orbits eccentric, the tangential unit vectors of all satellites are rotated by an angle θ around the perpendicular unit vector, as shown in Table 3.2. For each test satellite, the values for θ are drawn from a uniform distribution. I used Rodrigues' rotation formula to rotate the tangential unit vector. To rotate $\hat{t}_i$ around $\hat{p}_i$, we cross $\hat{t}_i$ with $\mathbf{R}(\theta)$. Here, $\mathbf{R}(\theta)$ is:

$$\mathbf{R}_{\hat{\mathbf{u}}}(\theta) = e^{\widetilde{u}\theta} \tag{3.12}$$

$$\mathbf{R}_{\hat{\mathbf{u}}}(\theta) = \mathbf{I} + \widetilde{u}\sin\theta + \widetilde{u}^2(1-\cos\theta) \tag{3.13}$$

$$\mathbf{R}_{\hat{\mathbf{u}}}(\theta) = \begin{bmatrix} \cos(\theta) + u_x^2(1-\cos(\theta)) & u_x u_y(1-\cos(\theta)) - u_z\sin(\theta) & u_x u_z(1-\cos(\theta)) + u_y\sin(\theta) \\ u_y u_x(1-\cos(\theta)) + u_z\sin(\theta) & \cos(\theta) + u_y^2(1-\cos(\theta)) & u_y u_z(1-\cos(\theta)) - u_x\sin(\theta) \\ u_z u_x(1-\cos(\theta)) - u_y\sin(\theta) & u_z u_y(1-\cos(\theta)) + u_x\sin(\theta) & \cos(\theta) + u_z^2(1-\cos(\theta)) \end{bmatrix}. \tag{3.14}$$

where $\mathbf{I}$ is the 3×3 identity matrix and u us the antisymmetric matrix.

$$\widetilde{u} = \begin{bmatrix} 0 & -u_z & u_y \\ u_z & 0 & -u_x \\ -u_y & u_x & 0 \end{bmatrix} \tag{3.15}$$

Thus, the new tangential unit vector and tangential velocity becomes:

$$\hat{t}_{\theta,i} = \hat{t}_i \times \mathbf{R}_{\hat{\mathbf{u}}}(\theta) \tag{3.16}$$

$$\mathbf{v}_{\tan\,\theta_i} = |\mathbf{v}_{\mathrm{tan_i}}|.\hat{t}_{\theta,i} \tag{3.17}$$

Once I have the radial $\mathbf{v}_{\mathrm{rad_i}}$, perpendicular $\mathbf{v}_{\mathrm{perp_i}}$, and tangential $\mathbf{v}_{\mathrm{tan_i}}$ velocity components, I can convert them into the Cartesian coordinate system. This allows us to determine how the satellite is moving in the x, y, and z directions.

$$\mathbf{v}_{x,i} = \mathbf{v}_{\mathrm{rad}_{i,x}} + \mathbf{v}_{\tan\,\theta_{i,x}} + \mathbf{v}_{\mathrm{perp}_{i,x}} \tag{3.18}$$

$$\mathbf{v}_{y,i} = \mathbf{v}_{\mathrm{rad}_{i,y}} + \mathbf{v}_{\tan\,\theta_{i,y}} + \mathbf{v}_{\mathrm{perp}_{i,y}} \tag{3.19}$$

$$\mathbf{v}_{z,i} = \mathbf{v}_{\mathrm{rad}_{i,z}} + \mathbf{v}_{\tan\,\theta_{i,z}} + \mathbf{v}_{\mathrm{perp}_{i,z}} \tag{3.20}$$

These equations allow us to fully describe the motion of a satellite in the simulated galaxy system, taking into account its radial, tangential and perpendicular velocity components, as well as any eccentricities introduced into its orbit.

3.3 Integration

For the numerical integrations, I rely on `Galpy` (Bovy, 2015), which is a strong and helpful package in Python that offers many useful features. It provides a comprehensive range of functionalities to explore galaxy dynamics, including orbit integration, potential and force modeling, action-angle calculations, and coordinate transformations.

3.3.1 Milky Way Mass

For numerical integration, understanding the gravitational potential and mass distribution of the Milky Way is pivotal for integrating the orbits of test satellites. Despite extensive research over the past century, the exact distribution of the Milky Way's mass still remains a topic of debate. Various methods have been employed to estimate the total mass of the Milky Way, including the analysis of the orbits of the Magellanic Clouds, kinematic tracers such as globular clusters, stellar halo stars and satellite galaxies, the timing argument technique, and abundance-matching studies. Current results offer estimations between $0.5 - 3 \times 10^{12} M_{\odot}$, which vary based on the method used and the underlying assumptions made (Bland-Hawthorn and Gerhard, 2016).

The Milky Way's potential is complex, resulting from the combined contributions of the central nucleus, bulge, disk, and surrounding halo. While the nucleus, bulge, and disk are predominantly baryonic in nature, the exact nature of the halo remains unknown and is thought to be composed of dark matter. Due to its unknown nature, it becomes challenging to compute its exact mass directly, and its presence is inferred solely from its influence on its surroundings.

Wilkinson and Evans (1999) presented an estimation for the Milky Way mass within 50 kpc, approximating it at $M(50\mathrm{kpc}) = 0.54 \times 10^{12} M_{\odot}$. Using the data from the SDSS/SEGUE survey, Kafle et al. (2012) employed observations of Blue Horizontal Branch (BHB) stars to determine the MW's mass within a 25 kpc radius, yielding $M(25\mathrm{kpc}) = 0.21 \times 10^{12} M_{\odot}$, with an associated virial mass of $M_{vir} = 0.9 \times 10^{12} M_{\odot}$. Küpper et al. (2015) offered further insights, using data from the tidal stream of the MW globular cluster Palomar 5 to produce an estimate of $M(19\mathrm{kpc}) = 0.21$

$\times 10^{12} M_\odot$. Gaia revolutionized the data with significant improvements in parallaxes and proper motions, allowing for more accurate 3D velocity measurements. Thus, using globular cluster data from Gaia DR2, Posti and Helmi (2019) found it to be $M(20\text{kpc}) = 1.9 \times 10^{11} M_\odot$, with $M_{vir} = 1.3 \times 10^{12} M_\odot$. Similarly, again by using the Gaia DR2 data for halo globular clusters, they estimated the mass of the Milky Way to be $M(21.1\text{kpc}) = 0.2 \times 10^{12} M_\odot$, with $M_{vir} = 1.28 \times 10^{12} M_\odot$, and with combined samples from Gaia and HST they estimated it to be $M(39.5\text{kpc}) = 0.42 \times 10^{12} M_\odot$ and $M_{vir} = 1.54 \times 10^{12} M_\odot$ (Watkins et al., 2019). Later, using spectral data from APOGEE with photometric information from WISE, 2MASS, and Gaia, Eilers et al. (2019) found $M_{\text{vir}} = 7.25 \pm 0.25 \times 10^{11}\ M_\odot$. Following them, Labini et al. (2023), using Gaia DR3 data and the NFW halo model, estimated $M_{\text{vir}} = 6.5 \pm 3 \times 10^{11}\ M_\odot$ within a virial radius of $R_{\text{vir}} = 180 \pm 3$ kpc. Furthermore, Jiao et al. (2023), using Gaia DR3 data, found a sharp decrease in the rotational curves of the Milky Way between 19.5 and 26.5 kpc; by studying them, their total mass estimation of the Milky Way was revised downwards to $2.06^{+0.24}_{-0.13} \times 10^{11}\ M_\odot$ only.

Thus, significant uncertainty surrounds the mass of the Milky Way, making it imperative to account for these ambiguities in mass distribution. Understanding these uncertainties is crucial, as they directly affect our comprehension of the orbits of test satellites and, consequently, the inferred orbital stability of the plane of satellite galaxies. In response to this, my study utilizes three distinct mass models, each representing a specific Milky Way potential configuration, see Table 3.1.

Table 3.1: Milky Way models

Potential Model	Total Mass
MW_{less}	$4.8 \times 10^{11} M_\odot$
MW_{fiducial}	$8 \times 10^{11} M_\odot$
MW_{high}	$11.2 \times 10^{11} M_\odot$

3.3.2 Galaxy Potential

Within `Galpy`, the `galpy.potential` module features a built-in Milky Way-like potential model known as `MWPotential2014`, which represents our MW_{fiducial} model with a virial mass of $M_{\text{vir}} = 8.0 \times 10^{11} M_\odot$. The `MWPotential2014` is composed of several components, each following a distinct potential profile to represent different parts of the Milky Way. Specifically, the bulge component in `MWPotential2014` adopts a power-law density profile, named `PowerSphericalPotentialwCutoff`. The disk component is simulated using the `MiyamotoNagaiPotential` (Miyamoto and Nagai, 1975), and the dark matter halo is characterized by the `NFWPotential` (Navarro et al., 1997).

The Miyamoto-Nagai potential is defined by the equation:

$$\Phi(R, z) = -\frac{amp}{\sqrt{R^2 + (a + \sqrt{z^2 + b^2})^2}} \tag{3.21}$$

where *amp* signifies the amplitude with units of mass density, a is the scale radius, and b represents the scale height.

The Power-law density spherical potential with an exponential cut-off is given as:

$$\rho(r) = amp \left(\frac{r_1}{r}\right)^{\alpha} \exp\left(-\left(\frac{r}{r_c}\right)^2\right) \tag{3.22}$$

In this equation, *amp* is the amplitude, r_c is the cut-off radius, α indicates the inner power, and r_1 is the reference radius for the amplitude.

The NFW potential is expressed as:

$$\rho(r) = \frac{amp}{4\pi a^3} \frac{1}{(r/a)(1+r/a)^2} \tag{3.23}$$

Here, *amp* and a stand for amplitude and scale radius, respectively.

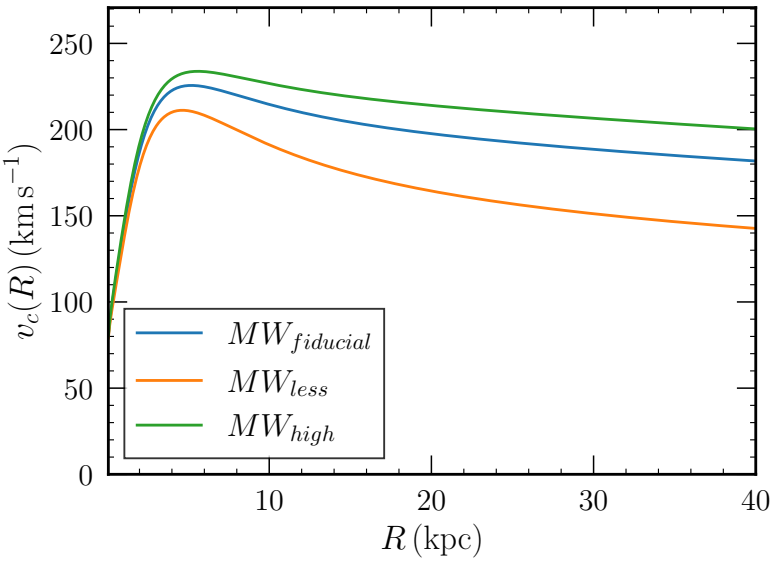

Figure 3.4: Rotational curves of the Milky Way for three different potential models: MW_{fiducial} (blue), MW_{less} (orange), and MW_{high} (green) as a function of radial distance (R) in kiloparsecs.

For the remaining two Milky Way potentials, the `MWPotential2014` is adjusted by scaling the halo mass to achieve the desired mass distribution. Particularly, MW_{less} model is configured with a halo mass 40% less than the MW_{fiducial} and MW_{high} is 40% greater than that of MW_{fiducial}. This method provides a deeper insight into the influence of mismatching mass of Milky Way on the behavior and formation of satellite galaxy systems. Figure 3.4 illustrates the rotation curves for the three MW models. In this figure, MW_{high} is depicted by the green curve, MW_{fiducial} by the blue curve, and MW_{less} by the orange curve. Notably, the green curve is flatter than the others. As we move further from the center, the velocity decrease is less pronounced than would be expected if only visible matter were present, suggesting a greater mass addition in the halo. In contrast, the orange curve, representing MW_{less}, shows a more pronounced decline with distance, indicating less

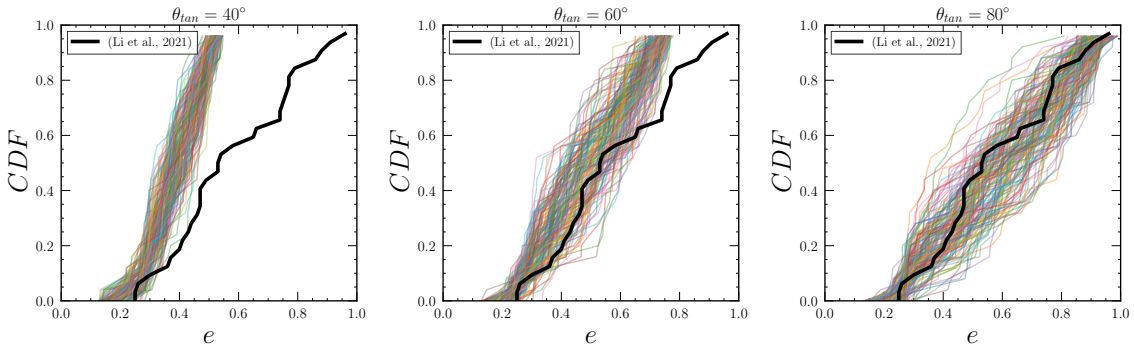

Figure 3.5: Comparison of eccentricity, (e), distributions across different θ: The figure presents the eccentricity CDF for three different θ_{tan}: 40°, 60°, and 80°from left to right, respectively. The predominant black histogram in each panel signifies observed data from (Li et al., 2021), while the overlaid colored CDF represent simulated results for $N_{\rm sat}$ test satellites.

mass in the halo. This steeper velocity drop at greater distances implies that this model accounts for less dark matter in the halo.

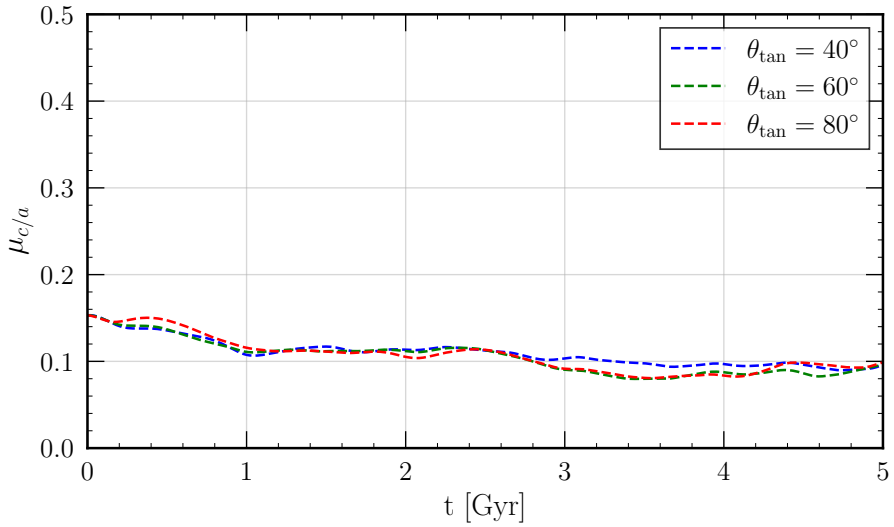

Figure 3.6: Plots showing the mean c/a of $N_{\rm realization}$ forward integration. Right: forward integration when $\theta = 40°$, center: forward integration when $\theta = 60°$, right: forward integration when $\theta = 80°$.

3.3.3 Forward Integration

To investigate the orbital properties of the simulated satellite galaxies, I integrated the system forward for 5 Gyr. Table 3.2 provides brief information on this forward integration. I performed the forward integration for $N_{\rm realization} = 20$ random realization of the initial setup for three different models. Each model has a different tangential velocity angle; the larger the angle, the more eccentric the orbit becomes. Each forward integration was conducted using the $MW_{\rm fiducial}$ potential model.

During the forward integration, the eccentricity for all the $N_{\rm sat}$ satellites across all $N_{\rm realization}$ realizations was analyzed. Figure 3.5 displays a comparison of eccentricity

distributions for $\theta_{tan} = 40°$, 60°, and 80°, from left to right, respectively. Apart from the black Cumulative Distribution Function (CDF), all other colored CDF represent N_{sat} test satellites. The eccentricity data for the observed Milky Way satellites from Li et al. (2021) is over-plotted, as indicated by the black CDF, to compare the simulated eccentricity with observed Milky Way satellite galaxies. From the graph, it is evident that the CDF range for Li et al. (2021) spans approximately 0.2 to 1.0. For the simulated eccentricity, the initial range is between 0.0 and 1.0, which implies that circular orbits were also included.

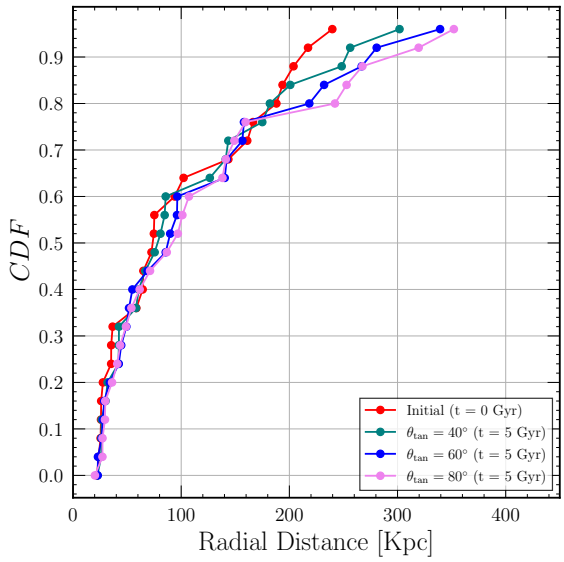

Figure 3.7: This figure illustrates the evolution of the cumulative distribution function (CDF) of radial distances. The red line represents the initial CDF of radial distances for random test satellites. The other three lines show the CDFs of the mean radial distance at 5 Gyr, each corresponding to a different θ_{tan}.

To align the simulated eccentricity of orbits with the observed data, values for all θ_{tan} were eventually drawn from a uniform distribution. However, values ranging between -20°and 20°were excluded to ensure that the contribution of circular orbits was disregarded. Figure 3.6 illustrates the mean minor-to-major axis ratio, $\mu_{c/a}$, across three θ_{tan} configurations. For all the θ_{tan}, $\mu_{c/a}$ lines initially start to decrease and after 2 Gyr [1], the plane remains stable until the 5 Gyr mark. This region shows decent stability and is suitable for the analysis of the plane of satellites after mock observing.

Furthermore, Figure 3.7 depicts the progression of the CDF for radial distances. It features a red line that illustrates the initial CDF for radial distances of randomly selected test satellites. Additionally, three other lines are present, each representing the CDF of the average radial distance at 5 Gyr for various values of θ_{tan}. Notably, there is an evident trend where an increase in θ_{tan} corresponds to a rightward shift in the mean CDF, suggesting that satellites tend to have a greater radial distance.

[1] 2 Gyr in Forward integration is 3 Gyr in Backward integration if total time of integration is 5 Gyr.

Table 3.2: Initial parameters for Forward Integration

Model	N_{sat}	θ_{tan}	Potential Model	$N_{\text{realization}}$	$\mu_{c/a}$ at 2 Gyr
FI-01	25	40°	MW_{fiducial}	20	0.113 ± 0.020
FI-02	25	60°	MW_{fiducial}	20	0.112 ± 0.011
FI-03	25	80°	MW_{fiducial}	20	0.105 ± 0.013

3.3.4 Uncertainties

As stated in Chapter 2 that one of the objectives of this project is to investigate the effect of uncertainties in proper motions and in distances. Thus these are the orbital properties which will be mocked observed. Table 3.3 shows the list of ranges of uncertainties in proper motions and in distances considered in this work. For proper motions, the uncertainties ranges is selected between none to extreme - 0 to 0.12 masyr^{-1}. This choice is motivated by the Gaia DR2 recorded proper motion uncertainties that approximate to 0.035 to 0.066 masyr^{-1}, which in Gaia ER3 is decreased to 0.0175 to 0.033 masyr^{-1}. Thus, it becomes good choice to test effect of uncertainties recorded by Gaia, as well as two extremes. Simultaneously, the range of uncertainties in distance is chosen between 0% to 5%. Again, 0% is chosen to test the system without any uncertainties, whereas approximately 5% is chosen because Li et al. (2021) reports an error of about 5% in their values for the observed Milky Way satellites. Thus, this gives a wide combinations of uncertainties in proper motion and distance to test, from no error to some extreme effects.

Table 3.3: Parameters for backward Integration with uncertainties for each model of Table 3.2.

Model	ϵ_μ [masyr^{-1}]	ϵ_{dist} [%]	$\text{Potential}_{\text{forward}}$	$\text{Potential}_{\text{backward}}$	$\text{M}_{\text{realization}}$
BI-01	±0.00	0	MW_{fiducial}	MW_{fiducial}	600
BI-02	±0.04	0	MW_{fiducial}	MW_{fiducial}	600
BI-03	±0.08	0	MW_{fiducial}	MW_{fiducial}	600
BI-04	±0.12	0	MW_{fiducial}	MW_{fiducial}	600
BI-05	±0.00	0	MW_{fiducial}	MW_{less}	600
BI-06	±0.04	0	MW_{fiducial}	MW_{less}	600
BI-07	±0.08	0	MW_{fiducial}	MW_{less}	600
BI-08	±0.12	0	MW_{fiducial}	MW_{less}	600
BI-09	±0.00	0	MW_{fiducial}	MW_{high}	600
BI-10	±0.04	0	MW_{fiducial}	MW_{high}	600
BI-11	±0.08	0	MW_{fiducial}	MW_{high}	600
BI-12	±0.12	0	MW_{fiducial}	MW_{high}	600
BI-13	±0.00	5	MW_{fiducial}	MW_{fiducial}	600
BI-14	±0.04	5	MW_{fiducial}	MW_{fiducial}	600
BI-15	±0.08	5	MW_{fiducial}	MW_{fiducial}	600
BI-16	±0.12	5	MW_{fiducial}	MW_{fiducial}	600
BI-17	±0.00	5	MW_{fiducial}	MW_{less}	600
BI-18	±0.04	5	MW_{fiducial}	MW_{less}	600
BI-19	±0.08	5	MW_{fiducial}	MW_{less}	600
BI-20	±0.12	5	MW_{fiducial}	MW_{less}	600
BI-21	±0.00	5	MW_{fiducial}	MW_{high}	600
BI-22	±0.04	5	MW_{fiducial}	MW_{high}	600
BI-23	±0.08	5	MW_{fiducial}	MW_{high}	600
BI-24	±0.12	5	MW_{fiducial}	MW_{high}	600

3.3.5 Backward Integration

After completing the forward integration, it is essential to record the orbital parameters such as right ascension, declination, proper motion in right ascension, proper motion in declination, distance, and line-of-sight velocity for each test satellite system at the final snapshot of all simulation realizations. This documentation is crucial as these parameters serve as the foundation for the subsequent mock observing and backward integration process. The backward integration begins by "mock observing" these parameters, which involves adding uncertainties to these recorded parameters.

$$\begin{aligned} \mu_{\alpha*_{\text{new}}} &= \mu_{\alpha*} + \epsilon_\mu \\ \mu_{\delta_{\text{new}}} &= \mu_\delta + \epsilon_\mu \\ \text{Dist}_{\text{new}} &= \text{Dist} + \epsilon_{\text{dist}} \end{aligned} \tag{3.24}$$

Equation 3.24 provides the updated proper motions and distance parameters, incorporating their respective uncertainties. For ϵ_μ, the random uncertainties are drawn from the Gaussian distribution with a width corresponding to the selected error. In contrast, for ϵ_{dist}, a percentage error is chosen. Table 3.3 details the ranges of uncertainties in these parameters. Following mocked observations, the system is integrated backward for 5 Gyr, repeating this process $M_{\text{realization}} = 30$ times for each of the 20 forward integrations (resulting in 600 total backward integrations) to return to its initial state. This procedure is conducted using three different Milky Way potential models, with their masses detailed in Table 3.1. Each row in Table 3.1 represents a combination of various parameters that could influence the inferred stability of the satellite plane. Overall, with 4 proper motion uncertainties, 2 distance uncertainties, and 3 potential models, there are 24 model combinations for each θ_{tan}. Each model undergoes 600 backward integrations, amounting to a total of 43,200 backward integrations. The results of these integrations will be presented in the next chapter.

Chapter 4

Results and Discussion

This chapter presents an analysis of my simulation results that are crucial for understanding the stability of the satellite's plane. The chapter is organized into distinct sections, each one dedicated to a different aspect of the study. Section 4.1 investigates the solely effect of uncertainties in proper motion on the satellite's plane. Section 4.2 focuses on the effect of distance uncertainties only. Section 4.3 explores the influence of various Milky Way potentials on orbital stability. Lastly, Section 4.4 examines the combined effects of all three types of errors to evaluate their collective influence [1].

The findings discussed in this chapter are based on simulations using the most eccentric model setup for forward integration - $\theta_{tan} = 80°$- which closely resembles the observed eccentricity of Milky Way satellites. Discussions regarding simulations with less eccentric orbits are detailed in the Appendix A.

4.1 Proper Motion Uncertainties

This section presents the results from simulations focusing exclusively on the role of uncertainties in proper motion on the inferred stability of the orbital plane. As defined in Chapter 3, the backward integrations were performed with proper motion uncertainties ranging from 0.00 to 0.12 masyr^{-1}, incrementing in steps of 0.04 masyr^{-1}. Furthermore, the backward integrations were carried out using the $MW_{\rm fiducial}$ potential, the same as that used in the forward integrations. Figure 4.1 shows the results in four panels, each corresponding to a distinct level of proper motion uncertainty. Within each panel, the x-axis represents the time evolution, with forward integrations extending from left to right and backward integrations from right to left, while the y-axis depicts the minor-to-major axis ratio of the orbital plane. The average of the 20 forward integrations is represented by the black dash-dotted line in each panel, with the individual forward integrations represented by gray lines. For each set of 20 forward simulations, there are 30 backward integrations, resulting in a total of 600 backward integrations, which are represented in a light green color, while the average of these 600 backward integrations is indicated

[1] Click here to see the playlist of movies illustrating the evolution of test satellites for backward integration.

by the green dashed line in each panel. Similary, Table 4.1 is an extended version of Table 3.3 and quantitatively translates the outputs of $\mu_{c/a}$. It includes two extra columns: $\Delta_{c/a}$, which represents the difference between $\mu_{c/a}$ from backward integration compared to forward integration after 3 Gyr in backward, and $f_{c/a}$, denoting the fractional change of $\mu_{c/a}$ in backward integrations compared to forward integrations.

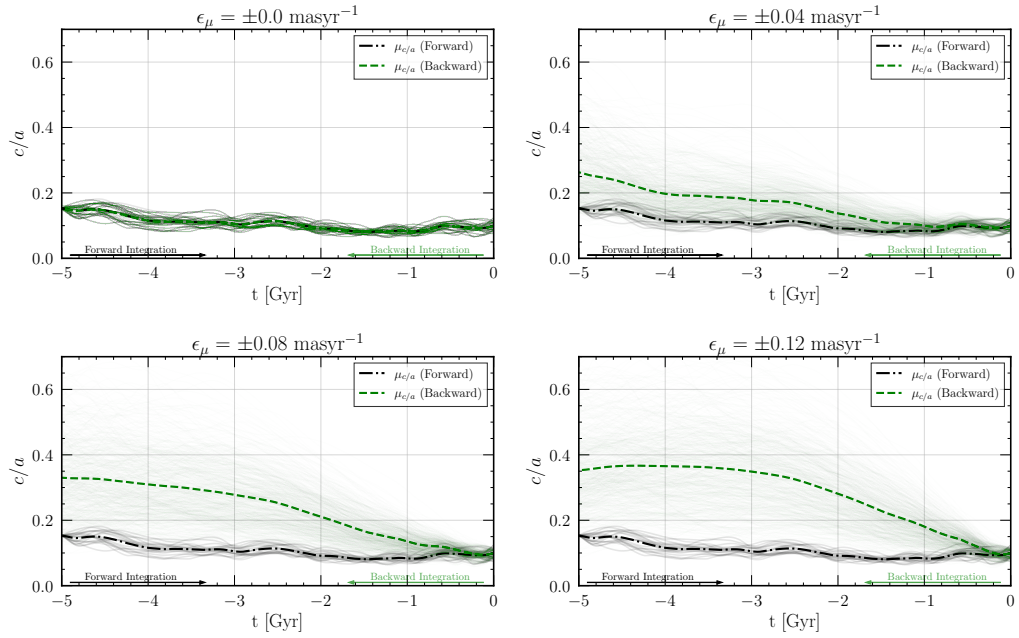

Figure 4.1: Four panels illustrating the influence of proper motion uncertainties on the plane of satellite galaxies. Each panel shows forward (black dashed lines) and backward (green dashed lines) integrations, also indicated by arrows. The uncertainties in proper motions are as follows: 0.00 masyr^{-1} in the upper left panel, 0.04 masyr^{-1} in the upper right panel, 0.08 masyr^{-1} in the lower left panel, and 0.12 masyr^{-1} in the lower right panel.

The upper left panel in Figure 4.1 illustrates the simulation outcomes when the proper motion error, ϵ_μ, is set to 0.00 masyr^{-1}. Under this condition, the mean minor-to-major ratio, $\mu_{c/a}$, obtained from backward integrations, aligns perfectly well with the mean minor-to-major ratio, $\mu_{c/a}$, obtained from the forward integrations, as shown in Figure 4.1, where each forward integration line is over-plotted by the backward integrations. This shows a high degree of predictability and suggests that the orbital plane remains stable and unaltered in scenarios where the proper motion are measured with perfect accuracy. It also implies that, at least in the theoretical framework of the simulation, the inherent dynamics of the satellite system are deterministic enough to allow for precise backtracking of its orbital path when initial conditions are precisely known. These results serve as a control scenario against which the other panels, which include some amount of proper motion errors, can be compared. Model BI-01 from Table 4.1 shows similar behavior in that, even after 3 Gyr of backward integration, the difference between forward and backward, $\Delta_{c/a} = 0.000$ masyr^{-1}, and $f_{c/a} = 1.000$, meaning that both forward and backward integration yield the same output when proper motion uncertainties remain at 0.000 masyr^{-1}.

Table 4.1: Combined parameters and metrics for backward integration models at 3 Gyr for $\theta_{tan} = 80°$, see Table A.1 and Table A.2 for $\theta_{tan} = 40°$and $60°$respectively.

Model	ϵ_μ [masyr^{-1}]	ϵ_{dist} [%]	Potential$_{\text{backward}}$	$\Delta_{c/a}$ [masy^{-1}]	$f_{c/a}$	$N_{\text{sat}} > 300$ kpc
BI-01	± 0.00	0	MW_{fiducial}	0.000 ± 0.013	1.000 ± 0.121	1.400 ± 0.917
BI-02	± 0.04	0	MW_{fiducial}	0.073 ± 0.053	1.694 ± 0.509	1.533 ± 1.013
BI-03	± 0.08	0	MW_{fiducial}	0.173 ± 0.091	2.641 ± 0.866	1.968 ± 1.096
BI-04	± 0.12	0	MW_{fiducial}	0.244 ± 0.112	3.316 ± 1.065	2.573 ± 1.142
BI-05	± 0.00	0	MW_{less}	0.028 ± 0.046	1.270 ± 0.436	6.400 ± 1.497
BI-06	± 0.04	0	MW_{less}	0.064 ± 0.049	1.612 ± 0.469	6.627 ± 1.459
BI-07	± 0.08	0	MW_{less}	0.132 ± 0.071	2.258 ± 0.676	7.033 ± 1.384
BI-08	± 0.12	0	MW_{less}	0.207 ± 0.098	2.968 ± 0.934	7.363 ± 1.433
BI-09	± 0.00	0	MW_{high}	0.014 ± 0.017	1.132 ± 0.160	0.350 ± 0.477
BI-10	± 0.04	0	MW_{high}	0.098 ± 0.061	1.932 ± 0.577	0.508 ± 0.594
BI-11	± 0.08	0	MW_{high}	0.208 ± 0.102	2.977 ± 0.974	0.910 ± 0.791
BI-12	± 0.12	0	MW_{high}	0.257 ± 0.107	3.445 ± 1.019	1.510 ± 0.934
BI-13	± 0.00	5	MW_{fiducial}	0.018 ± 0.019	1.168 ± 0.184	2.050 ± 1.071
BI-14	± 0.04	5	MW_{fiducial}	0.082 ± 0.053	1.779 ± 0.506	2.353 ± 1.119
BI-15	± 0.08	5	MW_{fiducial}	0.177 ± 0.090	2.680 ± 0.858	2.900 ± 1.136
BI-16	± 0.12	5	MW_{fiducial}	0.243 ± 0.111	3.315 ± 1.062	3.612 ± 1.165
BI-17	± 0.00	5	MW_{less}	0.054 ± 0.060	1.512 ± 0.572	8.100 ± 1.578
BI-18	± 0.04	5	MW_{less}	0.084 ± 0.060	1.803 ± 0.570	8.337 ± 1.524
BI-19	± 0.08	5	MW_{less}	0.148 ± 0.075	2.407 ± 0.711	8.610 ± 1.530
BI-20	± 0.12	5	MW_{less}	0.205 ± 0.083	2.950 ± 0.792	8.915 ± 1.538
BI-21	± 0.00	5	MW_{high}	0.017 ± 0.022	1.163 ± 0.208	0.900 ± 0.768
BI-22	± 0.04	5	MW_{high}	0.099 ± 0.064	1.944 ± 0.608	0.920 ± 0.742
BI-23	± 0.08	5	MW_{high}	0.207 ± 0.102	2.965 ± 0.971	1.357 ± 0.905
BI-24	± 0.12	5	MW_{high}	0.259 ± 0.111	3.460 ± 1.053	1.965 ± 1.022

In the upper right panel at the level of the Gaia systamatic uncertainties, ϵ_μ, is set to 0.04 masyr^{-1}. Here, a slight uncertainty in proper motion leads to a visible divergence between the mean axial ratios of forward and backward integrations. The mean axial ratio, $\mu_{c/a}$, from the backward integration does not align as closely with the forward integration as it did in the first case, when there were no uncertainties. This suggests a decrease in the predictability and inferred stability of the orbital plane with the introduction of proper motion errors. Furthermore, the scatter of individual backward c/a values around the mean increases. This is also evident from Model BI-02 in Table 4.1, which shows that with the introduction of $\epsilon_\mu = 0.04$ masyr^{-1}, $\Delta_{c/a}$ shifts from 0.000 masyr^{-1} to 0.073 masyr^{-1}, and $f_{c/a}$ becomes 1.694.

In the lower left panel, proper motion uncertainties are increased to 0.08 masyr^{-1}. In this scenario, there is a further widening gap between the means of backward and forward integrations, as illustrated by the greater separation of the dashed lines. The mean axial ratio, $\mu_{c/a}$, from backward integration shows a more pronounced deviation from the mean axial ratio of the forward integration. This indicates a further decline in the predictability and stability of the orbital plane as proper motion uncertainty increases. Additionally, the individual backward integration lines are more scattered, demonstrating that the uncertainties are beginning to have a dominate impact on the inferred stability of the satellite plane. Moreover, Table 4.1 also validates that in Model BI-03, $\Delta_{c/a}$ shifts yet again from 0.073 masyr^{-1} to 0.173 masyr^{-1}, and $f_{c/a}$ doubles.

In the lower right panel, where the proper motion error reaches 0.12 masyr^{-1}, the divergence between the forward and backward integration means, shown by the dashed lines, is the most pronounced of all cases presented. The mean axial ratio, $\mu_{c/a}$, from backward integration shows a significant divergence from the forward integration mean, implying a severe reduction in the orbital plane's predictability

and stability with the highest proper motion uncertainty examined. Moreover, the scatter of individual backward c/a is the most wide. It shows that the system's dynamics are highly chaotic under such uncertainties, making reliable influences on the satellite's orbital evolution becomes impossible. This case is represented by Model BI-04 of Table 4.1, it shows that $\Delta_{c/a} = 0.244$ masyr^{-1} and $f_{c/a} = 3.316$.

The left panel in Figures 4.2 and 4.3 illustrates $\Delta_{c/a}$ and $f_{c/a}$ as functions of proper motion uncertainties, respectively [2]. Each figure also demonstrates the impact of θ_{tan} at 40°, 60°, and 80°. These figures reveal that an increase in proper motion uncertainties results in higher values of $\Delta_{c/a}$ and $f_{c/a}$ across all θ_{tan} values. However, a greater increase in θ_{tan} shows a more pronounced impact. The points there seem to have a linear behaviour, so we fitted a line and the R-square of the fiited line comes out to be between 0.9 - 1.0 for all the cases, indicates that both $\Delta_{c/a}$ and $f_{c/a}$ increases liearly with proper motion uncertainties, see Table A.3. For a detailed analysis of θ_{tan} at 40° and 60°, please refer to Appendix A.1.

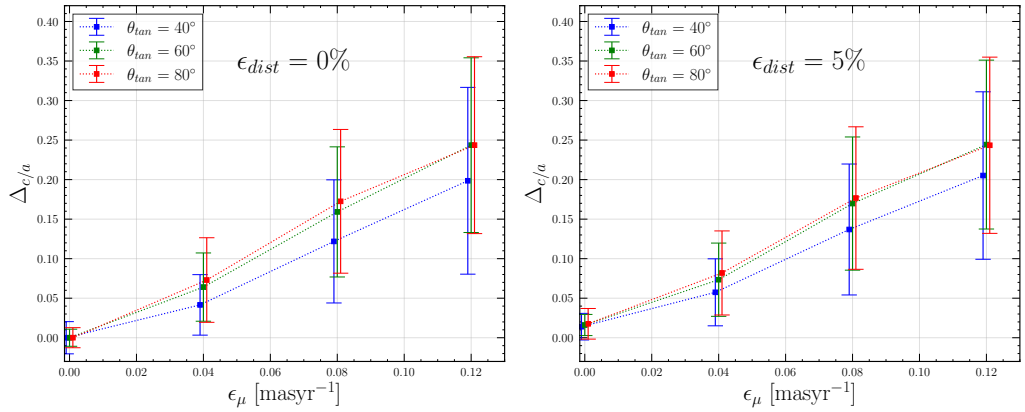

Figure 4.2: Two figures illustrate $\Delta_{c/a}$ as a function of proper motion errors under MW_{fiducial}. Within each figure, the effect of eccentricities is represented by lines with error bars. The left figure represents Model BI-01 to BI-04, and the right figure represents Model BI-013 to BI0-16, as detailed in Table 4.1.

4.2 Distance Uncertainties

This section presents the results involving uncertainties in distances. Figure 4.4 depicts the evolution of the orbital plane. The mean of c/a for forward integration is shown in a dotted-dashed black color. Whereas, for backward integration, two dashed lines are present: the first, without distance uncertainties — 0% represented in blue color, and the second introduces a 5% uncertainty in distances, represented in green color. The analysis of the former is already presented in section 4.1, which represents an ideal state with high predictability and stability for the test satellite's plane. However, with the introduction of a 5% distance error — while maintaining the proper motion error at zero — a new variable is added to the simulation. There

[2]Here the positions of the error bars for each line slightly along the x-axis has been adjusted so that error bars that don't overlap wit each other.

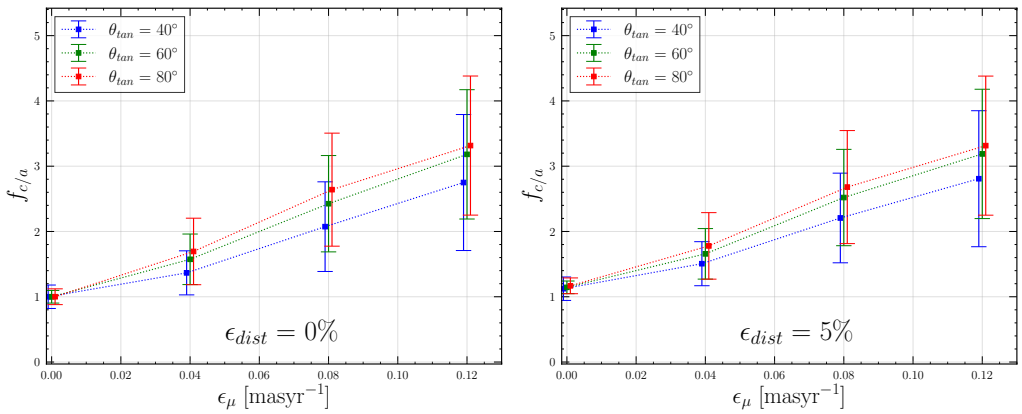

Figure 4.3: Two figures illustrate $f_{c/a}$ as a function of proper motion errors under MW_{fiducial}. Within each figure, the effect of eccentricities is represented by lines with error bars. The left figure represents Model BI-01 to BI-04, and the right figure represents Model BI-013 to BI0-16, as detailed in Table 4.1.

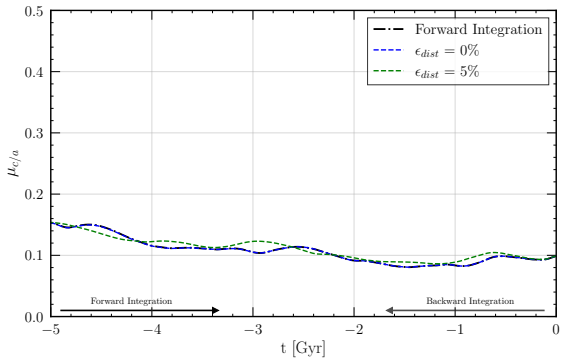

Figure 4.4: The figure illustrates the impact of distance uncertainties on the orbital plane stability of satellite galaxies. The forward integration is represented by a dotted-dashed black line. In the case of 0% distance uncertainty, the backward integration closely follows the forward integration, shown in blue. However, with 5% distance uncertainty, the backward integration, depicted in green, shows a noticeable divergence in $\mu_{c/a}$ compared to the forward integration.

is a noticeable effect of distance uncertainties; the system does not return to its original state but instead experiences a slight change. Despite this, there is still decent agreement between the mean backward $\mu_{c/a}$ and forward $\mu_{c/a}$ integrations, suggesting that the inferred fundamental orbital evolution is not drastically impacted, even with the introduction of 5% uncertainties in the distances of the test satellites. It is also evident from Table 4.1, comparing Model BI-01 and B1-13, both $\Delta_{c/a}$ and $f_{c/a}$ have changed just slightly from 0.000 masyr^{-1} to 0.018 masyr^{-1} and 1.000 to 1.168 respectively after 3 Gyr of backward integration.

4.3 Milky Way Model

In the study of galactic dynamics, particularly the stability and evolution of satellite planes, the potential model adopted for the Milky Way plays a crucial role. Figure 4.5 shows the influence of different Milky Way mass models on the inferred stability

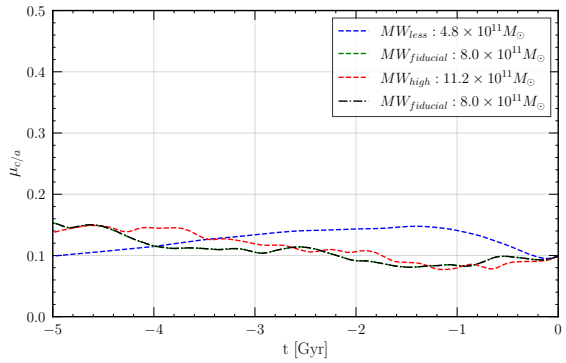

Figure 4.5: This figure illustrates the $\mu_{c/a}$ for forward integrations, shown as dotted-dash lines, alongside $\mu_{c/a}$ for backward integration under three Milky Way models, characterized by halo mass. The blue, green, and red dashed lines represent the $\mu_{c/a}$ under $MW_{\rm less}$, $MW_{\rm fiducial}$, and $MW_{\rm high}$ potential models, respectively.

of a satellite plane. By not taking into account uncertainties in proper motion and distance, the results provide a clear picture of the satellite plane's fundamental dynamical behavior when subjected to different Milky Way potential models. The x-axis shows the time evolution, while the y-axis represents the $\mu_{c/a}$ of plane of satellite obtained from the simulations. The black dotted-dashed lines represents the mean of forward integration under a $MW_{\rm fiducial}$ potential. In contrast, the colored lines depict the mean backward integration under different Milky Way potentials. The backward integrations, particularly the green line representing the same $MW_{\rm fiducial}$ potential, demonstrates a perfect consistency with its forward counterpart, implying a stable evolution when the Milky Way potential is same, also seen in Model BI-01 in Table 4.1 that $\Delta_{c/a}$ that is remains 0.000 masyr^{-1} even after 3 Gyr, and $f_{c/a}$ = 1.000 . This scenario serves as a benchmark for stability against which other models are compared. The red line, representing the $MW_{\rm high}$ model, exhibits a reasonable degree of stability, although it does not completely resembles the forward integration, suggesting some sensitivity to the Milky Way's mass assumptions. This difference is shown in BI-09 of Table 4.1, that shows $\Delta_{c/a} = 0.014$ masyr^{-1} after 3 Gyr, and $f_{c/a} = 1.132$. The blue line, representing the $MW_{\rm less}$ mass model, shows a marked divergence from the other models. Its $\mu_{c/a}$ initially increases followed by a flattening trend in the $\mu_{c/a}$ ratio, this could imply a different dynamical history for the plane of satellites within such a lower-mass Milky Way potential. Here, for lower-mass Milky Way potential, $\Delta_{c/a} = 0.028$ masyr^{-1} after 3 Gyr, and $f_{c/a} = 1.270$.

These observations underscore the impact of Milky Way mass models on the dynamical interpretations of satellite planes. The correlation between the mass of the Milky Way and the behavior of satellite planes is evident, where higher mass models tend to show a more stable evolution compared to lower mass models.The precise measurement of the Milky Way's mass is thus essential for accurate simulations and predictions of satellite plane behaviors, which could have broader implications for understanding galactic formation and evolution.

4.4 Combined Effect

This section presents a complex scenario combining proper motion uncertainties with three distinct Milky Way potential models to assess the stability of the satellite plane. Figure 4.6 illustrates the impact of varying degrees of proper motion uncertainty on the predicted flatness of the satellite distribution over time, with uncertainties ranging from 0.00 to 0.12 masyr^{-1}. Each panel further shows the impact of Milky Way models on the plane. The analysis for $MW_{\rm fiducial}$ have been thoroughly discussed in section 4.1. As for the $MW_{\rm high}$ model, it generally follows a similar trend to $MW_{\rm fiducial}$, but with slightly larger $\mu_{c/a}$ values in the three scenarios of proper motion uncertainty due to its higher halo mass, as can be seen in Table 4.1 that both $\Delta_{c/a}$ and $f_{c/a}$ for $MW_{\rm high}$ is slightly larger than the $MW_{\rm fiducial}$. However, in the last panel, where ϵ_μ values are at their extreme (0.12 masyr^{-1}), the $\mu_{c/a}$ for both $MW_{\rm fiducial}$ and $MW_{\rm high}$ models appears to be identical. Additionally, Table 4.1 demonstrates that proper motions have a significant effect on both models, and this effect intensifies with an increase in proper motion errors. This trend is also evident in both $\Delta_{c/a}$ and $f_{c/a}$, as they increase with rising proper motion errors (see Model BI-01 to BI-04 for $MW_{\rm fiducial}$ and BI-09 to BI-012 for $MW_{\rm high}$).

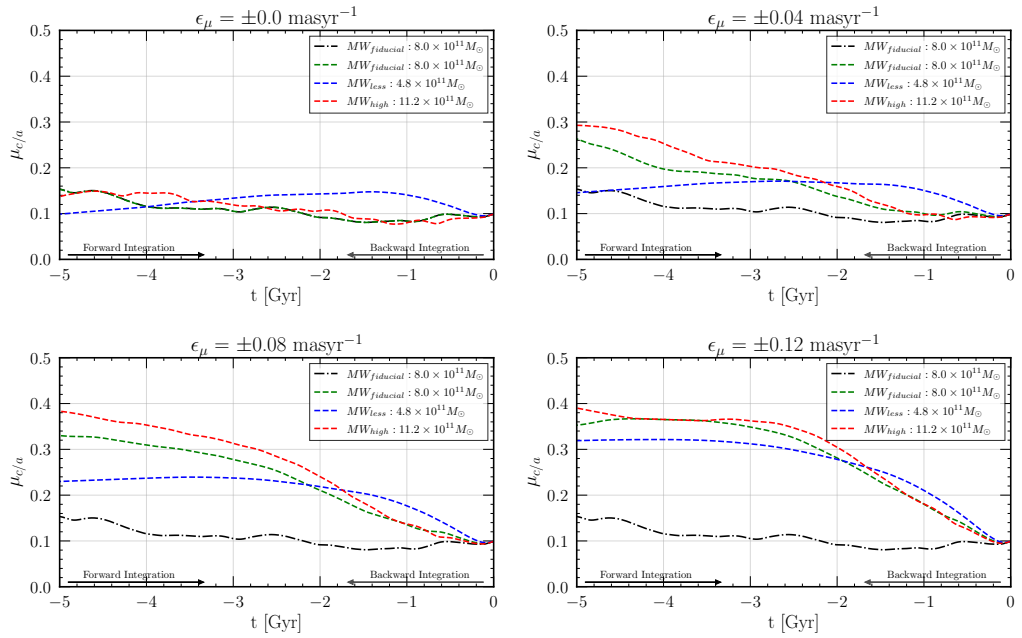

Figure 4.6: This figure comprises four panels, each highlighting the effect of proper motion uncertainties, ranging from 0.00 to 0.12 masyr^{-1}, on the evolution of $\mu_{c/a}$. Each panel also demonstrates the influence of using different Milky Way potential models — $MW_{\rm less}$, $MW_{\rm fiducial}$, and $MW_{\rm high}$ — on the plane's flattening.

$MW_{\rm less}$ exhibits a different impact. For all proper motion uncertainties, the $\mu_{c/a}$ initially increases, but after a certain period, the trend starts to flatten. Except for $\epsilon_\mu = 0.000$ masyr^{-1}, the evolution of $\mu_{c/a}$ under all the other cases remains smaller than the other two Miky Way models. From Table 4.1, both $\Delta_{c/a}$ and $f_{c/a}$ shows smaller values than those of $MW_{\rm high}$ and $MW_{\rm fiducial}$.

Furthermore, the evolution of the satellite plane with 0.12 masyr^{-1} proper motion

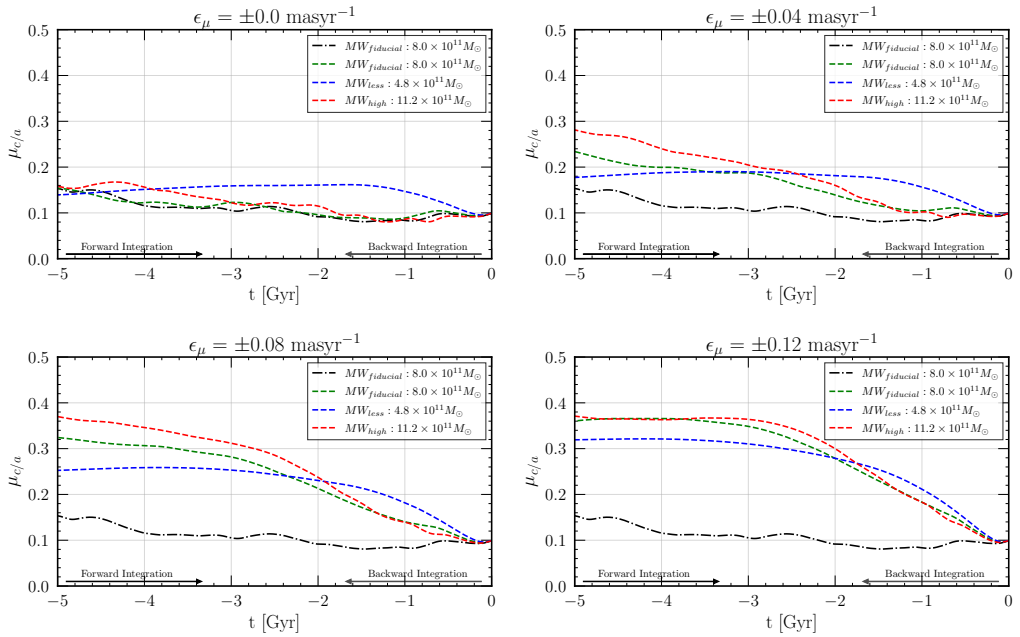

Figure 4.7: This figure is akin to Figure 4.6, but it now includes distance uncertainties. It consists of four panels, each highlighting the effects of different proper motion uncertainties, ranging from 0.00 to 0.12 masyr^{-1}, on the evolution of $\mu_{c/a}$. Furthermore, each panel sheds light on how varying Milky Way potential models — MW_{less}, MW_{fiducial}, and MW_{high} — influence the flattening of the plane.

uncertainty appears to show a same trend across all three Milky Way models: an initial increase followed by a flattening trend in the $\mu_{c/a}$ values, but with a wider spread, suggesting that higher proper motion uncertainties overshadow the effect of different Milky Way models, at least for MW_{fiducial} and MW_{high}. This observation indicates that, at higher levels of proper motion uncertainty, the distinctions between the various Milky Way potential models become less pronounced, as the increased uncertainty tends to dominate the dynamics of the satellite plane.

Building upon this understanding, Figure 4.7 introduces an additional layer of complexity by incorporating distance errors into the analysis. The upper left panel depicts the effect of distance uncertainties on the plane of satellite galaxies within three Milky Way models. The $\mu_{c/a}$ for backward integration, obtained from the MW_{fiducial}, is analyzed in 4.2, where it shows a slight deviation from the forward integration, as indicated by the black dashed line. Although the effect is not significant, it is still noticeable. A similar impact of distance uncertainties is observed in the $\mu_{c/a}$ of MW_{high} and MW_{less}, where it slightly increases the axial ratio from the forward integration. In the remaining three panels, uncertainties in proper motion, specifically 0.04, 0.08, and 0.12 masyr^{-1}, are introduced. These panels display results incorporating both proper motion and distance uncertainties across the three Milky Way models. The behavior in these three panels is consistent with that observed in Figure 4.6, showing an additional, minor increase in the $\mu_{c/a}$ ratio for all three Milky Way models due to the inclusion of distance uncertainties. Models BI-13 to BI-24, shows this behaviour when 5% of uncertainties were induced, although there is not prominent impact. A comparison of the left ($\epsilon_{dist} = 0\%$) and right (ϵ_{dist}

= 5%) panels in Figures 4.2 and 4.3 also reveals a notable impact of distance errors. However, these errors did not significantly alter the plane of the satellite.

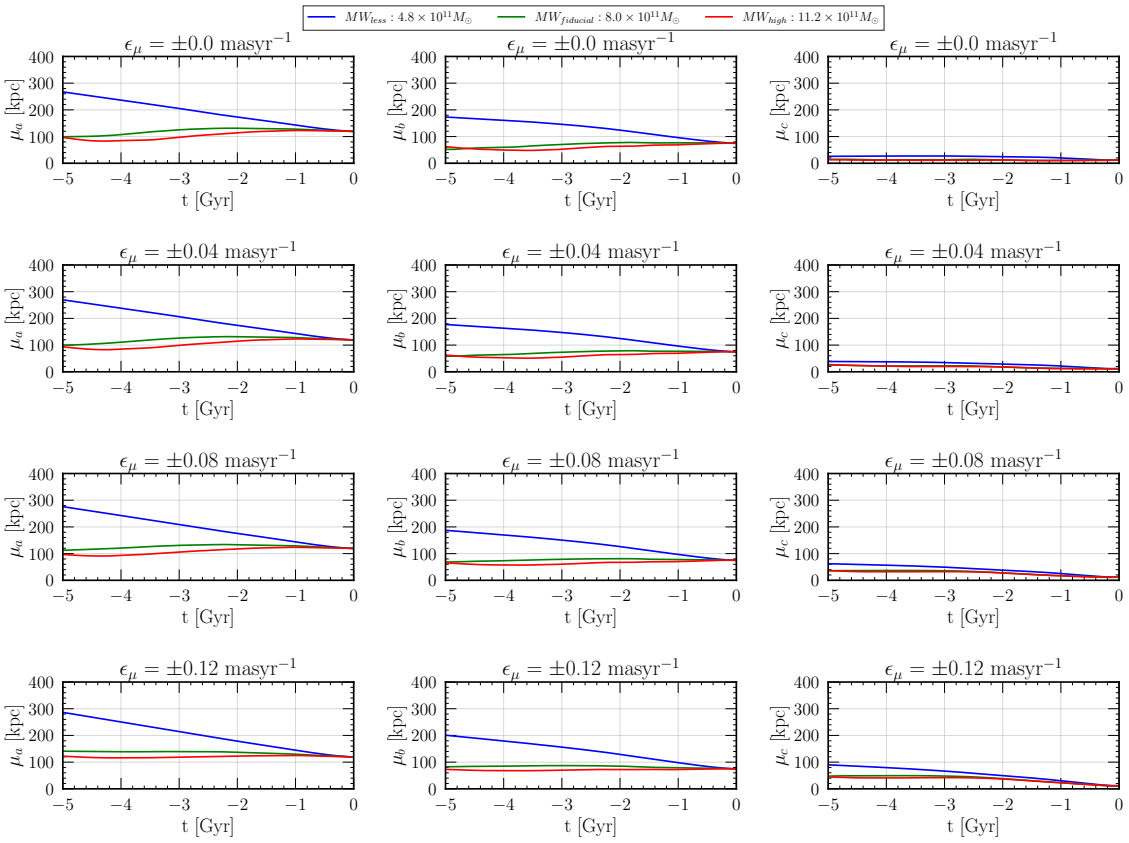

Figure 4.8: Figure shows the comparative analysis of galactic orbital axes under Varying proper motion uncertainties and Milky Way Models. This figure illustrates the mean values of 600 major, minor, and intermediate axes calculated through backward integration. It is organized into 12 panels, each representing a different combination of proper motion uncertainty (ranging from 0.00 to 0.12 masyr^{-1}) and Milky Way model. The rows indicate the varying levels of proper motion uncertainty, while each column corresponds to one of the three axes: major (first column), intermediate (second column), and minor (third column). The influence of different Milky Way models is denoted by distinct colors as per the legend, allowing for a clear comparison of their impacts on the galactic orbital axes over time.

4.5 Analysis of Individual Axes

The behavior of the minor-to-major axial ratio, $\mu_{c/a}$, in the $MW_{\rm less}$ Milky Way potential model differs from other models, warranting a closer examination of how the extent of the test satellite system changes along its different axes, from major to minor. Figure 4.8 illustrates the influence of proper motion errors on the mean values of the three axes: a (major axis), b (intermediate axis), and c (minor axis). The influence of proper motion is presented row-wise, while the axes are displayed column-wise in the figure. Each panel further depicts three lines representing the axes derived from backward integration using three distinct Milky Way potentials. The impact of using different Milky Way potentials is quite evident, particularly

in the $MW_{\rm less}$ model, which has a smaller halo mass. Under this model, with zero proper motion uncertainties, the mean of both the major and intermediate axes exhibit a pronounced increase over time, whereas the minor axis increases slowly. In contrast, $MW_{\rm fiducial}$ and $MW_{\rm high}$ models demonstrate distinct patterns in the major and intermediate axes compared to the $MW_{\rm less}$ model, while their minor axes show similar behavior.

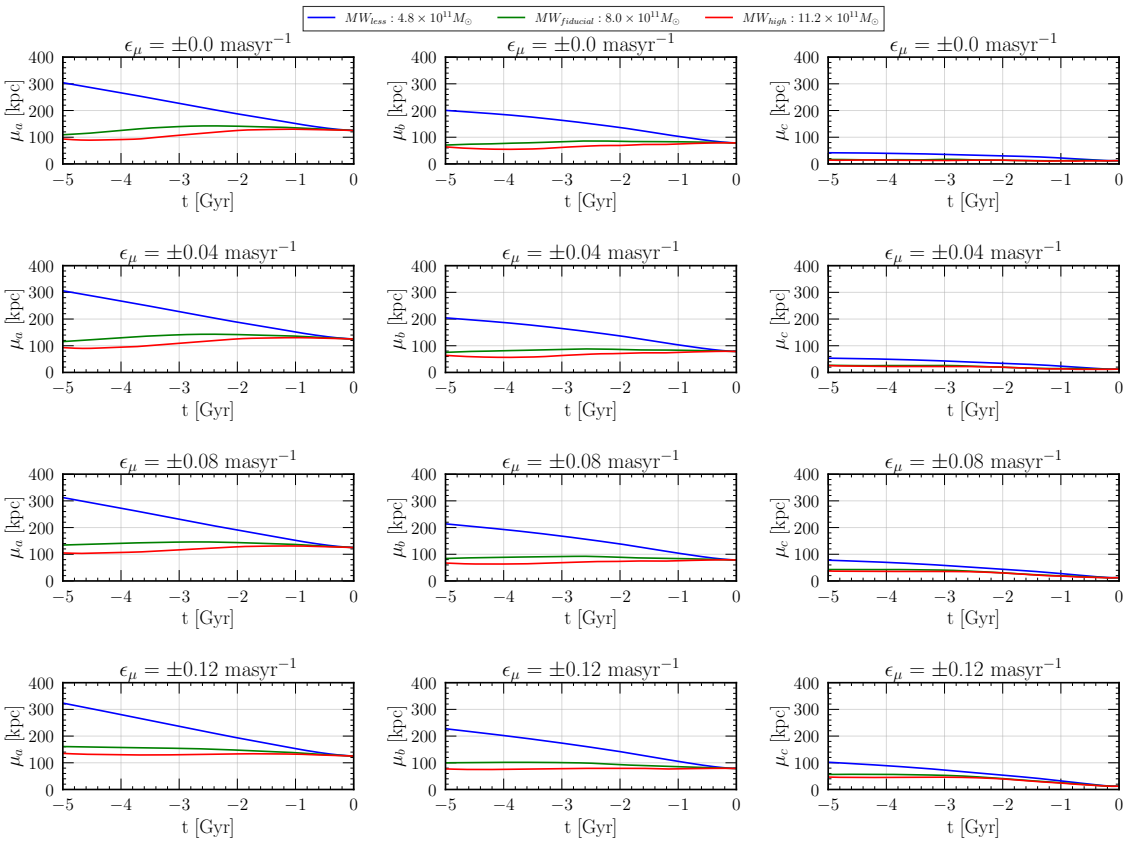

Figure 4.9: Similar comparative analysis of galactic orbital axes under as shown in 4.8. This figure illustrates the mean values of 600 major, minor, and intermediate axes calculated through backward integration under distance uncertainties. It is organized into 12 panels, each representing a different combination of proper motion uncertainty (ranging from 0.00 to 0.12 masyr^{-1}) and Milky Way model. The rows indicate the varying levels of proper motion uncertainty, while each column corresponds to one of the three axes: major (first column), intermediate (second column), and minor (third column). The influence of different Milky Way models is denoted by distinct colors as per the legend, allowing for a clear comparison of their impacts on the galactic orbital axes over time.

In these models, the variations in axis lengths are a direct consequence of changes in gravitational pull due to mass differences. In the $MW_{\rm high}$ model, with increased mass, all axes become more compact as the structure becomes more gravitationally bounded. Conversely, in the $MW_{\rm less}$ model, a reduction in mass leads to an elongation of the axes. This suggests that in the $MW_{\rm less}$ model, more test satellites are drifting away from their host galaxies, causing the system to become unbound. It is important to note that the $MW_{\rm fiducial}$ model was used as a baseline for the $MW_{\rm high}$ and $MW_{\rm less}$ models, with the halo mass being adjusted by 40% (increased

and decreased, respectively). However, the response of the axis extents to these adjustments is striking, with the Milky Way potential with 40% less halo mass having a more pronounced effect on the system than the one with a 40% higher halo mass. This also explains why the axial ratio $\mu_{c/a}$ showed a distinct behavior in the $MW_{\rm less}$ potential as observed in section 4.3.

Figure 4.9 presents a similar analysis, but it also incorporates distance uncertainties. Each of the 12 panels in this figure accounts for distance uncertainties, revealing a trend similar to the previous analysis. However, with the inclusion of distance errors, each axis in every Milky Way model extends slightly, indicating a noticeable, though not extreme, effect on the orbital axes.

4.6 Understanding Escaping Satellites

The preceding sections have highlighted a unique behavior of the galactic plane in the $MW_{\rm less}$ Milky Way model due to its lower halo mass compared to other models. This section will explore the average number of test satellites that become unbound (go beyond after certain radial distance) across all Milky Way potentials, with a particular emphasis on $MW_{\rm less}$. Figure 4.10 illustrates the average number of test satellites that surpass a distance of 300 kpc from the galactic center. It has four panels, each having a different impact of proper motion uncertainties on it. Within each panel, there are three lines, each representing the impact of a different Milky Way potential. These results were derived under conditions with no uncertainties in the distance. In every panel, each model begins with around 2-3 test satellites surpassing the 300 kpc threshold. This happens at the end of forward integration when $N_{\rm sat}$ were integrated forward $N_{\rm realization}$= 20 times, leading to the same starting number in the backward integration. This count varies over time, influenced by the different Milky Way potentials and varying levels of proper motion uncertainties. In the upper left panel of Figure 4.10 when there is no proper motion uncertainties, for $MW_{\rm less}$, the line initially show a relatively stable number of satellites that leave the Milky Way. Over time, there is a gradual increase in the number of test satellites that go beyond 300 kpc, followed by a period of stability. This pattern suggests that the test satellites are more likely to be ejected from the low Milky Way potential influence. Unlike the lower mass Milky Way model, the $MW_{\rm fiducial}$ Milky Way potential model exhibits an opposite behavior; under this model, the number of test satellites going beyond 300 kpc decreases over time, and at 5 Gyr, all $N_{\rm sat}$ test satellites remain under the 300 kpc limit. This trend is even more pronounced in the $MW_{\rm high}$ potential model, where the number of unbound test satellites progressively diminishes over time due to the higher halo mass. Furthermore, the other three panels demonstrate the effect of proper motion uncertainties on satellite dynamics, showing that as uncertainties increase, more test satellites remains at distances greater than 300 kpc across all models. Proper motion affects it by increasing the velocities and the energies of satellites and thus ejecting more test satellites across all the Milky Way potentials.

Additionally, Figure 4.11 displays similar results, but with the inclusion of un-

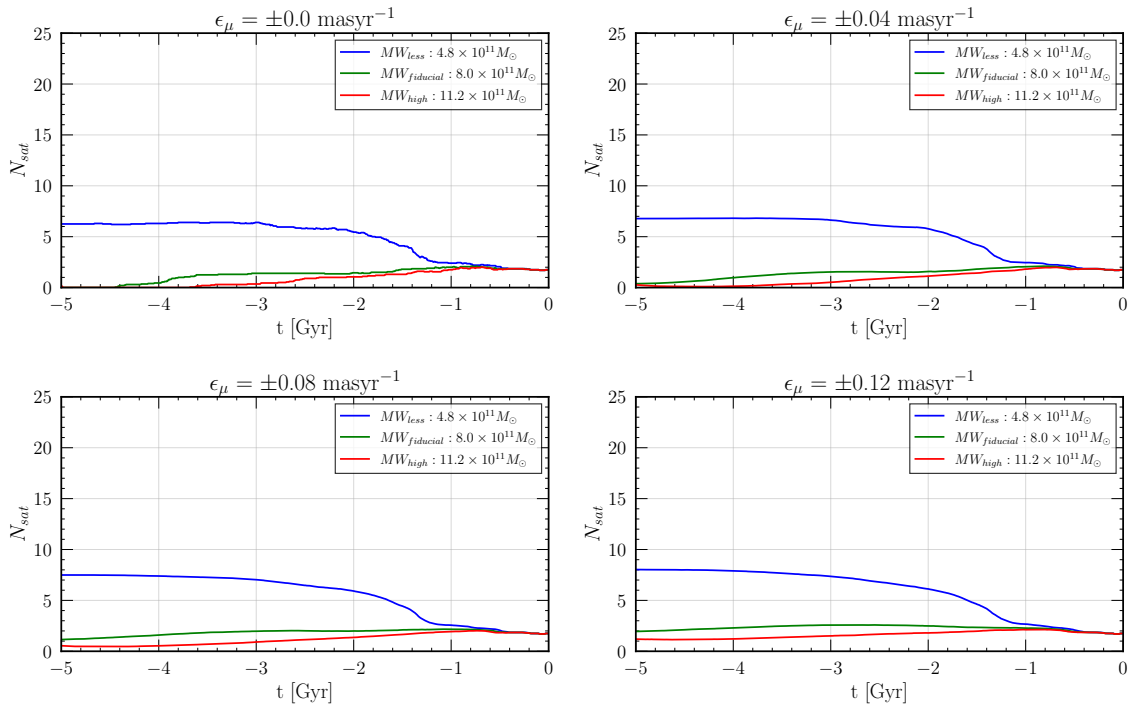

Figure 4.10: This figure presents the average number of test satellites surpassing a 300 kpc distance from the galactic center in various Milky Way potential models, highlighting the impact of proper motion uncertainties inaccuracies on satellite dynamics.

certainties in distance measurements in the analysis. A clear effect of distance uncertainties is evident, further increasing the number of test satellites that exceed the 300 kpc range, see Table 4.1, column $N_{\rm sat} > 300$ kpc for Models BI-05 to BI-08 represent when no distance errors are induced in $MW_{\rm low}$, and models BI-17 to BI-20 are those which has distance errors, from these it is clear that with the inclusion of distance errors at 3 Gyr the system losses more satellites. For $\theta_{tan} = 40°$and 60 °see Appendix A.6.

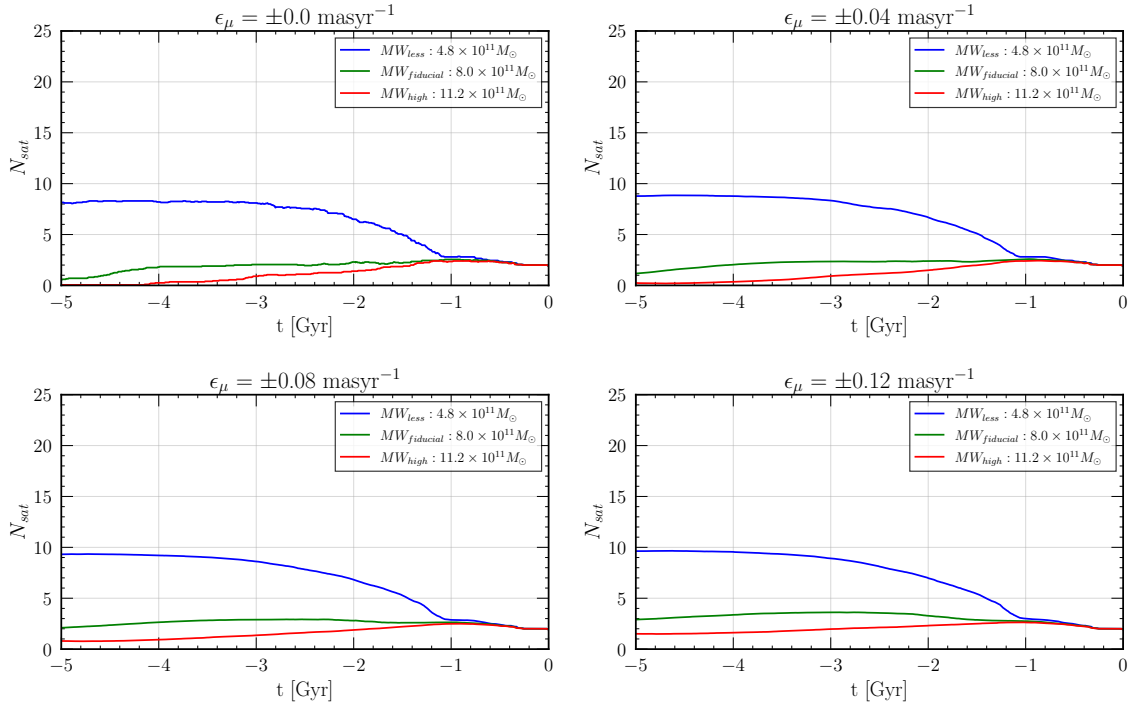

Figure 4.11: This figure presents the average number of test satellites surpassing a 300 kpc distance from the galactic center in various Milky Way potential models, highlighting the impact of proper motion uncertainties and distance measurement inaccuracies on satellite dynamics.

Chapter 5

Summary and Conclusion

The presence of a spatially thin and kinematically coherent plane of satellite around the Milky Way and other massive galaxies have been a subject of debate in astrophysical circles for a long time (Lynden-Bell, 1976; Samuel et al., 2021). This debate stems from the complexities involved in accurately determining the orbital paths of the satellite galaxies. To calculate the orbits with precision, a comprehensive understanding of several key parameters is essential. These include an accurate measurement of satellite's position, distance, line-of-sight velocity, proper motions, the underlying gravitational pontential of the host galaxy and the Galactocentric distance of the Sun and its motion relative to the Galactic center. Many of these crucial parameters, however, remain insufficiently constrained, adding a significant degree of uncertainty to any analysis (Bland-Hawthorn and Gerhard, 2016; Joshi, 2007; Schönrich et al., 2010). Particularly important is the consideration of measurement errors or uncertainties. These uncertainties, especially in proper motions, can significantly affect our analyses (Pawlowski, 2021). These uncertainties can be broadly categorized into statistical and systematic uncertainties. Statistical uncertainties, often due to random measurement variations, can be reduced through statistical methods and larger datasets. Systematic uncertainties, on the other hand, which are not related to random measurement but rather to inherent biases in the measurement process or instruments, pose a major challenges. Maji et al. (2017) and Sawala et al. (2023) have indicated that the satellite plane of the Milky Way galaxy is unstable and may merely be a coincidental alignment. Despite their significant contributions, a notable limitation in their research is the lack of consideration for measurement uncertainties, particularly those related to proper motion. These uncertainties are critical, as they have the potential to significantly alter the outcomes of studies focusing on the evolution of the Milky Way's satellite plane. The proper motion, which remains inadequately defined, is a key factor that could impact the analysis. This highlights the importance of integrating uncertainties into astrophysical research to ensure a more accurate and reliable conclusion.

Addressing these challenges, this study investigated the inferred stability of the plane of satellite galaxies, considering the influences of uncertainties in proper motion, distance, and the impact of various Milky Way potential models. To achieve this, we employed a sophisticated computer-simulated environment, where satellite

galaxies orbit the central host galaxy. Satellite galaxies were treated as test particles, allowing for a detailed analysis of their orbital paths and behavior. This approach provided a unique advantage, offering the flexibility to manipulate and control initial conditions and parameters. By adjusting these variables, we could not only mirror the observed system with high fidelity but also explore hypothetical scenarios. The simulation results shown and analysed in Chapter 4 were primarily focused on an eccentric model setup (with $\theta_{tan} = 80°$), reflecting the observed eccentricities of the Milky Way satellites. The impact on less eccentric orbits was also tested and shown in Appendix A. This study broadly tested two cases, one without the presence of uncertainties in any of these parameters, and other where some increment of uncertainties are introduced to these parameter.

Proper motion is one of the important parameters for investigating the orbital behavior of satellite galaxies, as it defines their movement across the sky in right-ascension and declination. Despite its importance, measuring proper motion accurately is challenging and prone to errors. The Gaia mission, with its DR2 and later EDR3 releases, has made notable strides in measuring the proper motion of at least 11 classical Milky Way satellites (Gaia et al., 2018). However, measuring proper motion precisely for fainter satellites remains challenging, and these uncertainties impact the orbits and inferred stability of the satellite plane. Our analysis in Sec 4.1 revealed that even small proper motion uncertainties significantly impact the satellite plane. As uncertainties increased, a divergence in $\mu_{c/a}$ forward and backward integration was observed, suggesting a loss of apparent stability and predictability in satellite orbits. For uncertainties a the level of Gaia sytsematic uncertainties, a noticeable impact was observed. However, with further increases, the predictability and stability of the satellite system significantly diminished, underscoring the chaotic nature induced by these uncertainties. With 0.12 masyr^{-1} uncertainties, the plane became highly unstable.

We also examined the influence of distance uncertainties in Sec 4.2. By introducing distance uncertainties, even at a level of 5%, while maintaining zero proper motion error, we observed an effect on the satellite orbital evolution. The changes, though less pronounced than those due to proper motion uncertainties, were significant and indicative of the influence of distance errors.

Another crucial parameter that can significantly affect our understanding of the plane of satellite galaxies is the Milky Way potential. We used three Milky Way potential models: $MW_{\rm fiducial}$ with 8×10^{11} solar masses, MW_{less} with a 40% underestimated halo mass, and $MW_{\rm high}$ with a 40% overestimated mass compared to $MW_{\rm fiducial}$. Results in Sec 4.3 showed that the backward integration for $MW_{\rm fiducial}$ demonstrated an expected consistency with its forward counterpart, implying stable evolution of the plane when the Milky Way retains the same potential. However, in $MW_{\rm high}$, the increased mass of the dark matter halo exerted a stronger gravitational pull on the test satellites, accelerating their dynamical evolution and affecting the satellite plane's stability over time. In the results, this has been observed that, although the system did not drastically altered, the $\mu_{c/a}$ do not align precisely and deviates from the forward integration path, suggesting that its stability is not as

pronounced as in MW_{fiducial}. In contrast, MW_{low} showed a different behavior. It initially increases and subsequently flattens, suggesting a dynamic scenario where the satellite plane becomes more dispersed over time. The analysis of the individual mean axes under various Milky Way models showed distinct behaviors, it was revealed that in the MW_{low} potential, the individual axes start to expand over time, indicating a weaker gravitational pull on satellites and resulting in a higher likelihood of satellites exceeding 300 kpc radial distance, making plane of satellites unstable. When integrating these Milky Way potential models with proper motion uncertainties, the results became more complex. Higher uncertainties tended to diminish the dynamical affect of satellite planes across different Milky Way models, suggesting a dominant effect of higher proper motion uncertainties.

These contrasting scenarios show that the mass of the Milky Way is not just a backdrop for the motion of satellites but is a dynamic and integral factor that shapes their evolution. The precise mass of the Milky Way, and thus the potential, therefore holds a crucial importance in modeling and predicting the behavior of satellite planes. A correct understanding of this mass is important not only for precisely simulating the orbits of these test satellites but also for constraining the formation history and evolution of the Milky Way itself. It informs us about the galaxy's interaction with its environment, the distribution and nature of dark matter, and the processes governing galaxy formation on a cosmological scale.

The analysis was also conducted for $\theta_{tan} = 40°$ and $60°$, as detailed in Appendix A. These levels of eccentricity displayed a comparable trend in $\mu_{c/a}$ under uncertainties. Notably, these lower ranges of eccentricities have a reduced impact on the plane.

5.1 Limitation and Future Work

In this study, while providing valuable insights into the impact of various parameters and Milky Way potentials on the plane of satellite galaxies, its crucial to recognize certain limitations. A significant caveat is the absence of consideration for the gravitational effects of massive satellite galaxies like the Large Magellanic Cloud (LMC) and the Small Magellanic Cloud (SMC). These celestial bodies, owing to their substantial mass could affect the mass estimates of Milky Way galaxy (Erkal et al., 2020), and exert significant gravitational forces that can profoundly influence the Milky Way and it's surroundings (Vasiliev, 2023), and thus can influence the stability of the satellite plane. The omission of these influences in the current study represents a notable limitation in our analysis. Additionally, this study assumes a spherical dark matter halo; however, it's important to acknowledge that the halo could be triaxial (Law et al., 2009), which might have implications for our findings. Future studies could enhance our understanding by incorporating the gravitational influence of massive satellite galaxies like the LMC and SMC, as well as considering different shapes of the dark matter halo. Such an approach would allow for a more comprehensive analysis of the satellite plane's dynamics, taking into account the complexities of real-world scenarios. Additionally, using different mass models also

could offer deeper insights into influences of satellite galaxies on the plane's stability and evolution. This would not only refine our models but also contribute to a more nuanced understanding of the gravitational interplay within the Milky Way and its satellite system. By addressing these aspects, future research can build upon the current study's findings, offering a more detailed and accurate depiction of the dynamics governing satellite galaxies.

5.2 Conclusion

In conclusion, this thesis provides significant insights into the dynamics of satellite planes within their host galaxy, offering a deeper understanding of evolution, particularly under the lens of measurement uncertainties. This research has brought to the forefront the critical impact of even minor uncertainties in orbital parameters on our understanding of satellite planes. We checked the impact of measurement uncertainties on the inferred stability of plane of satellites, we found:

- When satellite galaxies' proper motions are measured with high accuracy (or $\epsilon_\mu = 0.00$ mas yr^{-1}), we observe that the system remains highly stable .
- At the level of Gaia uncertainties (with $\epsilon_\mu = 0.04$ mas yr^{-1}), the plane begins to diverge; however, it generally remains well constrained. As the proper motion uncertainties increase (when ϵ_μ is 0.04 and 0.12 mas yr^{-1}), the system becomes highly unstable. The $\mu_{c/a}$ shows a linear increase with the addition of more uncertainties.
- Under distance uncertainties, a noticeable effect is observed. However, this does not dominate the evolution of the satellite plane. Additionally, the impact of distance uncertainties becomes less significant with higher levels of proper motion uncertainties.
- The influence of different Milky Way potential models is significant, especially with $MW_{\rm low}$, which has a smaller halo mass compared to the other three models considered. Due to its lower mass, it struggles to maintain cohesion among the test satellites, leading to increased radial distances and an extension of its major, minor, and intermediate axes. However, under larger proper motion uncertainties, the influence of varying Milky Way potential models diminishes, as the system exhibits unstable behaviors across all potential models.

Thus, this study emphasizes the necessity of precise determination of proper motion, distances of satellite galaxies and the Milky Way's gravitational potential. We have seen how variations in these quantities can significantly shift our understanding of the evolution of satellite planes. Accurate measurement of is thus vital for a comprehensive study of its satellite system and for broader insights into galactic evolution and interactions. However, it is crucial to acknowledge certain limitations in this research. While providing substantial insights, the study does not encompass all possible variables and scenarios. In essence, while this thesis advances our

knowledge in the field, it also opens avenues for future research to address these limitations.

Bibliography

Abuter, R., Amorim, A., Anugu, N., Bauböck, M., Benisty, M., Berger, J.-P., Blind, N., Bonnet, H., Brandner, W., Buron, A., et al. (2018). Detection of the gravitational redshift in the orbit of the star s2 near the galactic centre massive black hole. *Astronomy & Astrophysics*, 615:L15.

Ade, P. A., Aghanim, N., Alves, M., Armitage-Caplan, C., Arnaud, M., Ashdown, M., Atrio-Barandela, F., Aumont, J., Aussel, H., Baccigalupi, C., et al. (2014). Planck 2013 results. i. overview of products and scientific results. *Astronomy & Astrophysics*, 571:A1.

Ade, P. A., Aghanim, N., Arnaud, M., Ashdown, M., Aumont, J., Baccigalupi, C., Banday, A., Barreiro, R., Bartlett, J., Bartolo, N., et al. (2016). Planck 2015 results-xiii. cosmological parameters. *Astronomy & Astrophysics*, 594:A13.

Bland-Hawthorn, J. and Gerhard, O. (2016). The galaxy in context: structural, kinematic, and integrated properties. *Annual Review of Astronomy and Astrophysics*, 54:529–596.

Bovy, J. (2015). galpy: A python library for galactic dynamics. *The Astrophysical Journal Supplement Series*, 216(2):29.

Boylan-Kolchin, M., Springel, V., White, S. D., Jenkins, A., and Lemson, G. (2009). Resolving cosmic structure formation with the millennium-ii simulation. *Monthly Notices of the Royal Astronomical Society*, 398(3):1150–1164.

Bullock, J. S. and Boylan-Kolchin, M. (2017). Small-scale challenges to the λ cdm paradigm. *Annual Review of Astronomy and Astrophysics*, 55:343–387.

Clowe, D., Bradač, M., Gonzalez, A. H., Markevitch, M., Randall, S. W., Jones, C., and Zaritsky, D. (2006). A direct empirical proof of the existence of dark matter. *The Astrophysical Journal*, 648(2):L109.

Colless, M., Dalton, G., Maddox, S., Sutherland, W., Norberg, P., Cole, S., Bland-Hawthorn, J., Bridges, T., Cannon, R., Collins, C., et al. (2001). The 2df galaxy redshift survey: spectra and redshifts. *Monthly Notices of the Royal Astronomical Society*, 328(4):1039–1063.

Conn, A. R., Lewis, G. F., Ibata, R. A., Parker, Q. A., Zucker, D. B., McConnachie, A. W., Martin, N. F., Valls-Gabaud, D., Tanvir, N., Irwin, M. J., et al. (2013).

The three-dimensional structure of the m31 satellite system; strong evidence for an inhomogeneous distribution of satellites. *The Astrophysical Journal*, 766(2):120.

Crnojević, D., Sand, D., Caldwell, N., Guhathakurta, P., McLeod, B., Seth, A., Simon, J., Strader, J., and Toloba, E. (2014). Discovery of a close pair of faint dwarf galaxies in the halo of centaurus a. *The Astrophysical Journal Letters*, 795(2):L35.

Crnojević, D., Sand, D., Spekkens, K., Caldwell, N., Guhathakurta, P., McLeod, B., Seth, A., Simon, J., Strader, J., and Toloba, E. (2016). The extended halo of centaurus a: uncovering satellites, streams, and substructures. *The Astrophysical Journal*, 823(1):19.

Dehnen, W. (1993). A family of potential–density pairs for spherical galaxies and bulges. *Monthly Notices of the Royal Astronomical Society*, 265(1):250–256.

Dehnen, W. and Binney, J. J. (1998). Local stellar kinematics from hipparcos data. *Monthly Notices of the Royal Astronomical Society*, 298(2):387–394.

D'Onghia, E. and Lake, G. (2008). Small dwarf galaxies within larger dwarfs: why some are luminous while most go dark. *The Astrophysical Journal*, 686(2):L61.

Eilers, A.-C., Hogg, D. W., Rix, H.-W., and Ness, M. K. (2019). The circular velocity curve of the milky way from 5 to 25 kpc. *The Astrophysical Journal*, 871(1):120.

Einasto, J. (1965). On the construction of a composite model for the galaxy and on the determination of the system of galactic parameters. *Trudy Astrofizicheskogo Instituta Alma-Ata, Vol. 5, p. 87-100, 1965*, 5:87–100.

Einstein, A. (1915). Die feldgleichungen der gravitation. *Sitzungsberichte der Königlich Preußischen Akademie der Wissenschaften (Berlin*, pages 844–847.

Eisenhauer, F., Genzel, R., Alexander, T., Abuter, R., Paumard, T., Ott, T., Gilbert, A., Gillessen, S., Horrobin, M., Trippe, S., et al. (2005). Sinfoni in the galactic center: young stars and infrared flares in the central light-month. *The Astrophysical Journal*, 628(1):246.

Eisenhauer, F., Schödel, R., Genzel, R., Ott, T., Tecza, M., Abuter, R., Eckart, A., and Alexander, T. (2003). A geometric determination of the distance to the galactic center. *The Astrophysical Journal*, 597(2):L121.

Erkal, D., Belokurov, V. A., and Parkin, D. L. (2020). Equilibrium models of the milky way mass are biased high by the lmc. *Monthly Notices of the Royal Astronomical Society*, 498(4):5574–5580.

Friedman, A. (1922). Über die krümmung des raumes. *Zeitschrift für Physik*, 10(1):377–386.

Fritz, T., Battaglia, G., Pawlowski, M., Kallivayalil, N., Van Der Marel, R., Sohn, S., Brook, C., and Besla, G. (2018). Gaia dr2 proper motions of dwarf galaxies within 420 kpc-orbits, milky way mass, tidal influences, planar alignments, and group infall. *Astronomy & Astrophysics*, 619:A103.

Gaia, C., Brown, A., Vallenari, A., Prusti, T., De Bruijne, J., Babusiaux, C., Juhász, Á., Marschalkó, G., Marton, G., Molnár, L., et al. (2018). Gaia data release 2 summary of the contents and survey properties. *Astronomy & Astrophysics*, 616(1).

Garrison-Kimmel, S., Hopkins, P. F., Wetzel, A., Bullock, J. S., Boylan-Kolchin, M., Kereš, D., Faucher-Giguère, C.-A., El-Badry, K., Lamberts, A., Quataert, E., et al. (2019). The local group on fire: Dwarf galaxy populations across a suite of hydrodynamic simulations. *Monthly Notices of the Royal Astronomical Society*, 487(1):1380–1399.

Geller, M. J. and Huchra, J. P. (1989). Mapping the universe. *Science*, 246(4932):897–903.

Gillessen, S., Plewa, P., Eisenhauer, F., Sari, R., Waisberg, I., Habibi, M., Pfuhl, O., George, E., Dexter, J., von Fellenberg, S., et al. (2017). An update on monitoring stellar orbits in the galactic center. *The Astrophysical Journal*, 837(1):30.

Gum, C. S., Kerr, F. J., and Westerhout, G. (1960). A 21-cm determination of the principal plane of the galaxy (paper ii). *Monthly Notices of the Royal Astronomical Society*, 121(2):132–149.

Hammer, F., Yang, Y., Fouquet, S., Pawlowski, M. S., Kroupa, P., Puech, M., Flores, H., and Wang, J. (2013). The vast thin plane of m31 corotating dwarfs: an additional fossil signature of the m31 merger and of its considerable impact in the whole local group. *Monthly Notices of the Royal Astronomical Society*, 431(4):3543–3549.

Harris, G. L., Rejkuba, M., and Harris, W. E. (2010). The distance to ngc 5128 (centaurus a). *Publications of the Astronomical Society of Australia*, 27(4):457–462.

Helmi, A., Van Leeuwen, F., McMillan, P., Massari, D., Antoja, T., Robin, A., Lindegren, L., Bastian, U., Arenou, F., Babusiaux, C., et al. (2018). Gaia data release 2-kinematics of globular clusters and dwarf galaxies around the milky way. *Astronomy & astrophysics*, 616:A12.

Hernquist, L. (1990). An analytical model for spherical galaxies and bulges. *Astrophysical Journal, Part 1 (ISSN 0004-637X), vol. 356, June 20, 1990, p. 359-364.*, 356:359–364.

Hopkins, P. F., Kereš, D., Oñorbe, J., Faucher-Giguère, C.-A., Quataert, E., Murray, N., and Bullock, J. S. (2014). Galaxies on fire (feedback in realistic environments):

stellar feedback explains cosmologically inefficient star formation. *Monthly Notices of the Royal Astronomical Society*, 445(1):581–603.

Hubble, E. and Humason, M. L. (1931). The velocity-distance relation among extra-galactic nebulae. *Astrophysical Journal, vol. 74, p. 43*, 74:43.

Ibata, R. A., Lewis, G. F., Conn, A. R., Irwin, M. J., McConnachie, A. W., Chapman, S. C., Collins, M. L., Fardal, M., Ferguson, A. M., Ibata, N. G., et al. (2013). A vast, thin plane of corotating dwarf galaxies orbiting the andromeda galaxy. *Nature*, 493(7430):62–65.

Jaffe, W. (1983). A simple model for the distribution of light in spherical galaxies. *Monthly Notices of the Royal Astronomical Society*, 202(4):995–999.

Janes, K. and Adler, D. (1982). Open clusters and galactic structure. *The Astrophysical Journal Supplement Series*, 49:425–445.

Jiao, Y., Hammer, F., Wang, H., Wang, J., Amram, P., Chemin, L., and Yang, Y. (2023). Detection of the keplerian decline in the milky way rotation curve. *arXiv preprint arXiv:2309.00048*.

Joshi, Y. C. (2005). Interstellar extinction towards open clusters and galactic structure. *Monthly Notices of the Royal Astronomical Society*, 362(4):1259–1266.

Joshi, Y. C. (2007). Displacement of the sun from the galactic plane. *Monthly Notices of the Royal Astronomical Society*, 378(2):768–776.

Kafle, P. R., Sharma, S., Lewis, G. F., and Bland-Hawthorn, J. (2012). Kinematics of the stellar halo and the mass distribution of the milky way using blue horizontal branch stars. *The Astrophysical Journal*, 761(2):98.

Klypin, A., Kravtsov, A. V., Valenzuela, O., and Prada, F. (1999). Where are the missing galactic satellites? *The Astrophysical Journal*, 522(1):82.

Klypin, A., Yepes, G., Gottlöber, S., Prada, F., and Hess, S. (2016). Multidark simulations: the story of dark matter halo concentrations and density profiles. *Monthly Notices of the Royal Astronomical Society*, 457(4):4340–4359.

Klypin, A. A., Trujillo-Gomez, S., and Primack, J. (2011). Dark matter halos in the standard cosmological model: Results from the bolshoi simulation. *The Astrophysical Journal*, 740(2):102.

Kroupa, P. (2012). The dark matter crisis: falsification of the current standard model of cosmology. *Publications of the Astronomical Society of Australia*, 29(4):395–433.

Kroupa, P., Theis, C., and Boily, C. M. (2005). The great disk of milky-way satellites and cosmological sub-structures. *Astronomy & Astrophysics*, 431(2):517–521.

Küpper, A. H., Balbinot, E., Bonaca, A., Johnston, K. V., Hogg, D. W., Kroupa, P., and Santiago, B. X. (2015). Globular cluster streams as galactic high-precision scales—the poster child palomar 5. *The Astrophysical Journal*, 803(2):80.

Kuzmin, G. (1956). Model of the steady galaxy allowing of the triaxial distribution of velocities. *Astronomicheskii Zhurnal*, 33:27.

Labini, F. S., Chrobáková, Ž., Capuzzo-Dolcetta, R., and López-Corredoira, M. (2023). Mass models of the milky way and estimation of its mass from the gaia dr3 data set. *The Astrophysical Journal*, 945(1):3.

Law, D. R., Majewski, S. R., and Johnston, K. V. (2009). Evidence for a triaxial milky way dark matter halo from the sagittarius stellar tidal stream. *The Astrophysical Journal*, 703(1):L67.

Lemaître, G. (1927). Un univers homogène de masse constante et de rayon croissant rendant compte de la vitesse radiale des nébuleuses extra-galactiques. *Annales de la Société Scientifique de Bruxelles*, 47:49–59.

Li, H., Hammer, F., Babusiaux, C., Pawlowski, M. S., Yang, Y., Arenou, F., Du, C., and Wang, J. (2021). Gaia edr3 proper motions of milky way dwarfs. i. 3d motions and orbits. *The Astrophysical Journal*, 916(1):8.

Li, Y.-S. and Helmi, A. (2008). Infall of substructures on to a milky way-like dark halo. *Monthly Notices of the Royal Astronomical Society*, 385(3):1365–1373.

Lovell, M. R., Eke, V. R., Frenk, C. S., and Jenkins, A. (2011). The link between galactic satellite orbits and subhalo accretion. *Monthly Notices of the Royal Astronomical Society*, 413(4):3013–3021.

Lynden-Bell, D. (1976). Dwarf galaxies and globular clusters in high velocity hydrogen streams. *Monthly Notices of the Royal Astronomical Society*, 174(3):695–710.

Lynden-Bell, D. and Lynden-Bell, R. (1995). Ghostly streams from the formation of the galaxy's halo. *Monthly Notices of the Royal Astronomical Society*, 275(2):429–442.

Maíz-Apellániz, J. (2001). The spatial distribution of o-b5 stars in the solar neighborhood as measured by hipparcos. *The Astronomical Journal*, 121(5):2737.

Maji, M., Zhu, Q., Marinacci, F., and Li, Y. (2017). Is there a disk of satellites around the milky way? *The Astrophysical Journal*, 843(1):62.

McConnachie, A. W. (2012). The observed properties of dwarf galaxies in and around the local group. *The Astronomical Journal*, 144(1):4.

McConnachie, A. W., Irwin, M. J., Ibata, R. A., Dubinski, J., Widrow, L. M., Martin, N. F., Côté, P., Dotter, A. L., Navarro, J. F., Ferguson, A. M., et al. (2009). The remnants of galaxy formation from a panoramic survey of the region around m31. *Nature*, 461(7260):66–69.

McGaugh, S. S. (2015). A tale of two paradigms: the mutual incommensurability of λcdm and mond. *Canadian Journal of Physics*, 93(2):250–259.

McMillan, P. J. (2016). The mass distribution and gravitational potential of the milky way. *Monthly Notices of the Royal Astronomical Society*, page stw2759.

Merritt, D. (2017). Cosmology and convention. *Studies in History and Philosophy of Science Part B: Studies in History and Philosophy of Modern Physics*, 57:41–52.

Metz, M., Kroupa, P., and Jerjen, H. (2007). The spatial distribution of the milky way and andromeda satellite galaxies. *Monthly Notices of the Royal Astronomical Society*, 374(3):1125–1145.

Metz, M., Kroupa, P., Theis, C., Hensler, G., and Jerjen, H. (2009). Did the milky way dwarf satellites enter the halo as a group? *The Astrophysical Journal*, 697(1):269.

Miyamoto, M. and Nagai, R. (1975). Three-dimensional models for the distribution of mass in galaxies. *Astronomical Society of Japan, Publications, vol. 27, no. 4, 1975, p. 533-543.*, 27:533–543.

Müller, O., Jerjen, H., and Binggeli, B. (2017). New low surface brightness dwarf galaxies in the centaurus group. *Astronomy & Astrophysics*, 597:A7.

Müller, O., Jerjen, H., Pawlowski, M. S., and Binggeli, B. (2016). Testing the two planes of satellites in the centaurus group. *Astronomy & Astrophysics*, 595:A119.

Müller, O., Pawlowski, M. S., Jerjen, H., and Lelli, F. (2018). A whirling plane of satellite galaxies around centaurus a challenges cold dark matter cosmology. *Science*, 359(6375):534–537.

Navarro, J. F. (1996). The structure of cold dark matter halos. In *Symposium-international astronomical union*, volume 171, pages 255–258. Cambridge University Press.

Navarro, J. F., Frenk, C. S., and White, S. D. (1997). A universal density profile from hierarchical clustering. *The Astrophysical Journal*, 490(2):493.

Nichols, M., Colless, J., Colless, M., and Bland-Hawthorn, J. (2011). Accretion of the magellanic system onto the galaxy. *The Astrophysical Journal*, 742(2):110.

Pawlowski, M., Pflamm-Altenburg, J., and Kroupa, P. (2012). The vpos: a vast polar structure of satellite galaxies, globular clusters and streams around the milky way. *Monthly Notices of the Royal Astronomical Society*, 423(2):1109–1126.

Pawlowski, M. S. (2018). The planes of satellite galaxies problem, suggested solutions, and open questions. *Modern Physics Letters A*, 33(06):1830004.

Pawlowski, M. S. (2021). It's time for some plane speaking. *Nature Astronomy*, 5(12):1185–1187.

Pawlowski, M. S., Dabringhausen, J., Famaey, B., Flores, H., Hammer, F., Hensler, G., Ibata, R. A., Kroupa, P., Lewis, G. F., Libeskind, N. I., et al. (2017). Considerations on how to investigate planes of satellite galaxies. *Astronomische Nachrichten*, 338(7):854–861.

Pawlowski, M. S. and Kroupa, P. (2013). The rotationally stabilized vpos and predicted proper motions of the milky way satellite galaxies. *Monthly Notices of the Royal Astronomical Society*, 435(3):2116–2131.

Pawlowski, M. S. and Kroupa, P. (2020). The milky way's disc of classical satellite galaxies in light of gaia dr2. *Monthly Notices of the Royal Astronomical Society*, 491(2):3042–3059.

Pawlowski, M. S., Kroupa, P., and Jerjen, H. (2013). Dwarf galaxy planes: the discovery of symmetric structures in the local group. *Monthly Notices of the Royal Astronomical Society*, 435(3):1928–1957.

Perlmutter, S., Aldering, G., Goldhaber, G., Knop, R., Nugent, P., Castro, P. G., Deustua, S., Fabbro, S., Goobar, A., Groom, D. E., et al. (1999). Measurements of ω and λ from 42 high-redshift supernovae. *The Astrophysical Journal*, 517(2):565.

Ploeckinger, S., Sharma, K., Schaye, J., Crain, R. A., Schaller, M., and Barber, C. (2018). Tidal dwarf galaxies in cosmological simulations. *Monthly Notices of the Royal Astronomical Society*, 474(1):580–596.

Plummer, H. C. (1911). On the problem of distribution in globular star clusters. *Monthly Notices of the Royal Astronomical Society, Vol. 71, p. 460-470*, 71:460–470.

Posti, L. and Helmi, A. (2019). Mass and shape of the milky way's dark matter halo with globular clusters from gaia and hubble. *Astronomy & Astrophysics*, 621:A56.

Prada, F., Klypin, A. A., Cuesta, A. J., Betancort-Rijo, J. E., and Primack, J. (2012). Halo concentrations in the standard λ cold dark matter cosmology. *Monthly Notices of the Royal Astronomical Society*, 423(4):3018–3030.

Press, W. H. and Schechter, P. (1974). Formation of galaxies and clusters of galaxies by self-similar gravitational condensation. *The Astrophysical Journal*, 187:425–438.

Redd, N. T. (2018). Astronomers track dwarf galaxies to better understand the milky way's make-up and evolution. *Proceedings of the National Academy of Sciences*, 115(51):12836–12838.

Reid, M., Menten, K., Zheng, X., Brunthaler, A., Moscadelli, L., Xu, Y., Zhang, B., Sato, M., Honma, M., Hirota, T., et al. (2009). Trigonometric parallaxes of massive star-forming regions. vi. galactic structure, fundamental parameters, and noncircular motions. *The Astrophysical Journal*, 700(1):137.

Riebe, K., Partl, A. M., Enke, H., Forero-Romero, J., Gottlöber, S., Klypin, A., Lemson, G., Prada, F., Primack, J. R., Steinmetz, M., et al. (2013). The multidark database: release of the bolshoi and multidark cosmological simulations. *Astronomische Nachrichten*, 334(7):691–708.

Riess, A. G., Filippenko, A. V., Challis, P., Clocchiatti, A., Diercks, A., Garnavich, P. M., Gilliland, R. L., Hogan, C. J., Jha, S., Kirshner, R. P., et al. (1998). Observational evidence from supernovae for an accelerating universe and a cosmological constant. *The astronomical journal*, 116(3):1009.

Robertson, H. P. (1929). On the foundations of relativistic cosmology. *Proceedings of the National Academy of Sciences*, 15(11):822–829.

Rubin, V. C. and Ford Jr, W. K. (1970). Rotation of the andromeda nebula from a spectroscopic survey of emission regions. *The Astrophysical Journal*, 159:379.

Samuel, J., Wetzel, A., Chapman, S., Tollerud, E., Hopkins, P. F., Boylan-Kolchin, M., Bailin, J., and Faucher-Giguère, C.-A. (2021). Planes of satellites around milky way/m31-mass galaxies in the fire simulations and comparisons with the local group. *Monthly Notices of the Royal Astronomical Society*, 504(1):1379–1397.

Sarkar, P., Yadav, J., Pandey, B., and Bharadwaj, S. (2009). The scale of homogeneity of the galaxy distribution in sdss dr6. *Monthly Notices of the Royal Astronomical Society: Letters*, 399(1):L128–L131.

Sawala, T., Cautun, M., Frenk, C., Helly, J., Jasche, J., Jenkins, A., Johansson, P. H., Lavaux, G., McAlpine, S., and Schaller, M. (2023). The milky way's plane of satellites is consistent with λ cdm. *Nature Astronomy*, 7(4):481–491.

Schönrich, R., Binney, J., and Dehnen, W. (2010). Local kinematics and the local standard of rest. *Monthly Notices of the Royal Astronomical Society*, 403(4):1829–1833.

Siegert, T. (2019). Vertical position of the sun with γ-rays. *arXiv preprint arXiv:1910.09575*.

Simon, J. D. (2019). The faintest dwarf galaxies. *Annual Review of Astronomy and Astrophysics*, 57:375–415.

Smith, R., Duc, P. A., Bournaud, F., and Sukyoung, K. Y. (2016). A formation scenario for the disk of satellites: Accretion of satellites during mergers. *The Astrophysical Journal*, 818(1):11.

Springel, V., Frenk, C. S., and White, S. D. (2006). The large-scale structure of the universe. *nature*, 440(7088):1137–1144.

Springel, V., White, S. D., Jenkins, A., Frenk, C. S., Yoshida, N., Gao, L., Navarro, J., Thacker, R., Croton, D., Helly, J., et al. (2005). Simulations of the formation, evolution and clustering of galaxies and quasars. *nature*, 435(7042):629–636.

Stothers, R. and Frogel, J. A. (1974). The local complex of o and b stars. i. distribution of stars and interstellar dust. *Astronomical Journal, Vol. 79, p. 456 (1974)*, 79:456.

Toomre, A. (1963). On the distribution of matter within highly flattened galaxies. *Astrophysical Journal, vol. 138, p. 385*, 138:385.

Tully, R. B., Libeskind, N. I., Karachentsev, I. D., Karachentseva, V. E., Rizzi, L., and Shaya, E. J. (2015). Two planes of satellites in the centaurus a group. *The Astrophysical Journal Letters*, 802(2):L25.

Tully, R. B., Rizzi, L., Shaya, E. J., Courtois, H. M., Makarov, D. I., and Jacobs, B. A. (2009). The extragalactic distance database. *The Astronomical Journal*, 138(2):323.

Vasiliev, E. (2023). The effect of the lmc on the milky way system. *Galaxies*, 11(2):59.

Vera-Ciro, C. A., Sales, L. V., Helmi, A., Frenk, C. S., Navarro, J. F., Springel, V., Vogelsberger, M., and White, S. D. (2011). The shape of dark matter haloes in the aquarius simulations: evolution and memory. *Monthly Notices of the Royal Astronomical Society*, 416(2):1377–1391.

Walker, A. G. (1935). On the formal comparison of milne's kinematical system with the systems of general relativity. *Monthly Notices of the Royal Astronomical Society, Vol. 95, p. 263-269*, 95:263–269.

Watkins, L. L., van der Marel, R. P., Sohn, S. T., and Evans, N. W. (2019). Evidence for an intermediate-mass milky way from gaia dr2 halo globular cluster motions. *The Astrophysical Journal*, 873(2):118.

Wegg, C. and Gerhard, O. (2013). Mapping the three-dimensional density of the galactic bulge with vvv red clump stars. *Monthly Notices of the Royal Astronomical Society*, 435(3):1874–1887.

White, M. (2001). The mass of a halo. *Astronomy & Astrophysics*, 367(1):27–32.

White, S. D. and Rees, M. J. (1978). Core condensation in heavy halos: a two-stage theory for galaxy formation and clustering. *Monthly Notices of the Royal Astronomical Society*, 183(3):341–358.

Wilkinson, M. and Evans, N. (1999). The present and future mass of the milky way halo. *Monthly Notices of the Royal Astronomical Society*, 310(3):645–662.

York, D. G., Adelman, J., Anderson Jr, J. E., Anderson, S. F., Annis, J., Bahcall, N. A., Bakken, J., Barkhouser, R., Bastian, S., Berman, E., et al. (2000). The sloan digital sky survey: Technical summary. *The Astronomical Journal*, 120(3):1579.

Zwicky, F. (1937). On the masses of nebulae and of clusters of nebulae. *The Astrophysical Journal*, 86:217.

Appendix A

Analysis of Plane of Satellites

This appendix presents the simulations involving less eccentric orbits. Results and analysis for $\theta_{tan} = 80$ been discussed in detail in Chapter 4. Following a similar pattern, I will preset the result which are obtained from $\theta_{tan} = 40°$and $60°$.

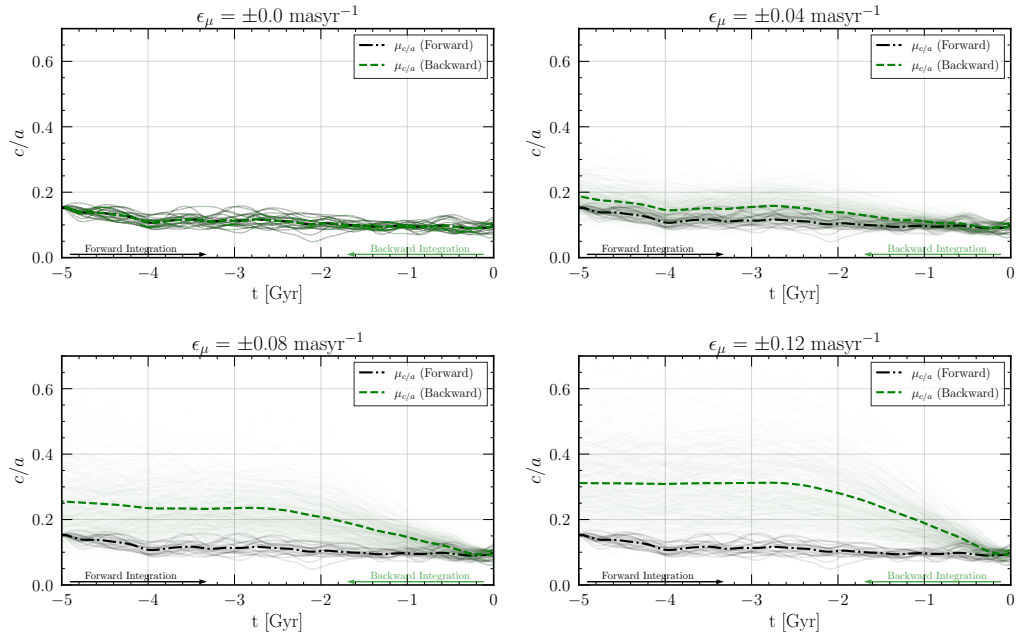

Figure A.1: Four panels illustrating the influence of proper motion uncertainties on the plane of satellite galaxies. This case represents θ_{tan}= 40°. Each panel shows amount of proper motion errors considered.

A.1 Proper Motion Uncertainties

Figures A.1 and A.2 display results analogous to those in Section 4.1. However, they differ in that they showcase outcomes for θ_{tan}= 40°and 60°, instead of 80°. These scenarios exhibit comparable patterns. The Figures are segmented into four panels, each representing different levels of proper motion errors. The c/a ratios for forward integrations are depicted with black lines, whereas those for backward integrations are marked in green. Similar to the previously discussed case, it becomes increasingly difficult to accurately determine the inferred stability of the satellite

plane as the level of proper motion errors escalates. Table A.1 and Table A.2 includes two extra columns: $\Delta_{c/a}$, which represents the difference between $\mu_{c/a}$ from backward integration compared to forward integration after 3 Gyr in backward, and $f_{c/a}$, denoting the fractional change of $\mu_{c/a}$ in backward integrations compared to forward integrations.

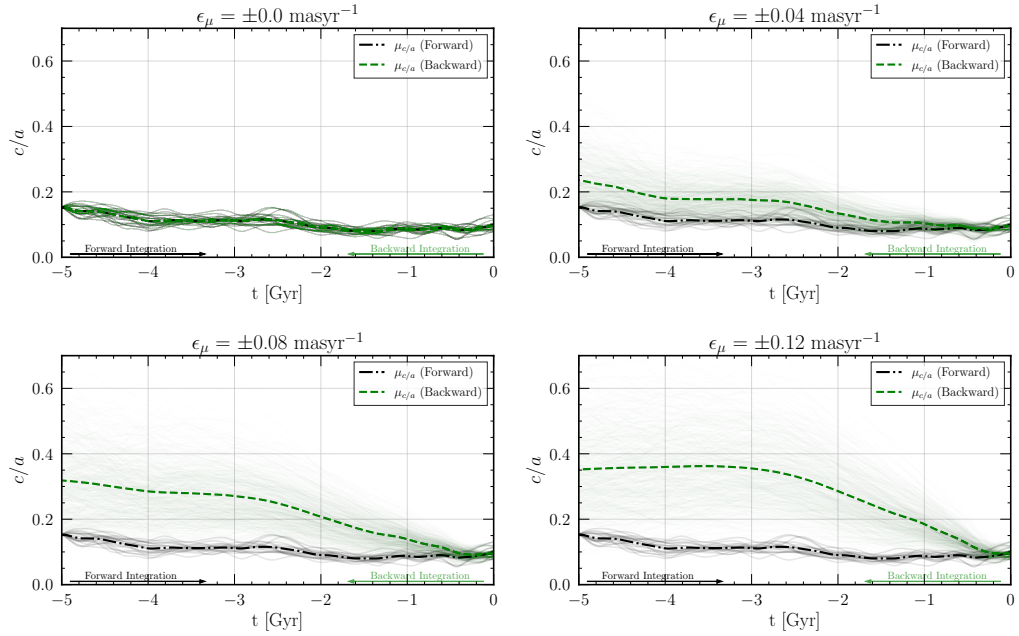

Figure A.2: Four panels illustrating the influence of proper motion uncertainties on the plane of satellite galaxies. This case represents θ_{tan}= 60°. Each panel shows amount of proper motion error considered.

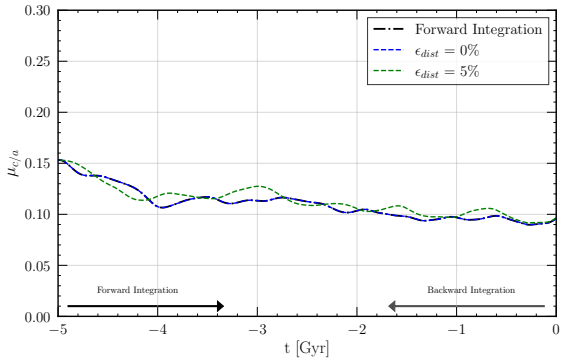

Figure A.3: This figure presents results for θ_{tan}= 40°. The figure illustrates the impact of distance uncertainties on the orbital plane stability of satellite galaxies. Forward integration is represented by a dotted-dashed black line, while backward integration is depicted with a blue and green dashed line.

A.2 Distance Uncertainties

Similarly, Figures A.3 and A.4 display the effects of distance errors on the inferred stability of the plane of satellites for θ_{tan}= 40°and 60°, respectively. The analysis, as discussed in Section 4.2, indicates that the inclusion of distance errors alters $\mu_{c/a}$.

However, this does not significantly impact the overall evolution of $\mu_{c/a}$, See Table A.1 and Table A.2.

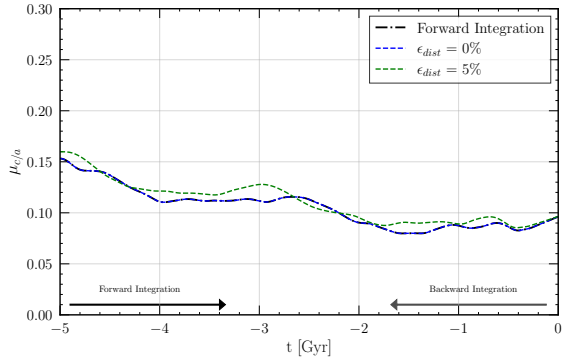

Figure A.4: This figure presents results for θ_{tan}= 60°. The figure illustrates the impact of distance uncertainties on the orbital plane stability of satellite galaxies. Forward integration is represented by a dotted-dashed black line, while backward integration is depicted with a blue and green dashed line.

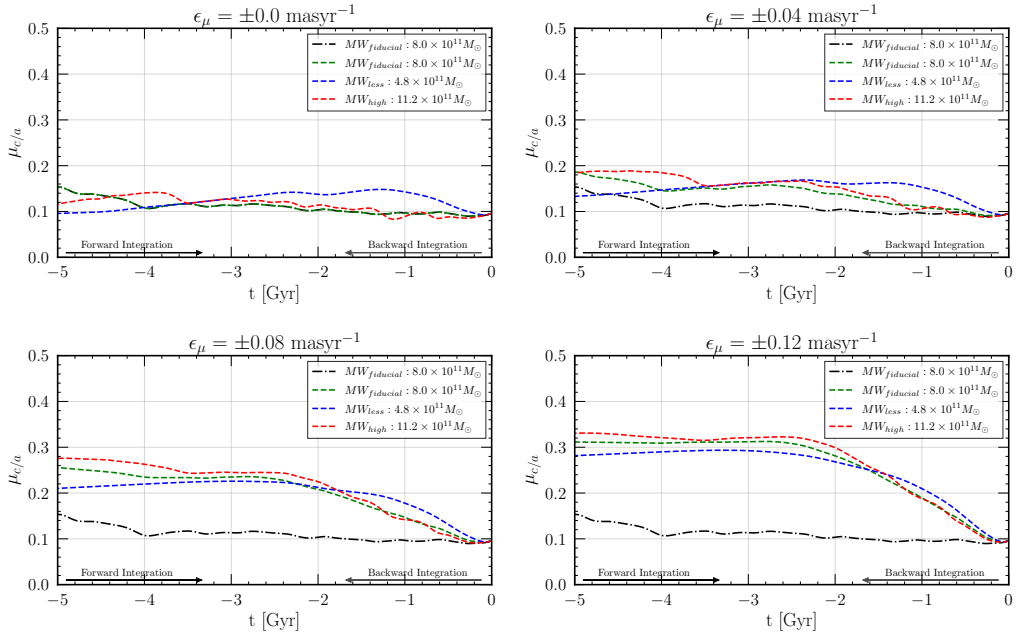

Figure A.5: This figure presents results for θ_{tan}= 40°, and illustrates the $\mu_{c/a}$ for forward integrations, shown as dotted-dash lines, alongside $\mu_{c/a}$ for backward integration under three Milky Way models, characterized by halo mass. The blue, green, and red dashed lines represent the $\mu_{c/a}$ under $MW_{\rm less}$, $MW_{\rm fiducial}$, and $MW_{\rm high}$ potential models, respectively.

A.3 Potential Model

The upper left panel in Figure A.5 and Figure A.6 presents the outputs for θ_{tan}= 40°and θ_{tan}= 60°respectively. These panels shows the affect of using different Milky Way potential on the inferred stability of plane of satellite. These outputs follow the same trend as it was observed in Sec 4.3. See the first column of Figure A.17.

Table A.1: Combined parameters and metrics for backward integration models at 3 Gyr for $\theta_{tan} = 40°$, see Table A.2 and Table 4.1 for $\theta_{tan} = 60°$and $80°$respectively.

Model	ϵ_μ [masyr^{-1}]	ϵ_{dist} [%]	Potential$_{\text{backward}}$	$\Delta_{c/a}$ [masy^{-1}]	$f_{c/a}$	$N_{sat} > 300$ kpc
BI-01	± 0.00	0	MW_{fiducial}	0.000 ± 0.020	1.000 ± 0.180	0.500 ± 0.592
BI-02	± 0.04	0	MW_{fiducial}	0.042 ± 0.038	1.366 ± 0.337	0.625 ± 0.717
BI-03	± 0.08	0	MW_{fiducial}	0.122 ± 0.078	2.074 ± 0.687	1.167 ± 0.937
BI-04	± 0.12	0	MW_{fiducial}	0.199 ± 0.118	2.750 ± 1.042	1.802 ± 1.146
BI-05	± 0.00	0	MW_{less}	0.015 ± 0.032	1.134 ± 0.280	4.350 ± 1.824
BI-06	± 0.04	0	MW_{less}	0.048 ± 0.040	1.426 ± 0.353	4.687 ± 1.647
BI-07	± 0.08	0	MW_{less}	0.112 ± 0.067	1.990 ± 0.592	5.292 ± 1.605
BI-08	± 0.12	0	MW_{less}	0.179 ± 0.095	2.578 ± 0.836	5.803 ± 1.673
BI-09	± 0.00	0	MW_{high}	0.013 ± 0.018	1.113 ± 0.156	0.000 ± 0.000
BI-10	± 0.04	0	MW_{high}	0.049 ± 0.036	1.430 ± 0.313	0.115 ± 0.334
BI-11	± 0.08	0	MW_{high}	0.132 ± 0.082	2.162 ± 0.719	0.425 ± 0.609
BI-12	± 0.12	0	MW_{high}	0.208 ± 0.113	2.829 ± 0.998	1.008 ± 0.878
BI-13	± 0.00	5	MW_{fiducial}	0.014 ± 0.017	1.123 ± 0.148	0.750 ± 0.829
BI-14	± 0.04	5	MW_{fiducial}	0.057 ± 0.042	1.506 ± 0.374	0.965 ± 0.853
BI-15	± 0.08	5	MW_{fiducial}	0.137 ± 0.083	2.207 ± 0.730	1.672 ± 1.051
BI-16	± 0.12	5	MW_{fiducial}	0.205 ± 0.106	2.808 ± 0.934	2.305 ± 1.242
BI-17	± 0.00	5	MW_{less}	0.036 ± 0.041	1.314 ± 0.360	5.800 ± 2.182
BI-18	± 0.04	5	MW_{less}	0.064 ± 0.044	1.566 ± 0.389	6.513 ± 1.895
BI-19	± 0.08	5	MW_{less}	0.119 ± 0.061	2.051 ± 0.539	6.923 ± 1.866
BI-20	± 0.12	5	MW_{less}	0.191 ± 0.087	2.685 ± 0.767	7.483 ± 1.908
BI-21	± 0.00	5	MW_{high}	0.010 ± 0.016	1.091 ± 0.142	0.100 ± 0.300
BI-22	± 0.04	5	MW_{high}	0.053 ± 0.041	1.464 ± 0.362	0.212 ± 0.444
BI-23	± 0.08	5	MW_{high}	0.140 ± 0.090	2.231 ± 0.796	0.768 ± 0.780
BI-24	± 0.12	5	MW_{high}	0.217 ± 0.122	2.910 ± 1.074	1.322 ± 0.937

Table A.2: Combined parameters and metrics for backward integration models at 3 Gyr for $\theta_{tan} = 60°$, see Table 4.1 and Table A.1 for $\theta_{tan} = 80°$and $40°$respectively.

Model	ϵ_μ [masyr^{-1}]	ϵ_{dist} [%]	Potential$_{\text{backward}}$	$\Delta_{c/a}$ [masy^{-1}]	$f_{c/a}$	$N_{sat} > 300$ kpc
BI-01	± 0.00	0	MW_{fiducial}	0.000 ± 0.011	1.000 ± 0.097	1.200 ± 0.812
BI-02	± 0.04	0	MW_{fiducial}	0.064 ± 0.043	1.574 ± 0.387	1.188 ± 0.830
BI-03	± 0.08	0	MW_{fiducial}	0.159 ± 0.082	2.425 ± 0.738	1.662 ± 0.958
BI-04	± 0.12	0	MW_{fiducial}	0.244 ± 0.110	3.181 ± 0.991	2.340 ± 1.091
BI-05	± 0.00	0	MW_{less}	0.007 ± 0.031	1.065 ± 0.275	4.800 ± 1.503
BI-06	± 0.04	0	MW_{less}	0.050 ± 0.037	1.447 ± 0.335	5.185 ± 1.504
BI-07	± 0.08	0	MW_{less}	0.123 ± 0.065	2.105 ± 0.583	5.742 ± 1.538
BI-08	± 0.12	0	MW_{less}	0.202 ± 0.089	2.812 ± 0.799	6.147 ± 1.493
BI-09	± 0.00	0	MW_{high}	0.005 ± 0.015	1.046 ± 0.130	0.450 ± 0.497
BI-10	± 0.04	0	MW_{high}	0.068 ± 0.047	1.607 ± 0.421	0.520 ± 0.580
BI-11	± 0.08	0	MW_{high}	0.176 ± 0.094	2.575 ± 0.845	0.873 ± 0.773
BI-12	± 0.12	0	MW_{high}	0.251 ± 0.106	3.246 ± 0.954	1.390 ± 0.972
BI-13	± 0.00	5	MW_{fiducial}	0.016 ± 0.013	1.144 ± 0.120	1.350 ± 0.963
BI-14	± 0.04	5	MW_{fiducial}	0.073 ± 0.046	1.657 ± 0.415	1.532 ± 0.941
BI-15	± 0.08	5	MW_{fiducial}	0.170 ± 0.084	2.520 ± 0.755	2.275 ± 1.104
BI-16	± 0.12	5	MW_{fiducial}	0.244 ± 0.107	3.188 ± 0.957	2.977 ± 1.200
BI-17	± 0.00	5	MW_{less}	0.029 ± 0.038	1.260 ± 0.342	6.900 ± 1.758
BI-18	± 0.04	5	MW_{less}	0.062 ± 0.040	1.556 ± 0.362	7.378 ± 1.836
BI-19	± 0.08	5	MW_{less}	0.128 ± 0.063	2.147 ± 0.563	7.723 ± 1.864
BI-20	± 0.12	5	MW_{less}	0.206 ± 0.090	2.849 ± 0.805	8.092 ± 1.821
BI-21	± 0.00	5	MW_{high}	0.010 ± 0.014	1.087 ± 0.125	0.700 ± 0.640
BI-22	± 0.04	5	MW_{high}	0.078 ± 0.051	1.697 ± 0.461	0.757 ± 0.686
BI-23	± 0.08	5	MW_{high}	0.186 ± 0.094	2.668 ± 0.842	1.170 ± 0.843
BI-24	± 0.12	5	MW_{high}	0.258 ± 0.119	3.311 ± 1.069	1.823 ± 1.047

A.4 Combination of Parameters

The remaining panels in Figures A.5 and A.6 present the combined effect of proper motion uncertainties and Milky Way potential models on the inferred stability of the plane of satellites. These panels also follow a similar trend as observed in Section 4.4. In these cases, an increase in θ_{tan} is associated with an increased $\mu_{c/a}$ in all scenarios. Similarly, Figures A.7 and A.8 presents combined affect of proper motion errors, distance errors and different Milky Way potential models, see Table A.1 and Table A.2..

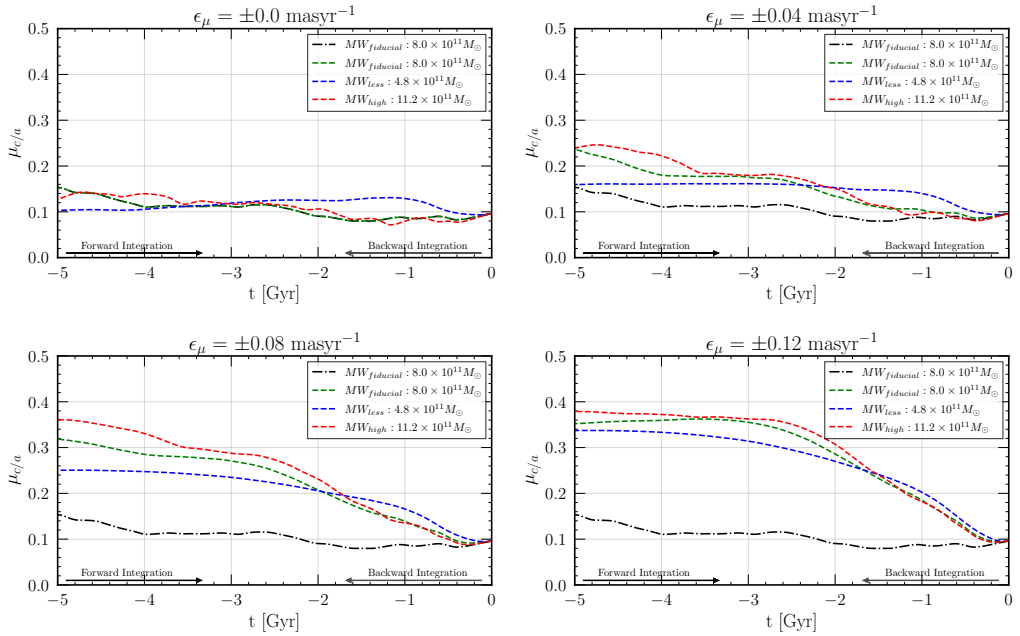

Figure A.6: This figure presents results for θ_{tan}= 60°, and illustrates the $\mu_{c/a}$ for forward integrations, shown as dotted-dash lines, alongside $\mu_{c/a}$ for backward integration under three Milky Way models, characterized by halo mass. The blue, green, and red dashed lines represent the $\mu_{c/a}$ under $MW_{\rm less}$, $MW_{\rm fiducial}$, and $MW_{\rm high}$ potential models, respectively.

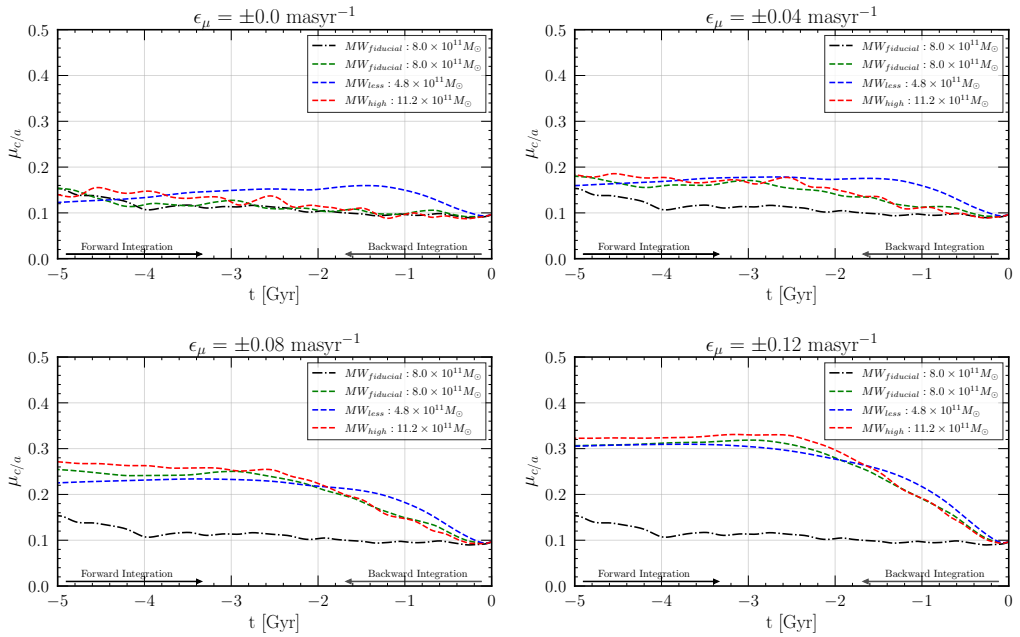

Figure A.7: This figure presents results for θ_{tan}= 40°. This figure contains four panels is similar to A.5 but now has distance errors of 5% in all panels. Each panels highlights the affects of different proper motion uncertainties. Furthermore, each panel sheds light on how varying Milky Way potential models — $MW_{\rm less}$, $MW_{\rm fiducial}$, and $MW_{\rm high}$ — influence the flattening of the plane.

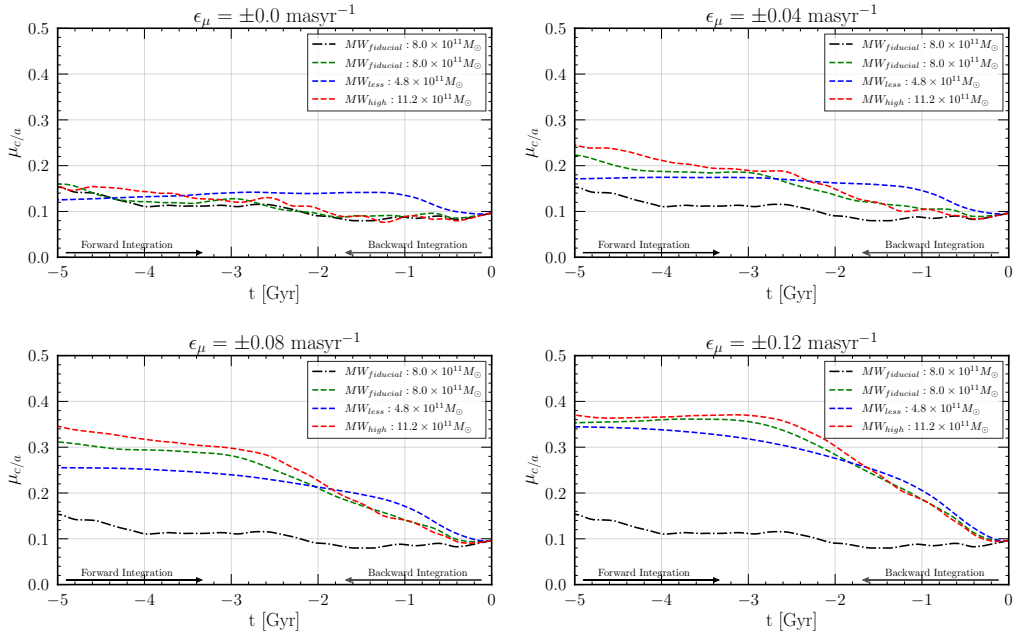

Figure A.8: This figure presents results for θ_{tan}= 60°. This figure contains four panels is similar to A.6 but now has distance errors of 5% in all panels. Each panels highlights the affects of different proper motion uncertainties. Furthermore, each panel sheds light on how varying Milky Way potential models — $MW_{\rm less}$, $MW_{\rm fiducial}$, and $MW_{\rm high}$ — influence the flattening of the plane.

A.5 Individual Axes

Figures A.9 and A.10 illustrate the impact of proper motion uncertainties and various Milky Way potential models on the individual extent of the plane axis under θ_{tan}= 40°and 60°, respectively. In contrast, Figures A.11 and A.12 present similar analyses, but in these cases, a 5% distance error is also factored in. From the Figures it can be seen that with an increase of θ_{tan}, the extent of individual axes increases more with during the backward integrations.

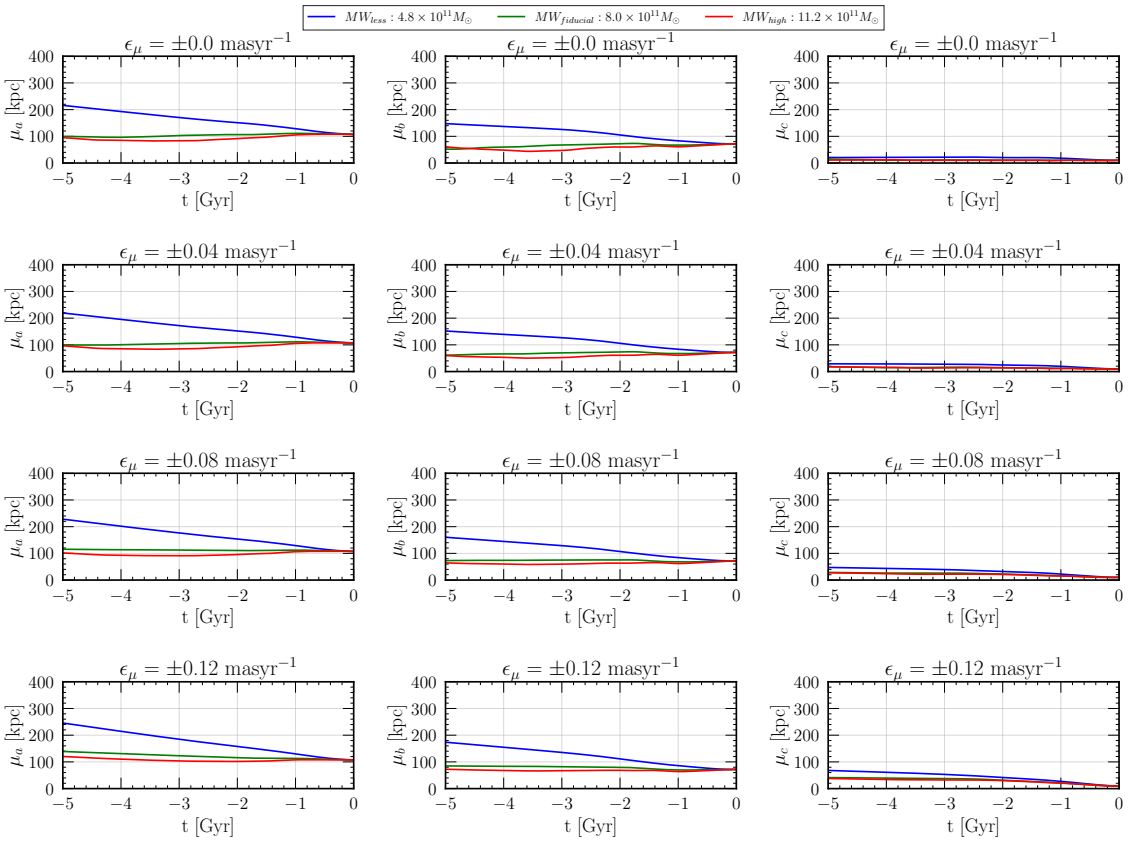

Figure A.9: This figure presents results for θ_{tan}= 40°and shows the comparative analysis of galactic orbital axes under varying proper motion uncertainties and Milky Way Models. This figure illustrates the mean values of 600 major, minor, and intermediate axes calculated through backward integration. The rows indicate the varying levels of proper motion uncertainty, while each column corresponds to one of the three axes: major (first column), intermediate (second column), and minor (third column). The influence of different Milky Way models is denoted by distinct colors as per the legend, allowing for a clear comparison of their impacts on the galactic orbital axes over time.

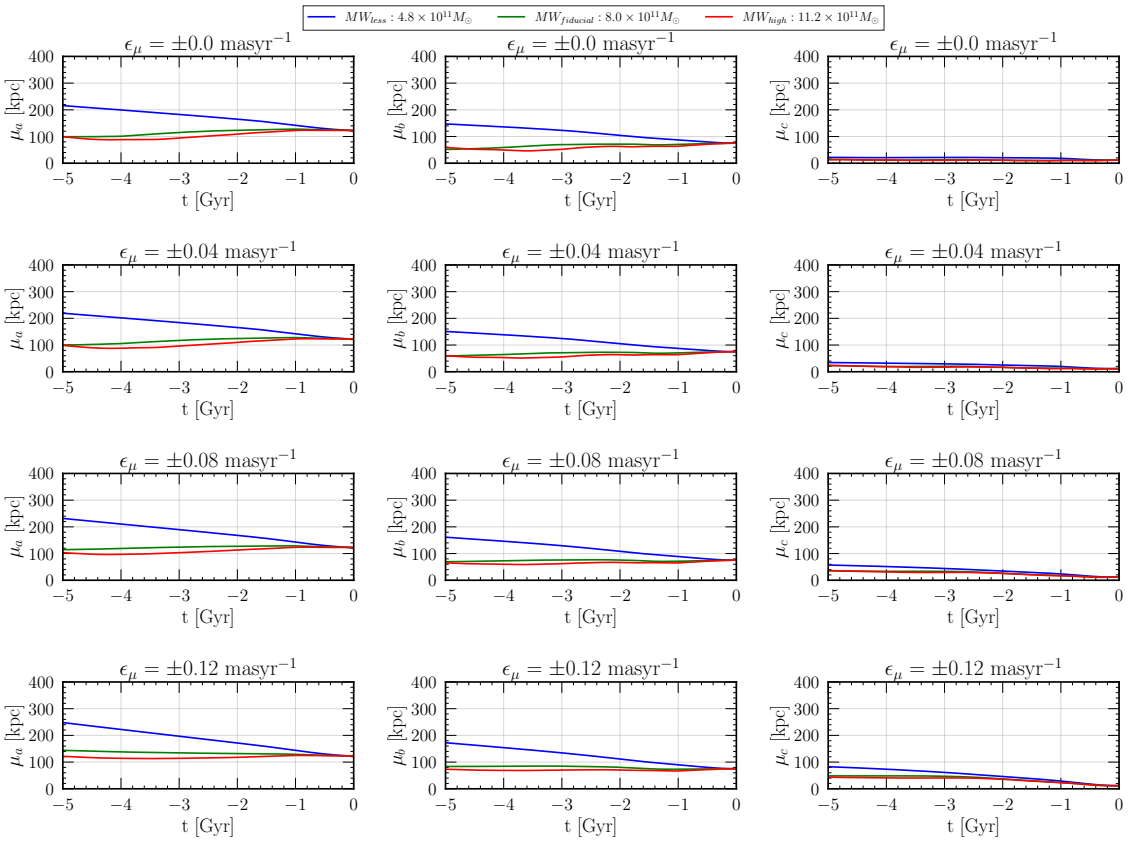

Figure A.10: This figure presents results for θ_{tan}= 60°and shows the comparative analysis of galactic orbital axes under varying proper motion uncertainties and Milky Way Models. This figure illustrates the mean values of 600 major, minor, and intermediate axes calculated through backward integration. The rows indicate the varying levels of proper motion uncertainty, while each column corresponds to one of the three axes: major (first column), intermediate (second column), and minor (third column). The influence of different Milky Way models is denoted by distinct colors as per the legend, allowing for a clear comparison of their impacts on the galactic orbital axes over time

A.6 Escaping Test Satellites

Figures A.13 and A.14 display the number of test satellites that exceeded the 300 kpc radius threshold under θ_{tan} = 40°and 60°, respectively. The effect of proper motion errors is depicted in each of the four panels, with each line within a panel representing the influence of different Milky Way potential models. While, figure A.15 and A.16 show similar output but in these Figures there is an additional parameter, distance errors. From Table A.1, Table A.2 and Table 4.1, it is clear that higher eccentricities cause more satellites to escape 300 kpc range.

Figure A.17 and A.18 shows the $\Delta_{c/a}$ and $f_{c/a}$, respectively, at 3 Gyrs as a function of proper motion uncertainties. The figure is arranged row-wise to demonstrate the varying effects of different Milky Way potentials. Column-wise, the plot elucidates the impacts of distance uncertainties. Each panel contains three distinct lines, representing the eccentricities of the satellite system. All panels clearly show the effect of proper motion uncertainties on the $\Delta_{c/a}$ and $f_{c/a}$ — in other words,

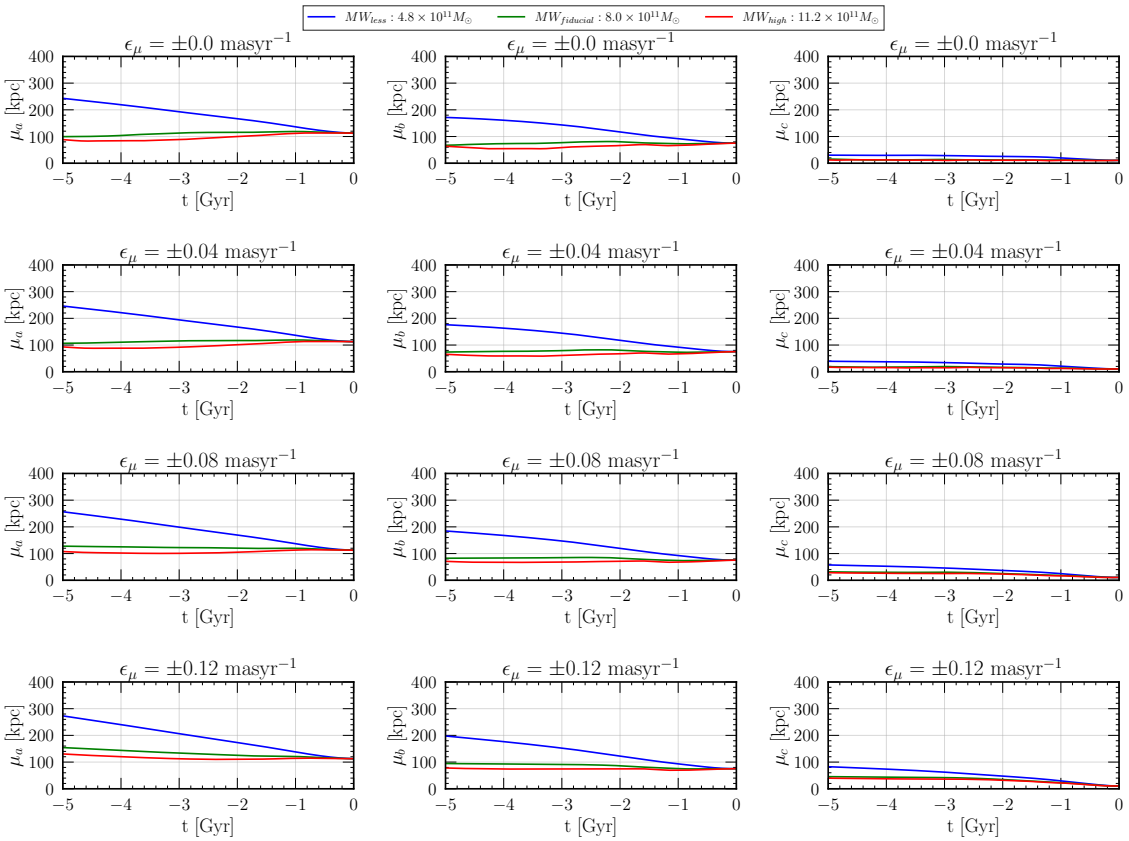

Figure A.11: This figure presents results for θ_{tan}= 40°and shows the comparative analysis of galactic orbital axes under varying proper motion uncertainties, distance uncertainties and Milky Way Models. This figure illustrates the mean values of 600 major, minor, and intermediate axes calculated through backward integration. The rows indicate the varying levels of proper motion uncertainty, while each column corresponds to one of the three axes: major (first column), intermediate (second column), and minor (third column). The influence of different Milky Way models is denoted by distinct colors as per the legend. Each panel accounts 5% distance uncertainties

proper motion uncertainties widen the plane of the satellite. The figure exhibits a linear behavior, indicating that higher proper motion uncertainties lead to increased system instability. Each panel also reveals the influence of the eccentricities of test satellites. In all panels, more eccentric orbits further widen the $\mu_{c/a}$ of the plane. Additionally, the different potential models influence the plane, though at higher proper motions, the effect of potential becomes less significant. Across all plots, the effects of proper motion uncertainties and the eccentricities of orbits remain consistent.

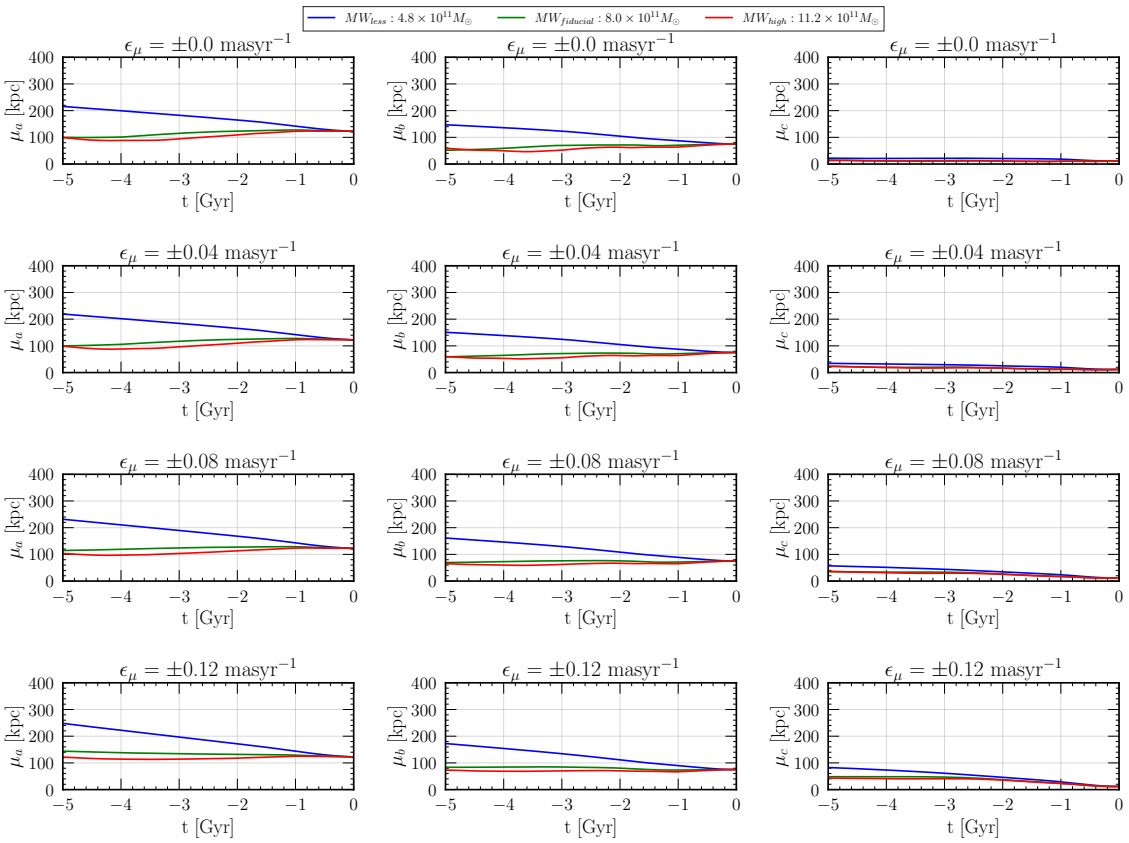

Figure A.12: This figure presents results for θ_{tan}= 60°and shows the comparative analysis of galactic orbital axes under varying proper motion uncertainties, distance uncertainties and Milky Way Models. This figure illustrates the mean values of 600 major, minor, and intermediate axes calculated through backward integration. The rows indicate the varying levels of proper motion uncertainty, while each column corresponds to one of the three axes: major (first column), intermediate (second column), and minor (third column). The influence of different Milky Way models is denoted by distinct colors as per the legend. Each panel accounts 5% distance uncertainties

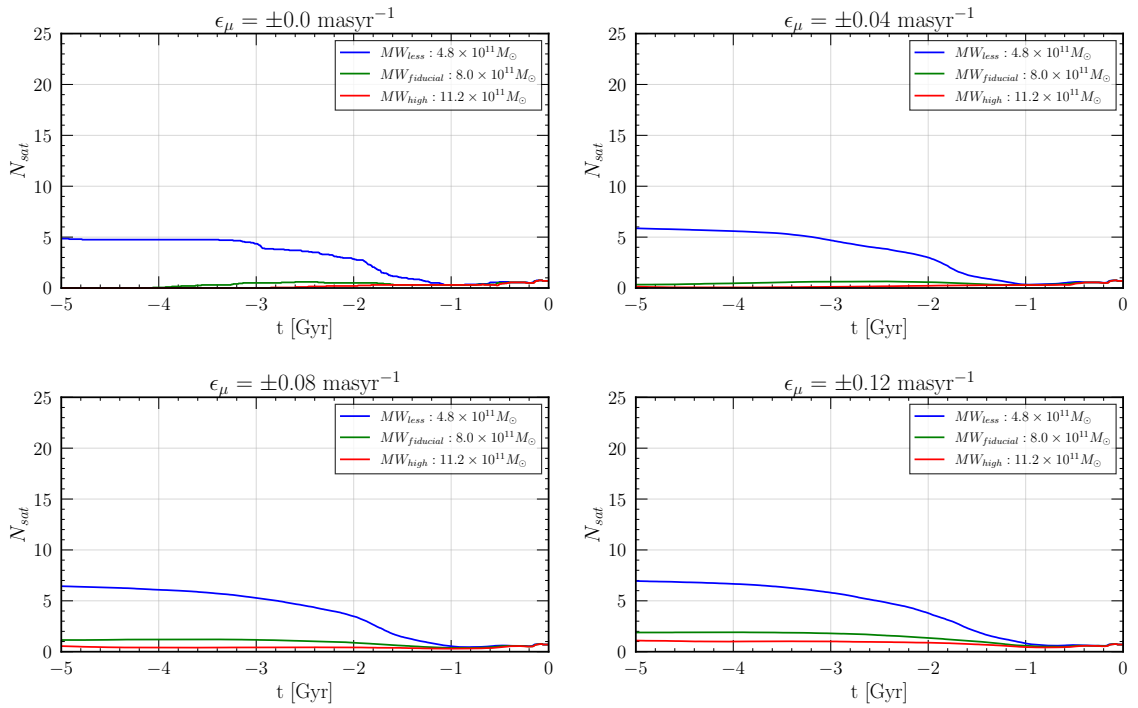

Figure A.13: This figure presents results for θ_{tan}= 40°and shows the average number of test satellites surpassing the 300 kpc distance from the galactic center in various Milky Way potential models, highlighting the impact of proper motion uncertainties on satellite dynamics.

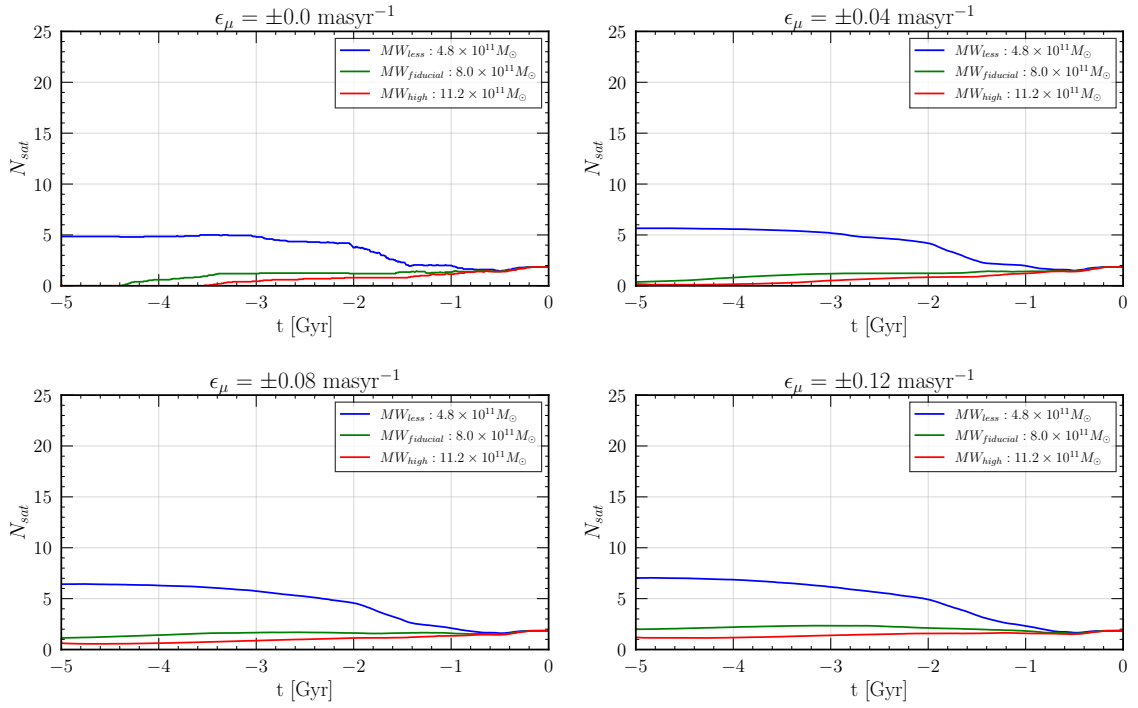

Figure A.14: This figure presents results for θ_{tan}= 60°and shows the average number of test satellites surpassing the 300 kpc distance from the galactic center in various Milky Way potential models, highlighting the impact of proper motion uncertainties on satellite dynamics.

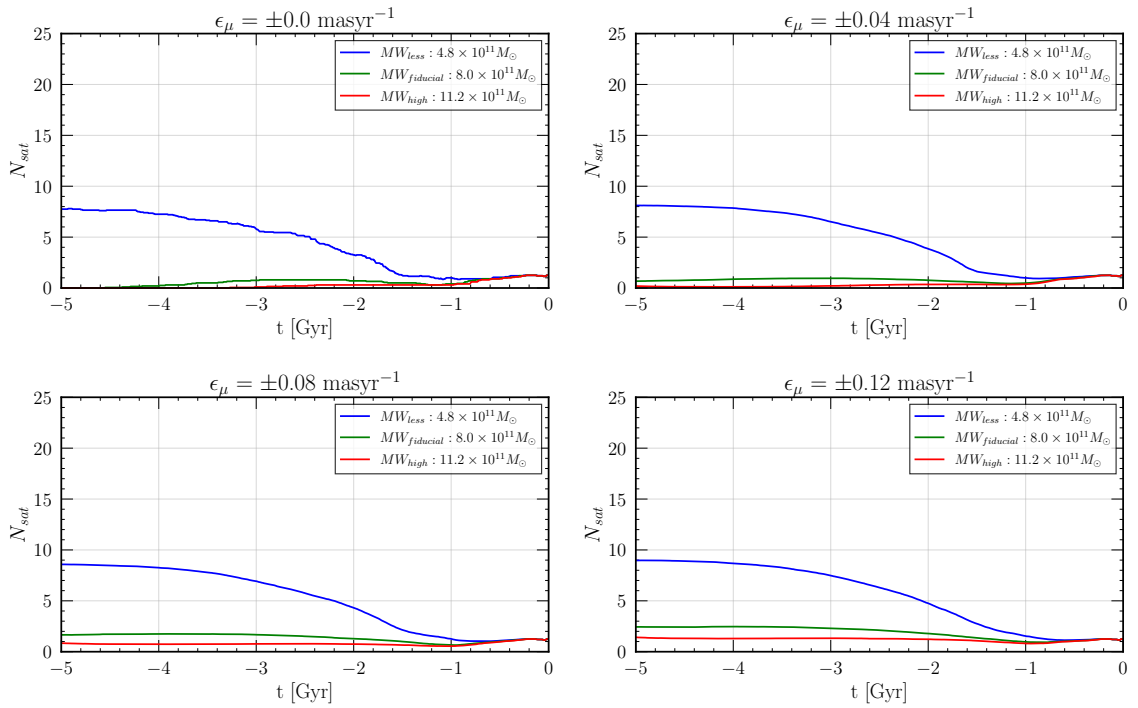

Figure A.15: This figure presents results for θ_{tan}= 40°and shows the average number of test satellites surpassing the 300 kpc distance from the galactic center in various Milky Way potential models, highlighting the impact of proper motion uncertainties and distance measurement inaccuracies on satellite dynamics.

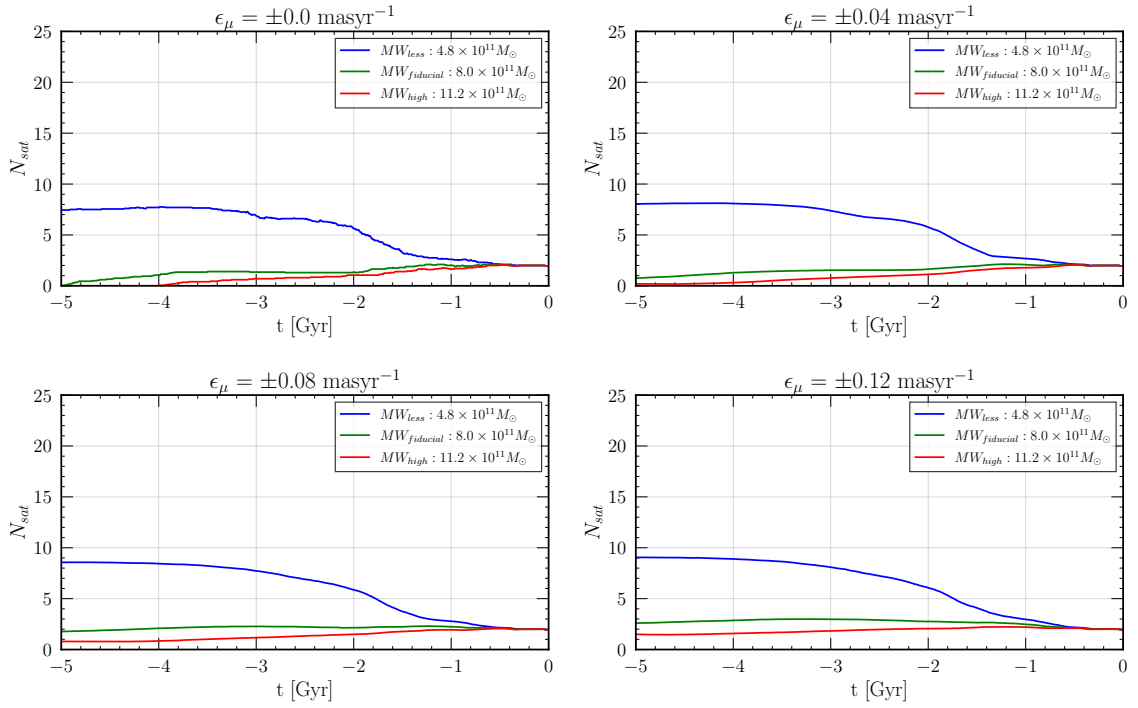

Figure A.16: This figure presents results for θ_{tan}= 60°and shows the average number of test satellites surpassing the 300 kpc distance from the galactic center in various Milky Way potential models, highlighting the impact of proper motion uncertainties and distance measurement inaccuracies on satellite dynamics.

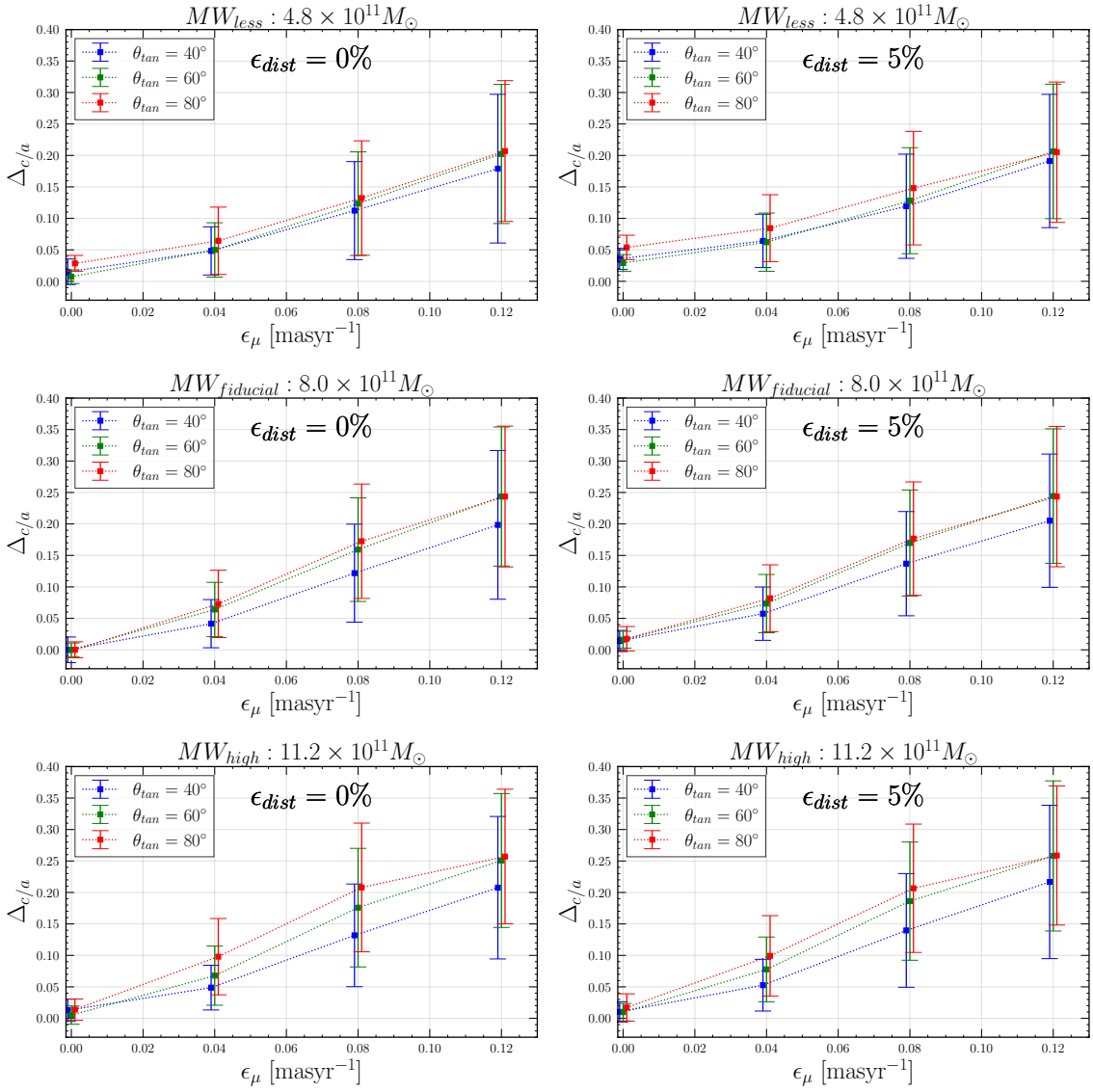

Figure A.17: Figure illustrating $\Delta_{c/a}$ as a function of proper motion uncertainties at 3 Gyr in backward integration. Row-wise, the figure demonstrates the effect of different Milky Way potentials, while column-wise, it shows the impact of distance uncertainties. Within each panel, three lines representing θ_{tan} and the eccentricities of the satellite system are shown.

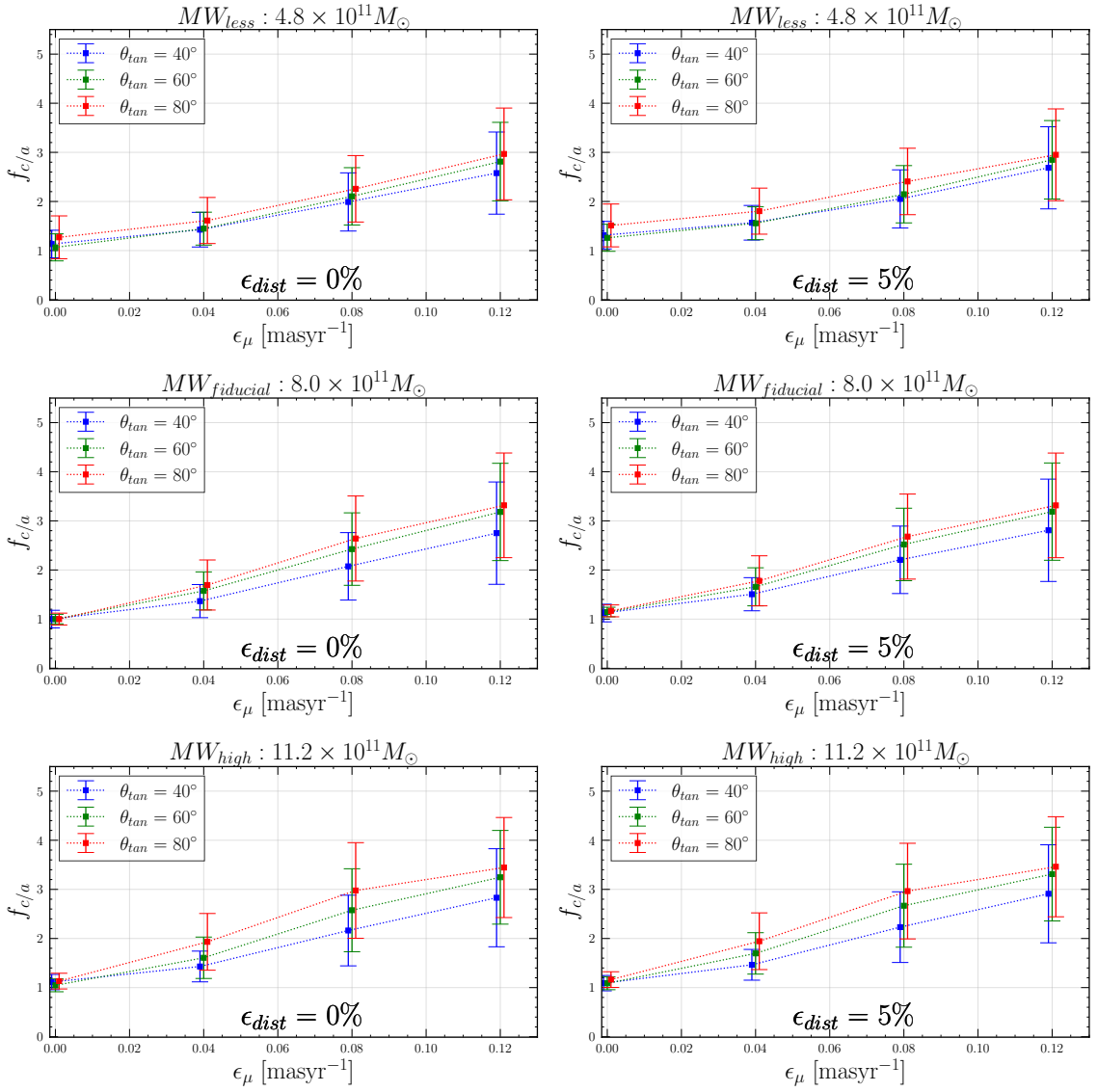

Figure A.18: Figure illustrating fc/a as a function of proper motion uncertainties at 3 Gyr in backward integration. Row-wise, the figure demonstrates the effect of different Milky Way potentials, while column-wise, it shows the impact of distance uncertainties. Within each panel, three lines representing θ_{tan} and the eccentricities of the satellite system are shown.

Table A.3: R-square values for Different Potential Models.

Potential Model	ϵ_{dist} [%]	θ_{tan} [°]	$R^2_{\Delta_{c/a}}$	$R^2_{f_{c/a}}$
MW_{fiducial}	0	40	0.9829	0.9829
MW_{less}	0	40	0.9796	0.9796
MW_{high}	0	40	0.9762	0.9762
MW_{fiducial}	0	60	0.9944	0.9944
MW_{less}	0	60	0.9835	0.9835
MW_{high}	0	60	0.9904	0.9904
MW_{fiducial}	0	80	0.9956	0.9956
MW_{less}	0	80	0.9782	0.9782
MW_{high}	0	80	0.9811	0.9811
MW_{fiducial}	5	40	0.9877	0.9877
MW_{less}	5	40	0.9665	0.9665
MW_{high}	5	40	0.9823	0.9823
MW_{fiducial}	5	60	0.9916	0.9916
MW_{less}	5	60	0.9710	0.9710
MW_{high}	5	60	0.9918	0.9918
MW_{fiducial}	5	80	0.9943	0.9943
MW_{less}	5	80	0.9815	0.9815
MW_{high}	5	80	0.9844	0.9844

List of Figures